UNIVERSITY OF OKLAHOMA

GRADUATE COLLEGE

FAULT MECHANISM AND ROCK STRENGTH DETERMINATION IN THE SELE FORMATION SHALE CAPROCK THROUGH INVERSION OF 3D SEISMIC IN THE FORTIES FIELD, NORTH SEA

A THESIS

SUBMITTED TO THE GRADUATE FACULTY

in partial fulfillment of the requirements for the

Degree of

MASTER OF SCIENCE

By

ALIYA URAZIMANOVA
Norman, Oklahoma
2011

FAULT MECHANISM AND ROCK STRENGTH DETERMINATION IN THE SELE FORMATION SHALE CAPROCK THROUGH INVERSION OF 3D SEISMIC IN THE FORTIES FIELD, NORTH SEA

A THESIS APPROVED FOR THE
CONOCO PHILLIPS SCHOOL OF GEOLOGY AND GEOPHYSICS

BY

____
Dr. Kurt Marfurt, Chair

____
Dr. John D. Pigott

____
Dr. J. Timothy Kwiatkowski

____
Dr. Jean-Claude Roegiers

ACKNOWLEDGEMENTS

I would like to thank my advisor Dr. Kurt Marfurt for all his help, encouragement, support, motivation, and guidance throughout my school years. Special thanks to the thesis committee members Dr. John Pigott, Dr. J. Tim Kwiatkowski, and Dr. Jean-Claude Roegiers for their advices, discussions, and exceptional input to this thesis work. I would also like to thank Apache Corporation, especially Gregg Barker, Farid Mohamed, and Phil Rose, for providing the survey and well data used in this project and sharing their knowledge and expertise. I also would like to thank Schlumberger, Hampson-Russell and TameCat LLC for providing licenses for the software that were used in this work.

For all my friends and colleagues I met in Norman, Oklahoma that put my life at ease away from home. I would like to acknowledge Bagdat Toleubay and Azar Hasanov for their input and valuable discussions of the work. To all faculty and staff, especially Donna Mullins, who was like a godmother to me during my school years in Norman, Oklahoma.

To my family, who always believed in me and my dreams, and provided great support to reach them. Lastly, many thanks for Xavier Refunjol, who was a shoulder and motivator throughout this work.

TABLE OF CONTENTS

LIST OF FIGURES

LIST OF TABLES

LIST OF SYMBOLS

As this study bridges the gap between engineering and geosciences, consequently some of the notation of nomenclature is mixed. For example, in geomechanics, μ is used to define the coefficient of friction of the rock or pre-existing plane of weakness within the rock, while geophysicists use μ to define rigidity of the rock. An alternative yet consistent interpretation of variables used in this thesis is described in the table below.

E	Young's modulus
g	Acceleration due to gravity
k_1	Most-positive curvature
k_2	Most-negative curvature
LOP	Leak-off pressure
LOT	Leak-off test
P_p	Pore pressure
P_p^{hydro}	Hydrostatic pressure associated with a water column at a given depth
r_{Pi}	Zero-offset P-wave reflection coefficient at i^{th} interface
$R(\theta)$	Reflection coefficient as a function of angle
S_{Hmax}	Maximum horizontal principal stress
S_{hmin}	Minimum horizontal principal stress
S_i	Principal stress component
s_{ij}	General stress tensor component
C_o	Cohesive strength of the rock
S_V	Vertical principal stress
UCS	Unconfined compressive strength
V_p	P-wave velocity
V_s	S-wave velocity
Z_p	P-wave Impedance
Z_s	S-wave impedance

z_w	Depth of the water column
β	Angle between fault normal and maximum effective principal stress
γ	Coefficient of internal friction
Δt	Slowness from well logs
θ	Incidence angle
λ	First Lamé parameter (compressability)
μ	Second Lamé parameter (rigidity/shear modulus)
ρ_w	Water density
σ_i	Effective principal stress (S_i - P_p)
σ_n	Effective normal stress
τ	Shear stress along a surface
	Angle of internal friction
Φ	porosity

ABSTRACT

Forties is a mature offshore field in the Central North Sea producing oil from Paleocene turbidite sands. In this work, I concentrate on the Sele formation, shale caprock of the reservoir, by relating geomechanical parameters of the rock to tectonic deformation using 3D seismic.

The objective of this project is to analyze the rock strength of the shale caprock of the Forties field in the North Sea that could relate to shale instability and more importantly to reactivation of the pre-existing faults in the region, which in turn could cause well drilling problems. Using fault slip theory and constructing Mohr's diagrams, I anticipate a decrease in the coefficient of friction of the pre-existing planes of weakness due to known layering and fractures within the shale caprock, resulting in low unconfined compressive strength (UCS) of the rock. Mapping low UCS values in the field was achieved by relating UCS to rigidity, μ, values obtained from the wells, and extending this relationship laterally using 3D seismic.

Edge-detecting seismic attributes together with the curvature attributes were extensively used for interpretation and modeling structural features. I used the structural models to interpret the nature of the geomechanical parameters of the rock, achieved from the elastics impedance inversion of the seismic data.

CHAPTER I

INTRODUCTION

Problem Statement

The mature North Sea Forties field is located in the UK sector of the Central Graben and has been discovered and developed since 1970s, with more than 300 wells and five platforms. Even though drilling parameters have been well established, McIntyre et al. (2010) point out that within a period from 2002 to 2007, 45% out of 94 wells drilled were lost due to drilling and completion problems. Borehole failures were classified as following operational causes: hole cleaning, wellbore instability, mechanical issues, and directional issues (McIntyre et al., 2010). Main failures were associated with friable and unconsolidated reservoir sands that cause major sand production. However, a recent core study of the overlying seal showed the complexity of shale caprock rock fabric. Figure 1.1 shows representative pictures of the shale cores of the Sele formation caprock, illustrating "imperfections" ranging from highly layered to fractured rock; creating rock anisotropy, which changes stiffness and rock strength with wellbore deviation (McIntyre et al. 2010). Reservoir depletion and a decrease in reservoir pore pressure increase the relative stresses in shales, which in turn causes complications in designing a safe mud-weight window. Pre-existing fractures and faults within the shale caprock and their possible drilling- or production-induced slippage or reactivation may also increase borehole instabilities. Minimizing risks of well borehole instability and borehole failure is essential for better economics and well hazard elimination. Success rates can be improved by careful integration of 3D seismic analysis with structural features and geomechanics.

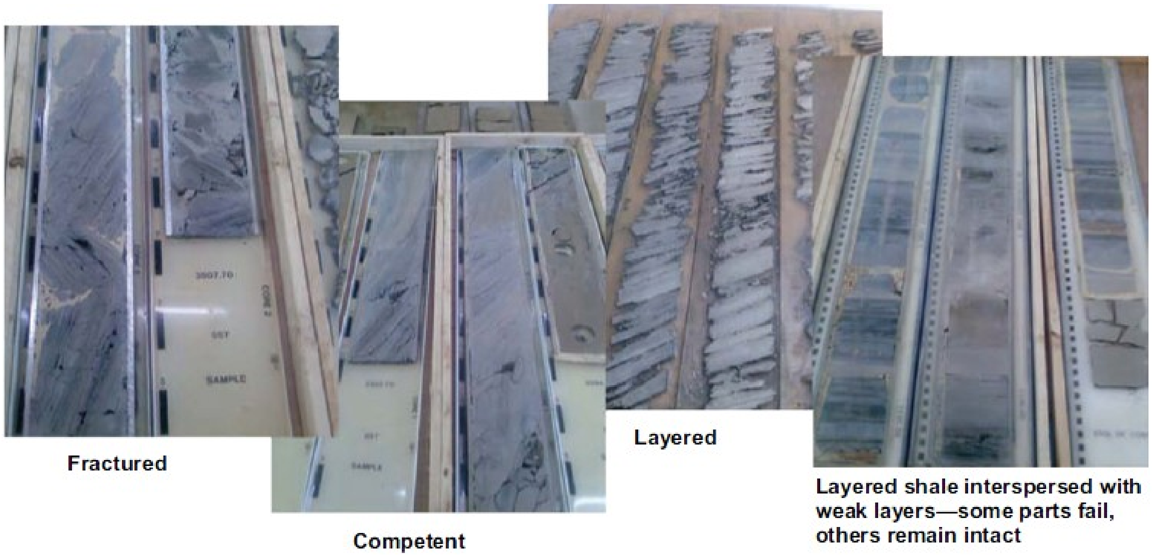

Figure 1.1. Photographs of core sample from Forties field wells sampled at the depth of the Sele formation shale caprock, illustrating variation of the rock fabric from fractured to layered causing rock strength variation (After McIntyre et al., 2010).

Hypothesis

I hypothesize that fault reactivation may be initiated not only by changes in the in-situ stresses due to depletion of the reservoirs, but also due to the low rock strength which gives rise to an anomalously low coefficient of friction. This lack of friction potentially creates sufficient shear stress along the pre-existing fractures. By constructing Mohr circles using in-situ stresses with the fault angles estimated using 3D seismic, geomechanical analysis should indicate possible regions of slip along pre-existing faults. Conditioning of 3D seismic through structure-oriented filters and computed 3D seismic attributes will assist in interpretation of the faults in the Sele formation. 3D seismic elastic impedance inversion theory estimates of Lamé parameters, λ and μ, can be used to detect lateral variation of rock strength, where the lowest values of Lamé parameters correspond to the weak rock strength areas susceptible to fault reactivation.

Methodology

Conditioning of 3D seismic using structure-oriented filters (SOF) smoothes reflectors, increases the signal-to-noise ratio, and enhances discontinuities of the reflector due to faults. SOF allows for more precise surface and fault interpretation, which may be confirmed with the 3D seismic attributes such as edge detecting Sobel filters, coherence, and curvature. After calculating dip angles of the interpreted faults, the wells with no reported drilling and completing problems through the faults cutting the Sele formation were identified and plotted in order to establish a statistical estimate of fault angles not prone to reactivation.

Pre-stack seismic data serve as input to elastic impedance inversion in order to map low Lamé's first parameter, μ, weak rock in the field. These regions of weak shale rock are correlated with wells in the field that reported shale instability within a borehole. Estimating and detecting low μ provides a means of mapping the lateral extent of higher risk fractured and layered (higher risk) rock within the field. Geomechanical analysis will be applied to those faults which cut regions of weak rock, since they are the most prone to reactivation.

History of Forties Field

Discovered in 1970 with the discovery well 20/21-1 and put onstream in 1975, the Forties Field is located in blocks 21/10 and 22/6 of the UK sector of the Central North Sea (Figure 1.2). The oil producing reservoir is Paleocene in age and consists of deep water turbidite sandstones of the Forties Member within the Sele formation with recoverable reserves of about 2590 MMBO (Ahmadi et al., 2003). The reservoir consists of interbedded sub-marine fan system sandstones with average permeabilities of 700 mD and an ultimate oil recovery factor of 61%, with oil gravity up to 37^o API trapped in an anticline formed by differential compaction of channel-like turbidite sands with respect to adjacent overbank muds. The source rock for the reservoir is from Kimmeridge clay formation. Several 3D seismic surveys have been acquired in order to map turbidity channels and monitor and enhance reservoir production.

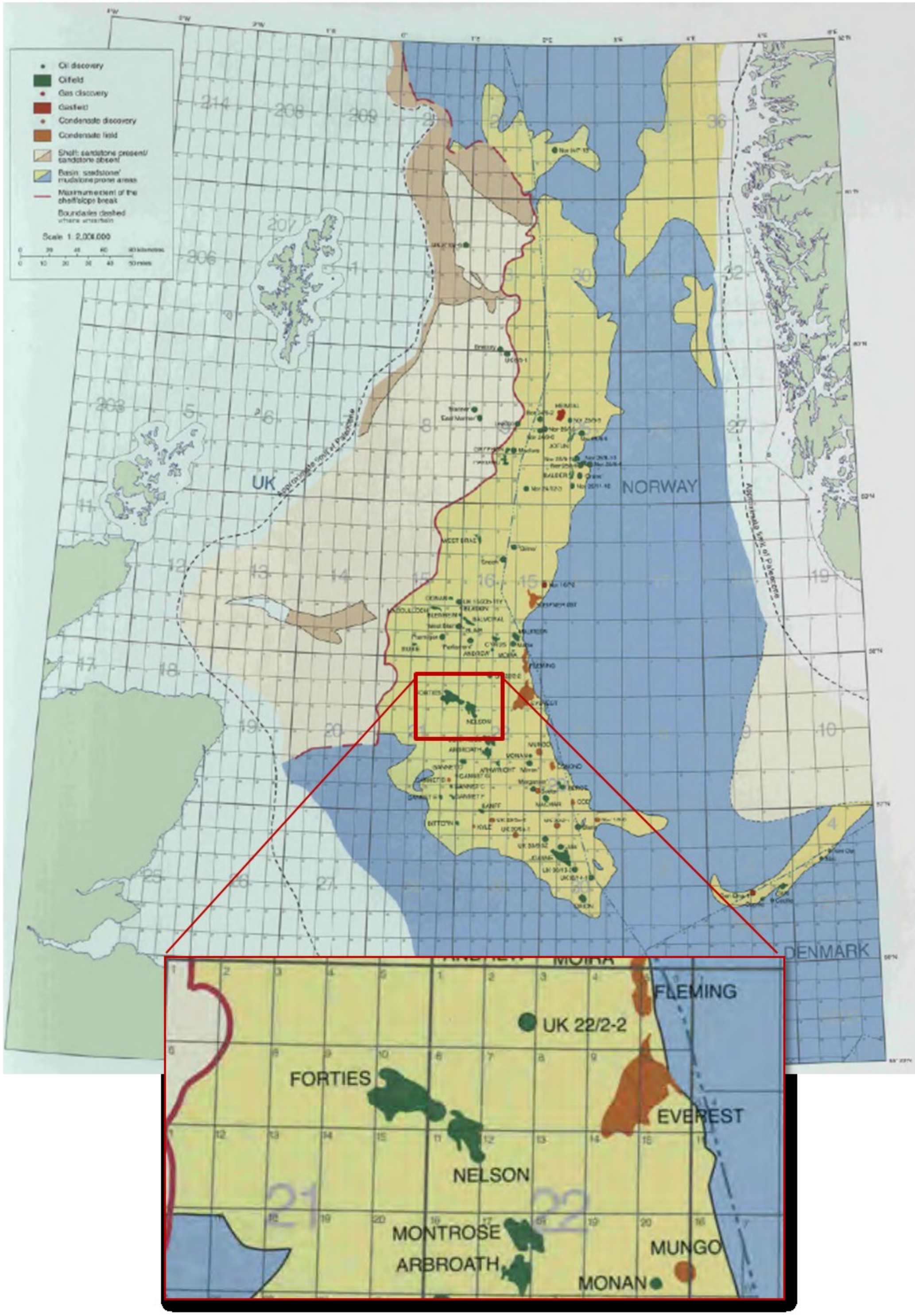

Figure 1. 2. Location of the Forties Field in the UK sector of the Central North Sea

(After Ahmadi et al., 2003).

CHAPTER II

BASIN EVOLUTION

Stratigraphy

Pre-Cretaceous age volcanics are the deepest formation penetrated by the discovery well 21/10-1 that was drilled to 3388 m. Well 21/10-1 was used to construct the stratigraphic column for the field (Figure 2.1a). 753 m of volcanics section of the Jurassic age is mainly composed of "alkaline olivine-basalts with large pyroxene phenocrysts and altered porphyritic rocks with agglomerates, pyroclastics and tuffs interbedded with red-brown siltstones and mudstones" (Walmsley, 1975). Upper Mesozoic, Maastrichtian in age micrites unconformably overlie on the volcanics and are about 114 m thick. The Paleocene section is about 506 m thick and is generally comprised of terrigenous sediments except for the lower intermediate layer between the Paleocene and Maastrichtian formation, Danian section, which is a white micritic limestone (Walmsley, 1975).

The main reservoir in the Forties field is found in the Upper Paleocene-Eocene Forties Sandstone member of the Sele Formation. Previous stratigraphic conventions (Walmsley, 1975; Hill and Wood, 1980; Carman and Young, 1981, Wills and Peattie, 1990) recognized Forties sandstones as a separate formation of the Montrose Group, lying between the Andrew Formation of the same group underneath and conformably overlain by shales of the Sele Formation within the Rogaland Group (Figure 2.1a). Recent biostratigraphic studies integrated with the well logs and seismic data, redefined the Montrose Group sediments, and reassigned the Andrew and Forties sandstone units to the Lista and Sele formations, respectively (Figure 2.1b; McInally et al., 2003).

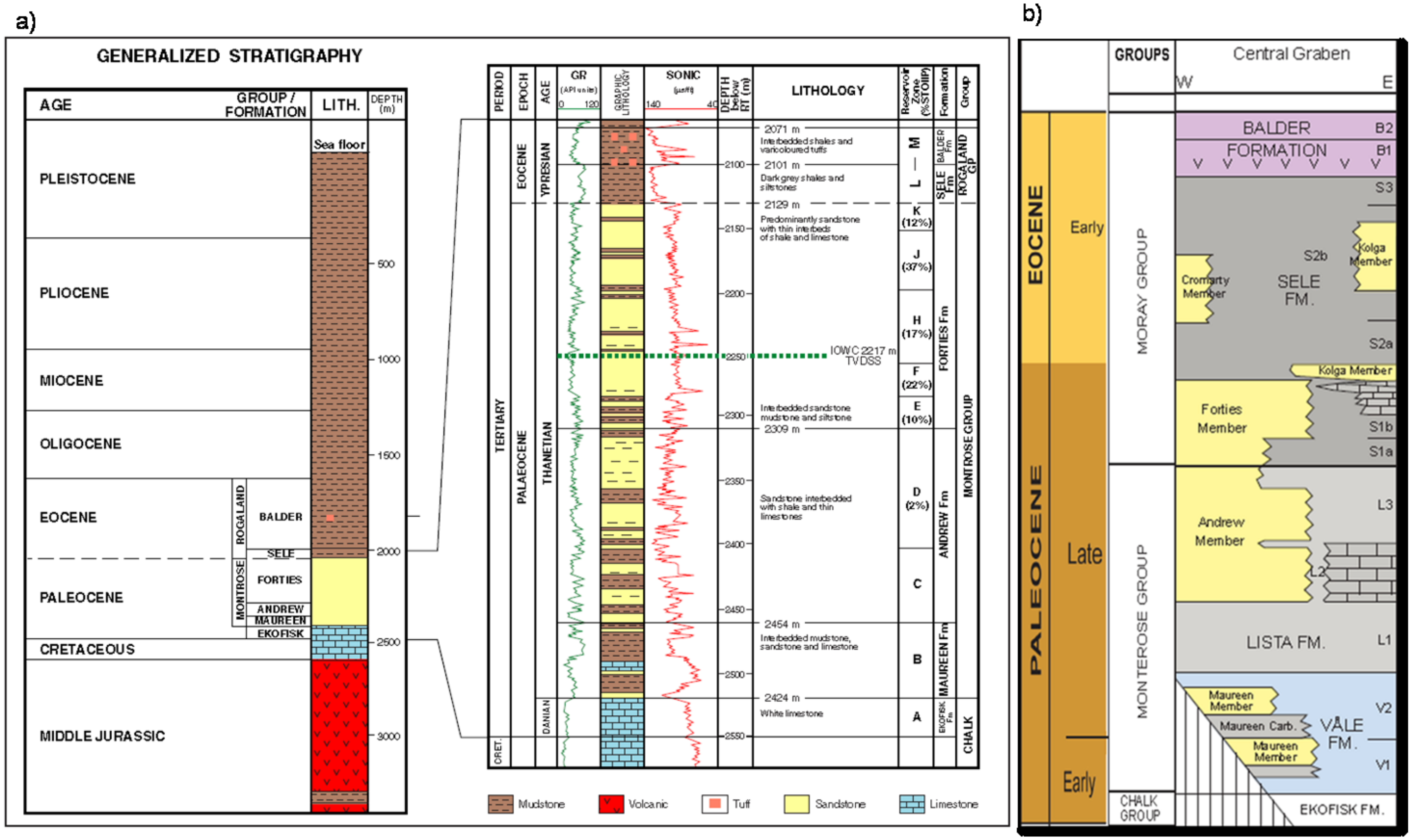

Figure 2.1. Stratigraphic column of the Forties field derived from the exploration well 21/10-1 that shows (a) the old stratiraphic nomenclature (After Wills and Peattie, 1990) and (b) the new stratigraphic nomenclature for the reservoir zone (After Bujak and Mudge, 1994)

Producing units of the Forties sands are indicated by a blocky low Gamma Ray response and are typically clean, friable, with very poor sorting, but have excellent reservoir characteristics. The reservoir consists of amalgamated turbidite fan sands deposited in the area from northwest, forming NW-SE trending turbidite fan system, and reflecting the topography influenced by the boundary faults of the Forties-Montrose High (Figure 2.2) (Hempton et al., 2005).

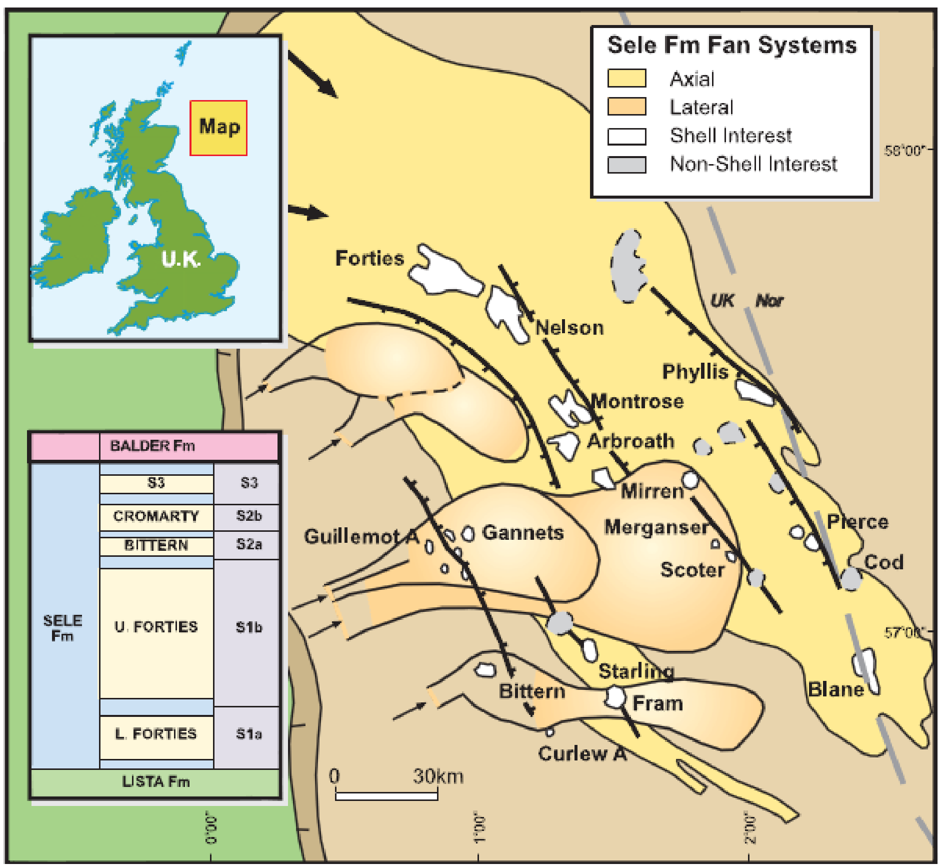

Figure 2.2. Regional sketch map of the Sele Formation showing the regional distribution of the turbidite reservoirs in the Central Graben, showing two major sources of the tubrbidite systems which deposited sands from the northwest, creating NW-SE trending turbidite fans, and from the west, creating E-W trending fans. Black arrows indicate inferred sediment flow directions (After Hempton et al., 2005).

Past work by the operators in integrating biostratigraphy, 3D seismic, well correlation, and reservoir engineering revealed reservoir zonations with differential pressured channel systems. Discovered and developed over time, the channel system now contains four major channel complexes: Alpha, Bravo, Delta-Echo, and Charlie (Figure 2.3). The reservoir sands are overlain by a regionally extensive shale of the Sele Formation that serves as the main vertical boundary for hydrocarbon movement. The Eocene Balder formation lies on top of the Sele Formation and is associated with the tuffaceous shales, giving rise to a strong acoustic impedance contrast in the seismic data (Hempton et al., 2005). See Appendix C for 3D seismic imaging of the reservoir turbidite sands and Balder formation faults using seismic attributes.

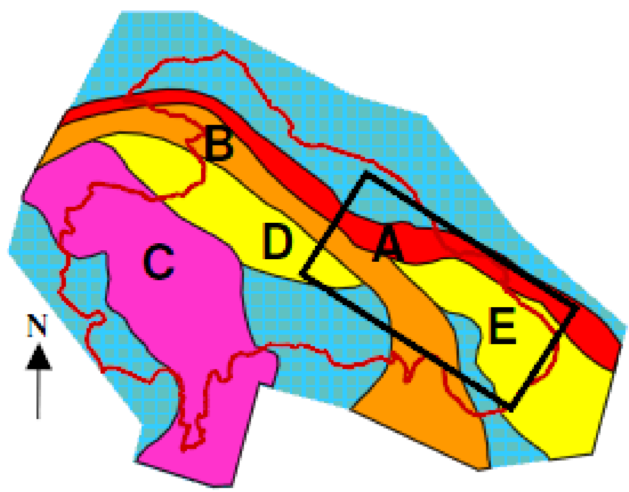

Figure 2.3. Sketch map of the distribution of channel system in the Forties field comprised of four major channel complexes of the Sele Formation: Alpha, Bravo, Delta-Echo, and Charlie, which were recognized as different sand members by use of integrated seismic mapping, well logs, reservoir engineering, and biostratigraphic data (After Ribeiro et al., 2007).

Tectonic History

The North Sea rift system is part of the Late Carboniferous Arctic-North Atlantic rift system, which started to develop during Permian and Triassic times and experienced five stages of geodynamic deformation. The oldest, part of the Caledonian basement underlies most of the North Sea, from south of Norway to the Danish part of the North Sea. This eastern part of the North Sea part of the Precambrian Fennoscandian Shield (Ziegler, 1992). The North Sea sedimentary basin started to develop after the Caledonian collision event that occurred during Late Ordovician to Early Silurian between the Laurentian basement in the west, the Baltic basement in the east, and Gondwana-derived terrain in the south, closing the Tethys Ocean (Nielsen et. al., 2000). This closure formed a line of weakness in the deep crust that controlled the subsequent Mesozoic graben system (Frederiksen et al., 2001).

Even though the initiation of the Central Graben has been interpreted early as the result of Mesozoic rifting event, the late Jurassic period is believed to be the most important extensional phase in forming the Viking and Central grabens in the North Sea basin (Frederiksen et al., 2001). The Triassic period did not experience significant volcanic activity in the North Sea basin and is marked by subsidence of the North Sea Rift system. During mid-Jurassic, at the junction of the Viking, Central and Moray Firth-Witch Ground grabens, a large volcanic center developed, depositing Permian, Triassic, and Early Jurassic sediments with a structural relief of 1500-2500 m in the flanks of the Central Graben. The late Jurassic – Early Cretaceous period is marked by a major rifting stage and occurrence of the convergent wrench faults system in the Viking, Central and Moray Firth-Witch Ground graben areas, resulting in orthogonal crustal stretching changing later to “dextral oblique extension” which could be related to the reorientation of the regional stress field (Ziegler, 1992). Whether the basin formation and initiation of the volcanism in the area is a thermal or plume active model, or an extensional or stretching passive model is contested (Smith and Ritchie, 1993). Latin and Waters (1992) argue that the Forties volcanic province, which lies in the triple-junction intersection of the three main rift arms, formed as a result of alkali basalt eruption triggered by lithospheric stretching.

Major controlling faults die out upwards towards Late Cretaceous-Paleocene sediments. This period accounts for major regional thermal subsidence and eustatically rising sea levels, which followed by deposition of thick chalk that reaches up to 2000 m in the Central Graben and thins towards the flanks. Senonian igneous rifting continued up to Paleocene that formed the British Isles and crustal separation between Greenland and Europe, which further infilled the Viking and Central grabens with prograding deltaic complexes. Density currents were triggered by slope failure and transported extensive sand fans into the deep-water troughs of the grabens. Exerted compressional stresses also inverted wrench faults in the southern part of the Central Graben that gradually die out northward (Ziegler, 1992).

Regional Paleostress Field in Northwestern Europe

Sippel et al. (2009) conducted an extensive study of the paleostress in the Central European Basin System, which divided the geodynamic history of the region into five main phases. The first phase includes initial rifting in the area and volcanic activity associated with the Variscan Orogeny. The collapse of the Variscan mountain chain resulted in N-S striking zones in the central North Sea and NW-SE striking zones in the southeast part of the basin during Late Carboniferous – Early Permian. The second phase of Early Permian – Early Triassic tectonic activity is marked by thermal subsidence of NW-SE oriented basin axes (Sippel et al., 2009). Hibsch et al. (1995) links the NNW-SSE oriented extension during the same period to the influence of the western Tethys rift system (Figure 2.4).

Subsequent changes in the tectonic regime occurred during Late Triassic – Jurassic, reactivating the Permo-Carboniferous fracture system trough from NNW-SSE striking extension system orientation to the ENE-WSW and E-W shown in Figure 2.5 (Hibsch et al., 1995). This period corresponds to the third phase, which correlates to the appearance of structural trends in the central North Sea, Viking and Central grabens (Sippel et al., 2009). During the Late Jurassic – Early Cretaceous the North Sea was affected by oblique extension (Figure 2.6). NE-SW striking faults in the Moray Firth Basin indicate E-W extension (Hibsch et al., 1995).

The fourth phase corresponds to the inversion of mainly NW-SE striking blocks along the Central European Basin margin during the Late Cretaceous – Early Ceonozoic. The compressional stresses during this time are due to combination of both: the opening of the North Atlantic, and Alpine collision of Africa and Europe. Cenozoic subsidence with a major depocentre located in the Central North Sea that had mainly N-S striking axes is marked as the fifth and final phase in the region (Sippel et al., 2009).

Overall, the Western Europe stress field orientation trends N 145^{o}E +/- 25^{o}, based on observations of stress indicators from borehole breakouts, fault slip vectors, focal mechanisms, overcoring, and hydraulic fracturing (Figure 2.7). The observed mean of maximum horizontal stress (S_{Hmax}) is subparallel to the Central Graben major strike orientation (Figure 2.8). Figure 2.8 shows how the horizontal stress field locally has a bimodal distribution of the orientation. Solid arrows represent mode I S_{Hmax} orientation that is parallel to the strike of the Central Graben, and open arrows represent mode II S_{Hmax} orientation that is perpendicular to the structure (Spann et al., 1994). Spann et al. (1994) modeled the local stress field of the Central Graben using finite element analysis, where two materials with different properties were used in the model. The study showed that the contrast between the materials can affect stress orientations and the magnitudes (Spann et al., 1994).

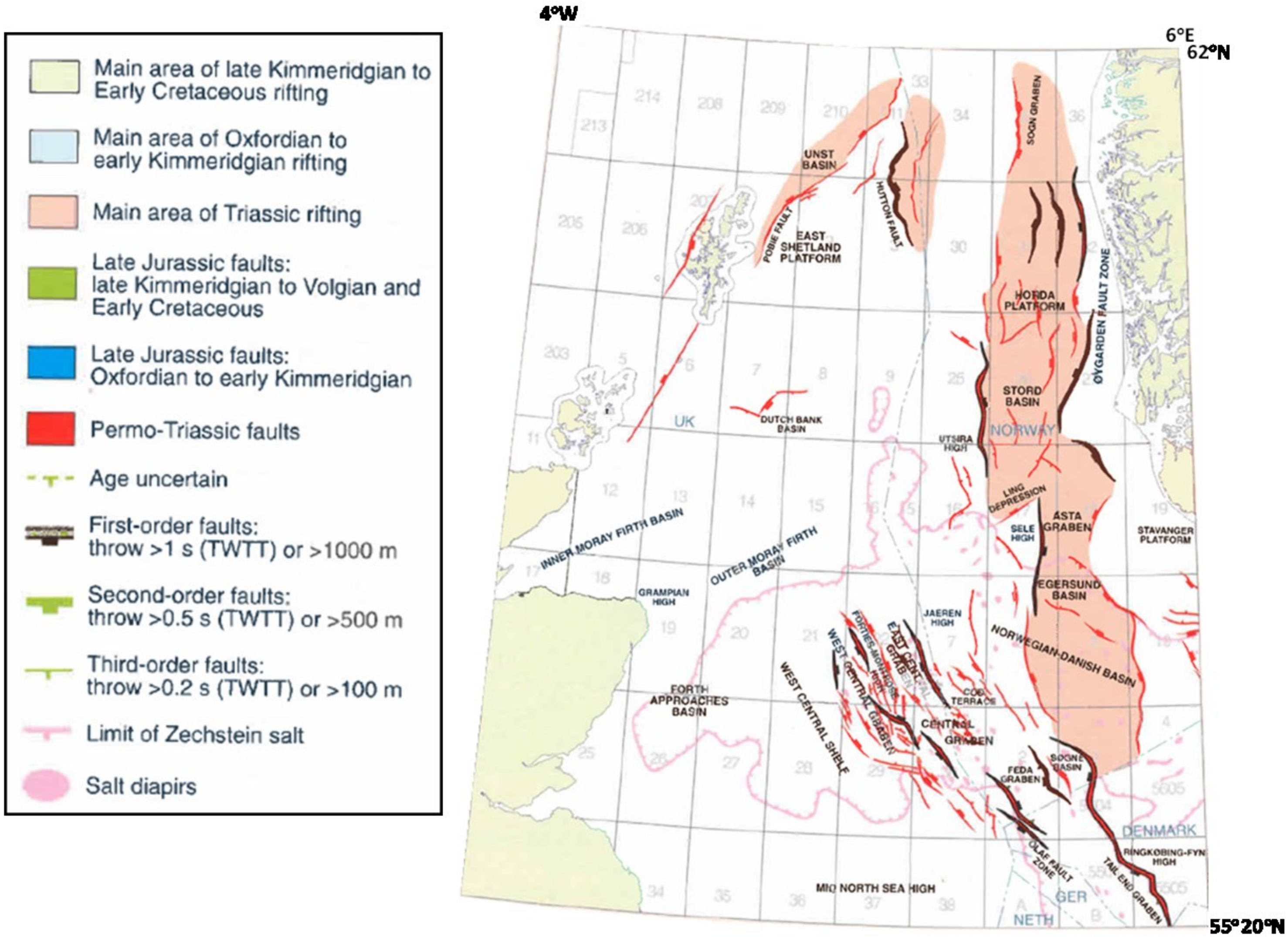

Figure 2.4. Rifting patterns of Permo-Triassic tectonic activity characterized by the NNW-SSE oriented faults blocks (After Zanella and Coward, 2003).

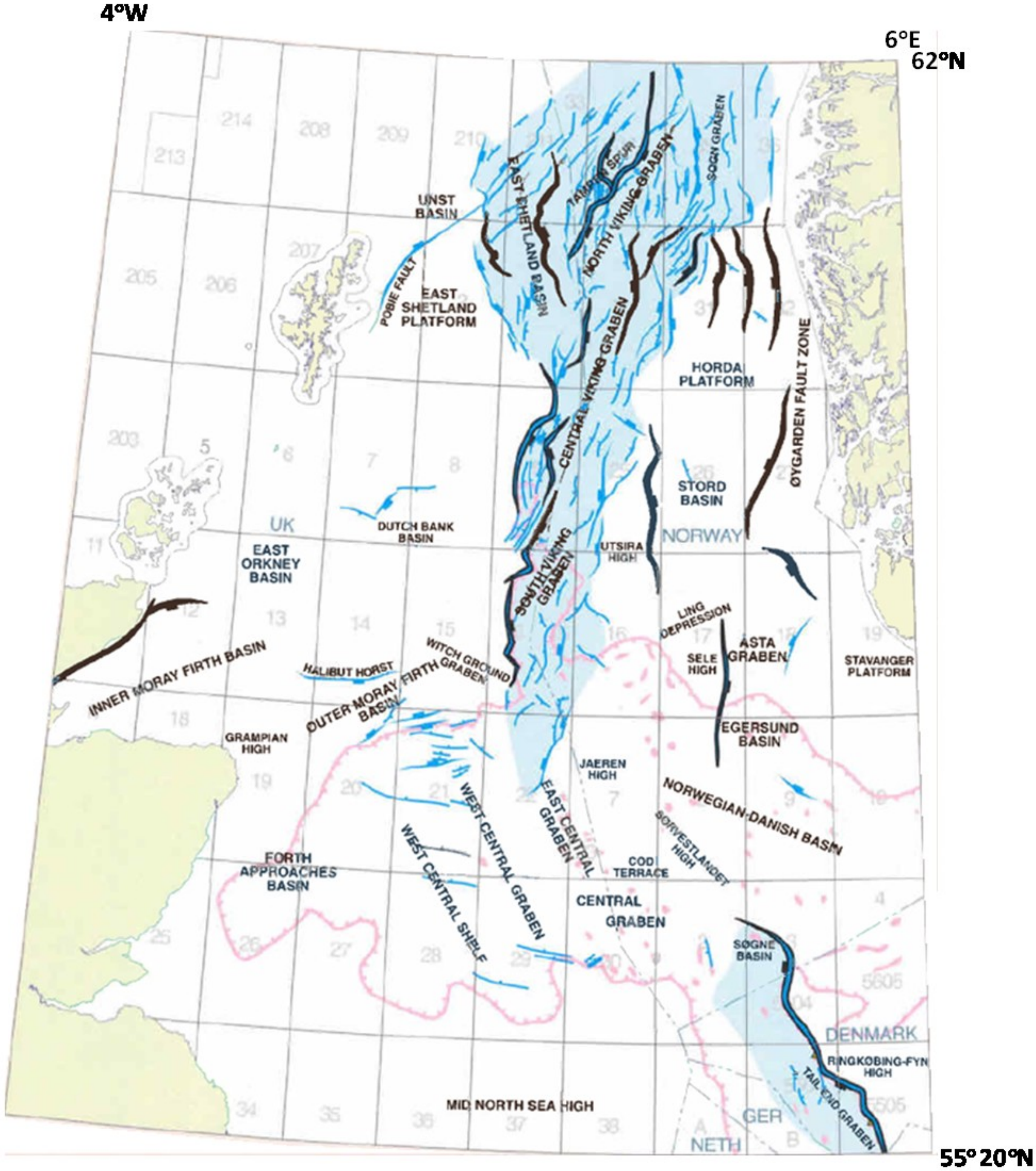

Figure 2.5. Rifting patterns of Late Triassic-Oxfordian tectonic activity characterized by reactivation of Permo-Triassic orientation of the faults to ENE-WSW and E-W. Look for color legend in Figure 2.4 (After Zanella and Coward, 2003).

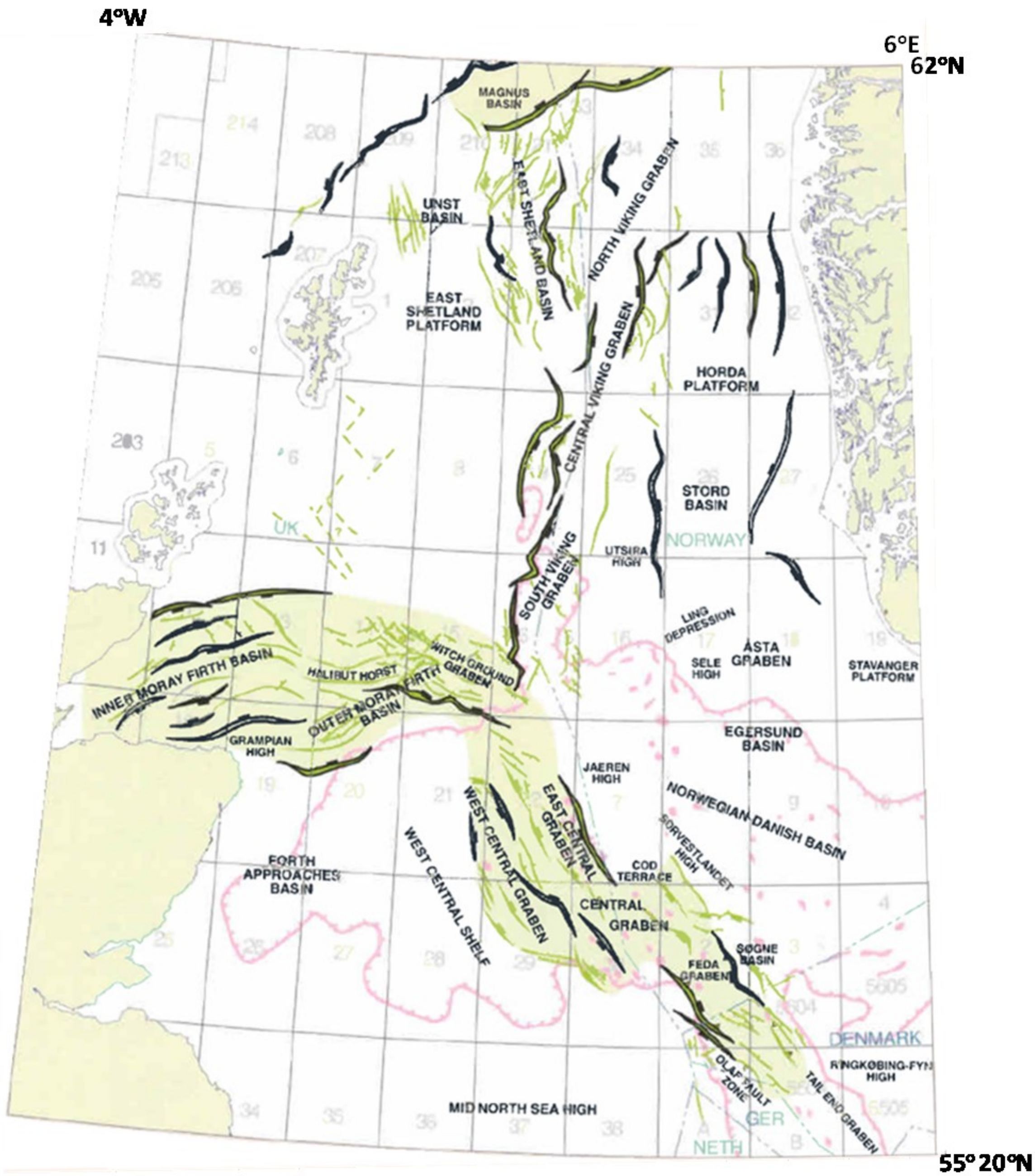

Figure 2.6. Rifting patterns of Late Jurassic - Early Cretaceous tectonic activity characterized by oblique extension and reactivation of earlier structures as strike-slip faults. Look for color legend in Figure 2.4 (After Zanella and Coward, 2003).

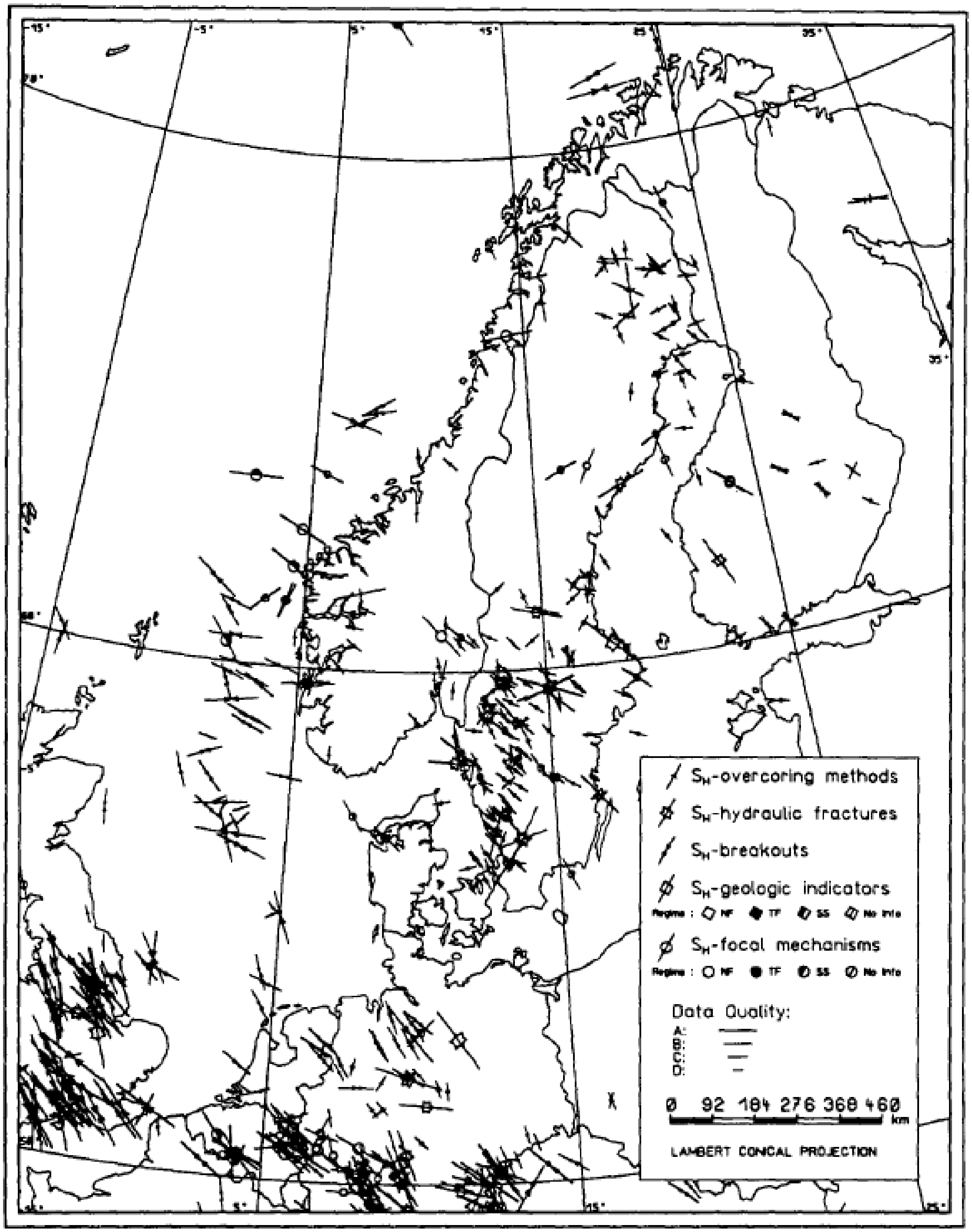

Figure 2.7. Part of the World Stress Map showing observed N 145°E +/- 25° stress orientation trend in the Central North Sea (After Spann et al., 1994).

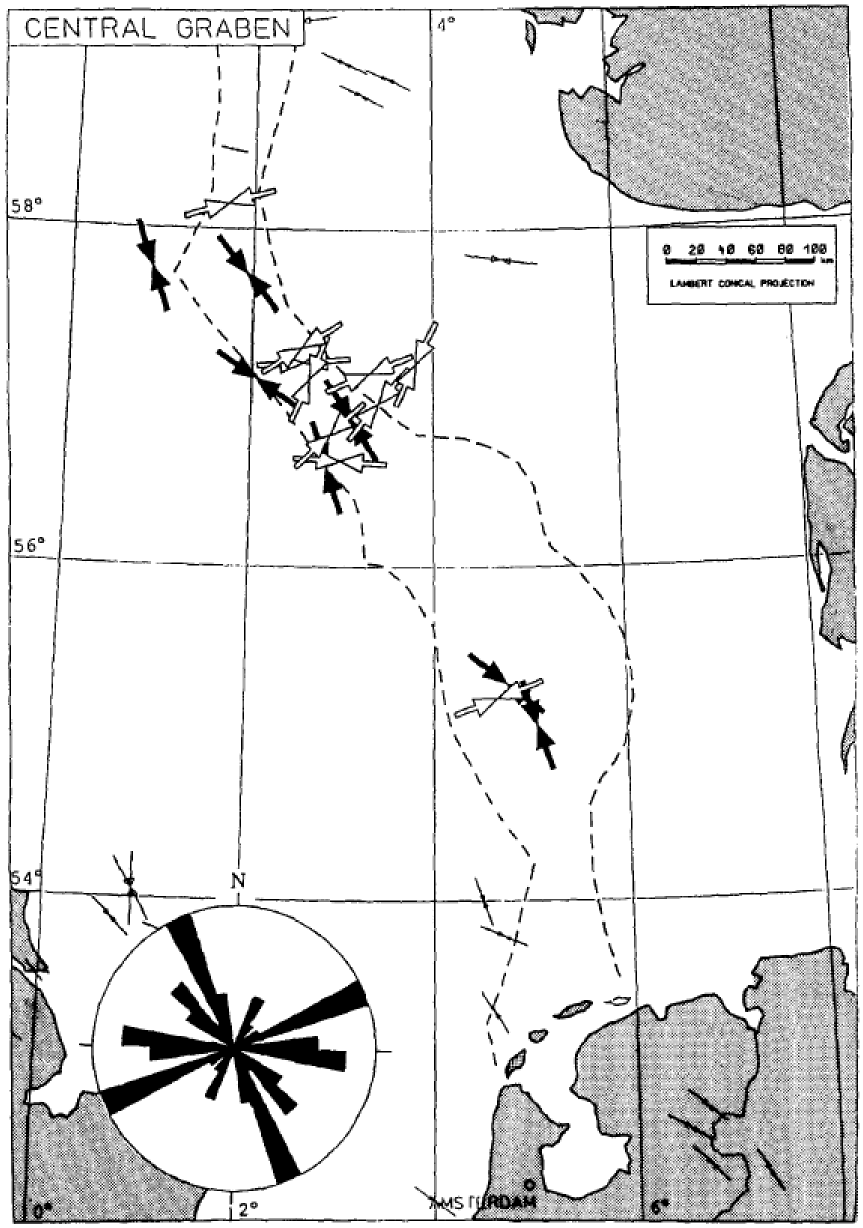

Figure 2.8. Map of the Central Graben showing orientation of the maximum principal horizontal stresses, S_{Hmax}. The solid arrows represent mode I, orientation of S_{Hmax} sub-parallel to the graben and white mode II arrows, orientation of S_{Hmax} perpendicular to the graben (After Spann et al., 1994).

CHAPTER III

THEORETICAL BACKGROUND - FAULT SLIP ANALYSIS

Geomechanics – Basic Principles

In continuum mechanics, stress is a measure of force acting over a homogeneous body. Forces acting on an infinitesimal volume of a body, represented as a cube $dV=dx_1\ dx_2\ dx_3$, within a large continuous medium in three dimensions can be described by a nine component stress tensor, **s**, 3.1, where normal stresses acting on the planes are perpendicular to them and the shear stress vectors are parallel to the planes (Figure 3.1a):

$$\mathbf{s} = \begin{bmatrix} s_{11} & s_{12} & s_{13} \\ s_{21} & s_{22} & s_{23} \\ s_{31} & s_{32} & s_{33} \end{bmatrix} \tag{3.1}$$

Assuming that external random stresses acting on the cube are larger than the normal and shear stresses, we can reorient the cube through tensor transformation in such a way that these external stresses become normal to the plane as denoted as S_1, S_2, and S_3 (Figure 3.1b). This rotation results in the shear stresses becoming zero and the principal stresses, S_i, on the diagonal, reducing the above matrix representing stress tensor to:

$$\mathbf{S} = \begin{bmatrix} S_1 & 0 & 0 \\ 0 & S_2 & 0 \\ 0 & 0 & S_3 \end{bmatrix} \tag{3.2}$$

Assuming that the overburden, S_v, is the largest acting stress on the rock, such that $S_1 = S_v$, and the remaining horizontal stresses S_2 and S_3 are maximum, S_{Hmax}, and minimum, S_{hmin}, horizontal stresses, respectively. E. M. Anderson's classification scheme, shown in Figure 3.2, relates the principal stresses acting on the rock in terms of the type of faults and geologic stress regime (Zoback, 2007).

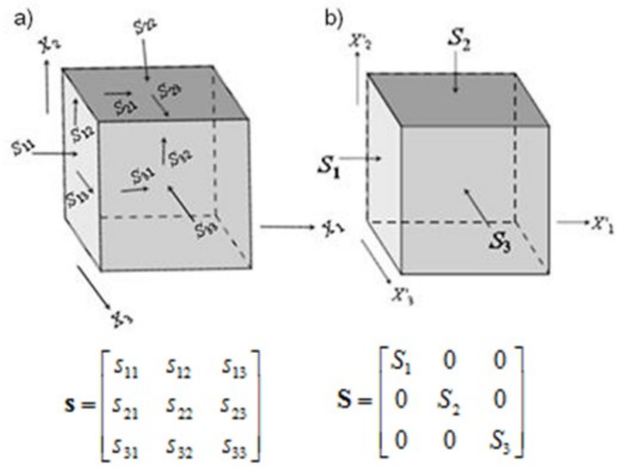

Figure 3.1. Cube showing (a) a nine component stress tensor acting on all six faces in an arbitrary Cartesian coordinate system with normal stresses acting perpendicular and shear stresses acting parallel to the planes. (b) Reorienting the cube such that only diagonal, principal stresses, S_i, remain (After Zoback, 2007).

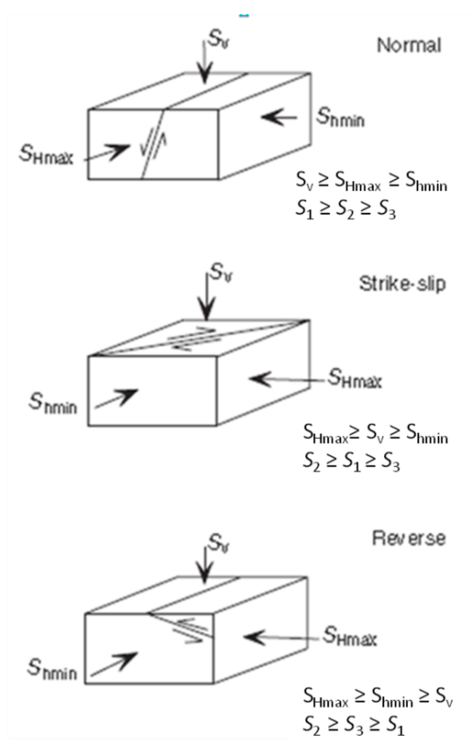

Figure 3.2. Anderson's classification scheme relating stress magnitudes to fault types and geologic stress regime (After Zoback, 2007).

Rock failure occurs under extension when the rock strength cannot sustain the local compressive stresses. Shear or tensile faults form as a result Figure 3.3 shows a sample triaxial strength test, where effective stresses are $\sigma_1 > \sigma_2 = \sigma_3$, σ_n is the effective normal stress on the fault, and β is the angle between the fault normal and σ_1. Effective stress is the stress acting on a body of rock with pore space inclusions, such that it is a difference between principal stresses, S_i and pore pressure P_p. A graphical evaluation of stresses and rock strength can be depicted using Mohr's circle, where effective normal stress σ_n is plotted against shear stress τ. The Mohr's circle represents the failure process or fault formation in terms of the effective principal stresses σ_1 and σ_3 (Figure 3.4) (Zoback, 2007), where

$$\sigma_1 - \sigma_3) \sin 2\beta \tag{3.3}$$

$$\sigma_n \qquad \sigma_1 + \sigma_3) + 0.5(\sigma_1 - \sigma_3) \cos 2\beta \tag{3.4}$$

In Figure 3.4, the Mohr's failure envelope is defined as a straight line that is tangent to the stress state "circle". The slope of the line is called coefficient of internal friction, γ. The shear stress intercept, when $\sigma_3 = 0$, is called cohesive strength, C_0:

, (3.5)

or

, (3.6)

where is an angle of internal friction that is based on the geometry and is described as $90^\circ - 2\beta$ (Davis and Reynolds, 1996). The unconfined compressive strength (UCS) is the strength of the rock before it fails under uniaxial compression (Zoback, 2007).

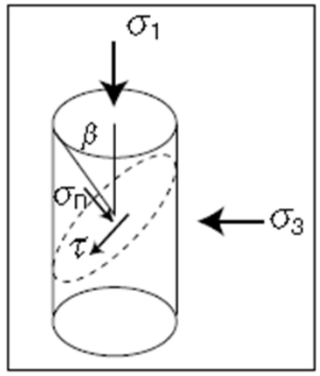

Figure 3.3. Illustration of triaxial experiment to measure rock strength. Rock failure occurs as a through-going fault as a result of the effective principal stresses acting on the rock mass (After Zoback, 2007).

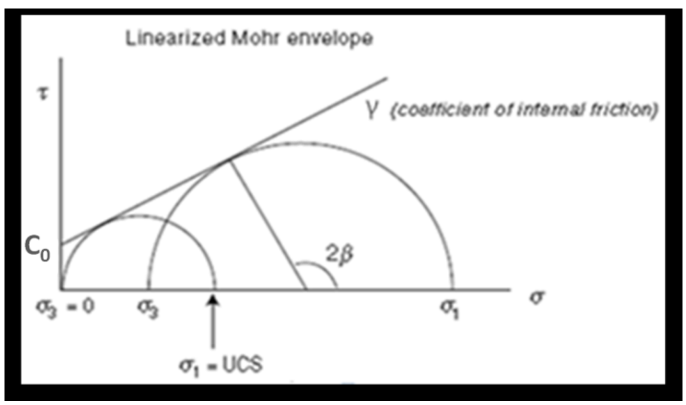

Figure 3.4. Mohr's failure envelope representing shear and effective normal stresses in terms of the effective principal stresses σ_1 and σ_3. Slope of the failure line provides the coefficient of internal friction, γ. The cohesive strength, C_0, is intercept of the failure line for $\sigma_3 = 0$ (After Zoback, 2007).

Fault Slip Theory

Donath (1966), Jaeger et al. (2007), and Zoback (2007) studied fault weakness and sliding on a plane of weakness. Fault weakness depends on its frictional strength and it cohesion. When the ratio of the shear to the effective normal stress on the fault exceeds the frictional strength, fault slippage occurs, causing reactivation of the discontinuity (Zoback, 2007):

$$\frac{\sigma_1}{\sigma_3} \le \left[\left(\gamma^2 + 1\right)^{1/2} + \gamma\right]^2 \qquad (3.7)$$

Roegiers (2011) uses constraints on the coefficient of friction, γ, as well as on the dip angles of the fault plane, β_1 and β_2, to determine which faults are the most prone to slip (Figure 3.5):

$$\beta_{1,2} = \frac{\pi}{2} - \frac{1}{2}\arccos\left[\frac{\gamma}{\left(1+\gamma^2\right)^{1/2}}\right] \pm \frac{1}{2}\arccos\left[\frac{\gamma}{\left(1+\gamma^2\right)^{1/2}}\frac{\sigma_1+\sigma_3}{\sigma_1-\sigma_3}\right]. \qquad (3.8)$$

The derivation of the above equation is shown in Appendix A.

The slippage of the fault was also analyzed using Mohr diagram shown in Figure 3.5 (Jaeger et al., 2007; Roegiers, 2011), where the region of the slip is defined as the intersection of the line of rock failure with the Mohr's circle. In order to find the region of the slip, a Mohr's circle can be constructed that corresponds to the weakness planes (Figure 3.5), by knowing the values of effective stresses, σ_1 and σ_3, and angle of coefficient friction, φ. The coefficient of friction, γ, depends on the nature of the properties of pre-existing plane of weakness or faults that affects the unconfined compressive strength (UCS) of the rock.

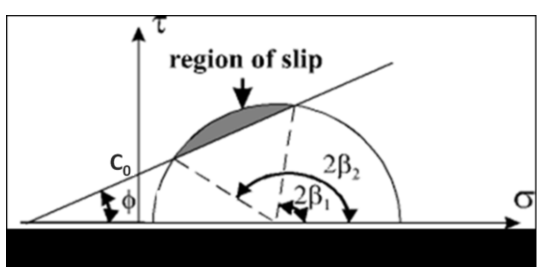

Figure 3.5. Mohr circle showing effective stresses and existing region of slip (After Roegiers, 2011).

Rock Strength Estimation from Well Logs

Fault slip and the Mohr circle also depend on the rock failure in compression and constitutes one of the variables that affects the coefficient of friction, γ. Termed as the unconfined compressive strength (UCS) it is represented in the Mohr circle (Figure 3.4) as the strength of the rock at a peak stress level of deformation, after which it starts to "strain soften" or weaken (Zoback, 2007). Zoback (2007) provides other factors that affect rock strength including rock properties such as elastic moduli and porosities. These properties can be estimated by prestack inversion of surface seismic data. Chang et al. (2006) provide several empirical relationships between UCS and geophysical logs: velocity, porosity, density, and Young modulus. As with any empirical relationships, there are pitfalls associated with using these estimations. The formulas depend on different assumptions, which include type of rock and its physical properties, geographic location, and age. Careful conditioning and calibration should be considered before accepting the estimations. Laboratory measurements using cores from different locations conclude that the strength of the rock, UCS, is inversely proportional to DT and porosity, ϕ, and has a positive correlation with Young Modulus, *E,* as shown in Figure 3.6. For this study, I used and compared Horsrud's (2001) and Lal's (1999) UCS estimations derived from Tertiary shales in the North Sea, defined in Table 3.1.

UCS, MPa	**Region where developed**	**Comments**	**Reference**
$0.77(304.8/\Delta t)^{2.93}$	North Sea	Mostly high porosity Tertiary shales	Horsrud (2001)
$10(304.8/\Delta t-1)$	North Sea	Mostly high porosity Tertiary shales	Lal (1999)

Table 3.1. Empirical relationships between UCS and sonic log values, Δt.

Δt is measured in μs/ft.

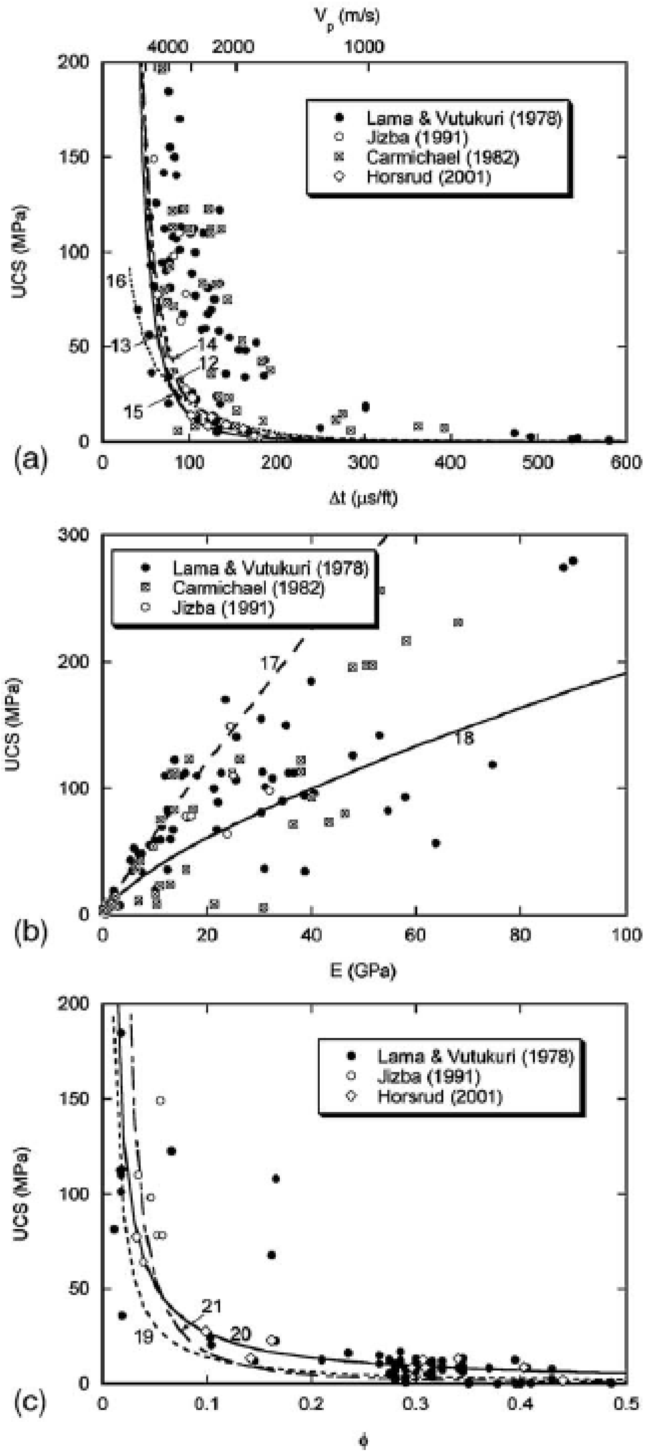

Figure 3.6. Labaratory measurements of shale rock properties, used to derive an empirical relationship between (a) DT, Δt, and UCS, (b) porosity, Φ, and UCS, and (c) Young Modulus, E, and UCS (After Chang et al., 2006).

Measuring In Situ Stresses

Zoback (2007) describes different techniques for measuring in situ stresses at depth. Since the study area mainly includes half grabens with normal faults, a normal fault regime will be assumed in the remainder of this thesis with overburden vertical stress, S_v, being the major principal stress and minimum horizontal principal stress S_3 = S_{hmin}. S_v consists of the integration of rock densities from the surface to a certain depth, z, with added seawater column:

$$S_V = \rho_w g z_w + \int_{z_W}^{z} \rho(z) g\,dz \tag{3.9}$$

Equation 3.9 provides a means of estimating S_v from integration of density logs from the wells in the study area.

The magnitude of the least principal stress, S_{hmin}, can be obtained from the leak-off tests (LOT) performed in the wells. In normal fault environment, S_{hmin} is equivalent to S_3 (Figure 3.3) (Zoback, 2007). A LOT is used to determine the mud density parameters needed at the maximum borehole pressure that can be applied. After casing is set in the borehole, the LOT requires the engineer to drill further distance of about 3 m to open hole below a casing shoe (Figure 3.7). A pumping pressure test, LOT, is then carried out. The drilling fluid is then sent from a cementing pump to pressurize the casing shoe, which results in the volumetric compression of the drilling mud column and expansion of the casing string and rock. The LOT reading is taken after the leak-off pressure (LOP) is reached, when the fluid diffuses into formation at a rapid rate and dilates the rock (Lin et al., 2008). There are number of issues and limitations of the LOT for stress estimation. Besides poor LOT measurements in the field, the error associated with LOT includes the assumption of an infinite long borehole thus plane strain condition. The interpretation of the LOT includes a two dimensional solution of the stress around the borehole, represented as a cross-section perpendicular to the axis of the borehole. The error arises from the exclusion of the bottom of the borehole as a three-dimension stress concentration (Lorwongngam, 2008). In order to decrease the error of the stress magnitude estimation extended-LOT measurements should be considered; however, only LOT measurements were available in this field.

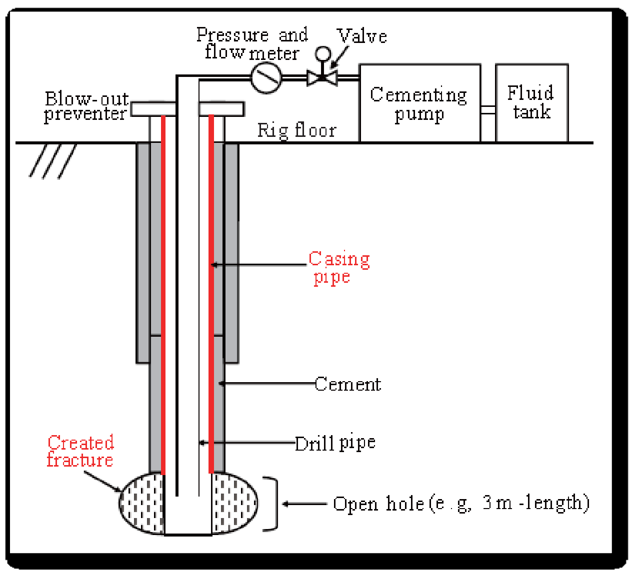

Figure 3.7. Schematic borehole configuration during a leak-off test (LOT) (After Lin et al., 2008).

Fault slide depends on the frictional strength of the rock, which varies between $0.6 \leq \gamma \leq 1.0$ (Zoback, 2007). Zoback (2007) quoted that "John Jaeger, perhaps the leading figure in rock mechanics of the twentieth century, once said: There are only two things you need to know about friction. It is always 0.6, and it will always make a monkey out of you". For the normal fault environment the limiting ratio of principal stress magnitude given by equation 3.7, can be used to compare the measured and calculated values S_{hmin} for a given coefficient of friction, γ.

In normal faulting environment, assuming that the maximum horizontal principal stress, S_1, is vertical (Figure 3.8a), the direction of the least principal stress is expected to be perpendicular to the strike of the fault as seen on the top view of the normal fault in Figure 3.8b (Zoback, 2007). The orientation of the maximum horizontal stress, S_{Hmax}, is expected to be parallel to the strike of the normal fault (Figure 3.8b). Measurement of the magnitude of the maximum horizontal stress, S_{Hmax}, is more complicated than the other principal stresses and no direct measurement in the field exist to predict precise value of the stress. The reader is referred to Zoback and Healy (1992) and Zoback (2007) for more detailed discussion on the empirical relationships and constraining the other principal stress values to obtain S_{Hmax}.

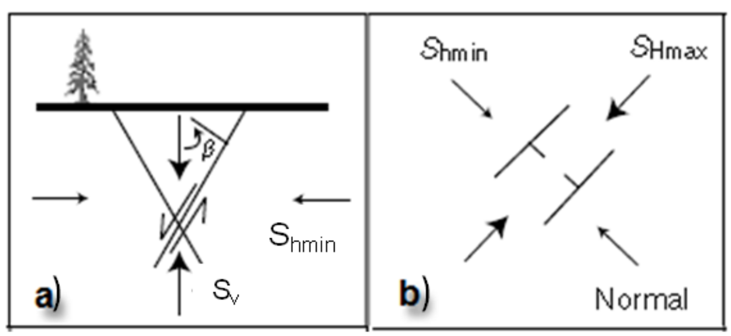

Figure 3.8. Schematic representation of normal fault regime and related stress orientation viewed (a) as a vertical cross-section in the subsurface and (b) from above (After Zoback, 2007).

Finally, in order to construct the Mohr envelope of failure to identify the region of possible fault slip, the pore pressure, P_p, has to be identified for the formation at depth. Several empirical relationships have been estimated using geophysical logs and seismic data described by Zoback (2007); however, the study of the pore pressure distribution over the Central Graben in the North Sea by Holm (1998) suggests that Paleocene sediments in the area are normally pressured. Pore pressure at depth is related to hydrostatic pressure associated with a column of water at depth that communicates with the sea floor:

$$P_p^{hydro} = \int_0^z \rho_w(z) g\,dz \approx \rho_w g z_w. \tag{3.10}$$

CHAPTER IV

THEORETICAL BACKGROUND - 3D SEISMIC ANALYSIS

Structural Filter

One of the objectives of this research is to improve seismic imaging of the faults within the Sele formation. The original 3D seismic data contained 1685 acquisition inline and 1281 acquisition crosslines with the distance of 12.5 meters between the lines. In this study I used partial-angle stacked 3D seismic data for the seismic attributes computation, and pre-stack seismic data for the inversion analysis. Table-4.1 describes the acquisition and processing parameters of the seismic data.

Acquisition Parameters
Data shot by vessel: WesternGeco Amundsen
Acquisition sample interval: 2 ms
Resampled seismic sample interval: 4ms
Number of cables: 11
Cable length: 3600 m
Number of groups: 571
Group Interval: 6.25
Shot interval: 12.5 m (flip-flop)
Record length: 4608 ms
Geodetic datum: ED50
Spheroid: International Hayford 1924
Projection: UTM
Central Meridian: 3E
UTM zone: 31N

Processig Sequence
Q digital group forming
Tidal static applied
Receiver motion correction
Deterministic water layer demultiple
τ dip filter in shot domain
τ dip filter in receiver domain
Global match filter
inverse Q (phase only)
4D binning
AMO regularization
Kirchoff prestack depth migration
Convert to time global match filter
Exponential gain
Bulk scaler
Offset variant scaler

Table 4.1. Acquisition and processing parameters of the original seismic data.

In this study, a structure oriented edge-preserving filter was used after the data was filtered out from noise. Figures 4.1 a and b compare unconditioned and conditioned data after structure-oriented edge-preserving filter within the area of study, where one can see smoother reflectors, improved delineation of structural features, and presentation of amplitude and frequency content. Details on structure-oriented filtering can be found in Davogustto (2011).

3D Seismic Attributes

Attribute assisted 3D seismic interpretation minimizes interpreter bias and enhances subtle geologic features. After conditioning the seismic data volume, structural features and major trends of principal horizontal stresses at the time of deformation based on the orientation of structures can be delineated using edge detecting attributes such as Sobel filters and coherence, and volumetric curvature.

Coherence attributes have long been used to visualize the spatial evolution of structural features within 3D seismic. Coherence aids in detection of discontinuities (faults) within the Sele formation by measuring similarity between waveforms and traces, which is inverse of variance attribute (Chopra and Marfurt, 2007). Another edge detecting attribute that is used in this study is the Sobel filter attribute. Sobel filter has been used in photographic digital image processing and then modified for seismic data by Luo et al. (1996). Sobel filter is a gradient-based edge detector that is commonly used in 2D or 3D signal processing. This filter takes into account the localization of the edges while enhancing the signal-to-noise. Therefore the resulted image is often much cleaner than the original, and the edges appear to be sharper than image produced by other filters of the same category such as coherence. In this study, coherence and Sobel filter volumes were computed along dip and azimuth of the reflectors.

Curvature attributes are widely used for structure delineation, highlighting 3D structures such as faults, valleys, ridges, domes, saddles, and bowls in seismic , as shown in previous works by Sigismondi and Soldo (2003), Chopra and Marfurt (2007 and

2010), and Roberts (2001). Mai et al. (2009) showed the relationship between curvature and normal faults, where the fault drag is directly associated with the curvature response Figure 4.2.

Mathematically, Roberts (2001) describes curvature as the rate of change of angle with respect to the arc length at a certain point in the curve. A circle exists at each point on the curve of the surface, which makes the circle tangent to the surface at the contact. The radius of the circle is defined as the radius of curvature. In a 2D cross-section through the surface, vectors which are normal to the surface define the type of curvature as shown in Figure 4.3. The vectors which are parallel to each other on a flat surface or constantly dipping correspond to zero curvature. The divergence or convergence of the vectors with each other corresponds to positive or negative curvature, respectively (Figure 4.3).

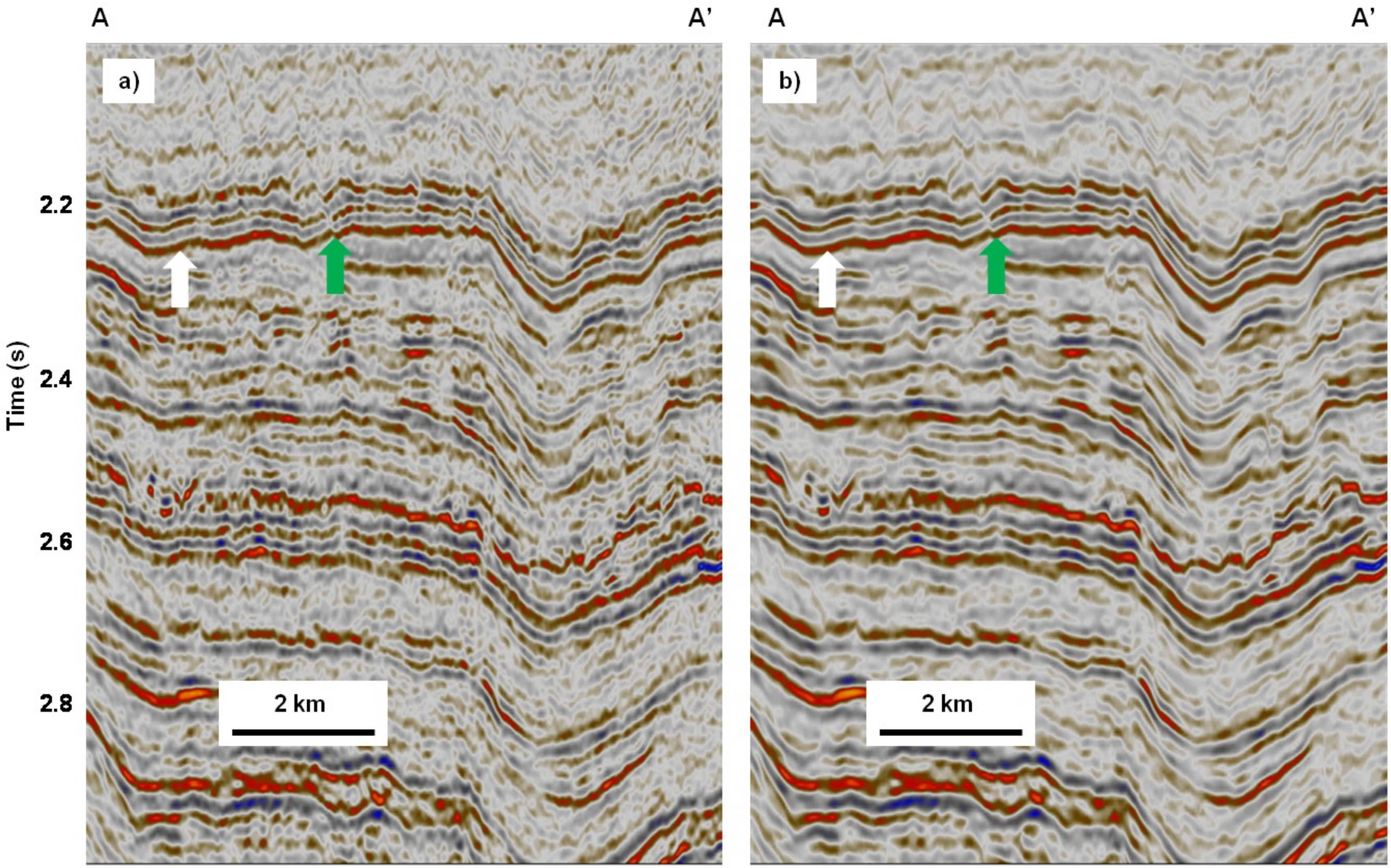
A
A'
a)
b)
Time (s)
2.2
2.4
2.6
2.8
2 km

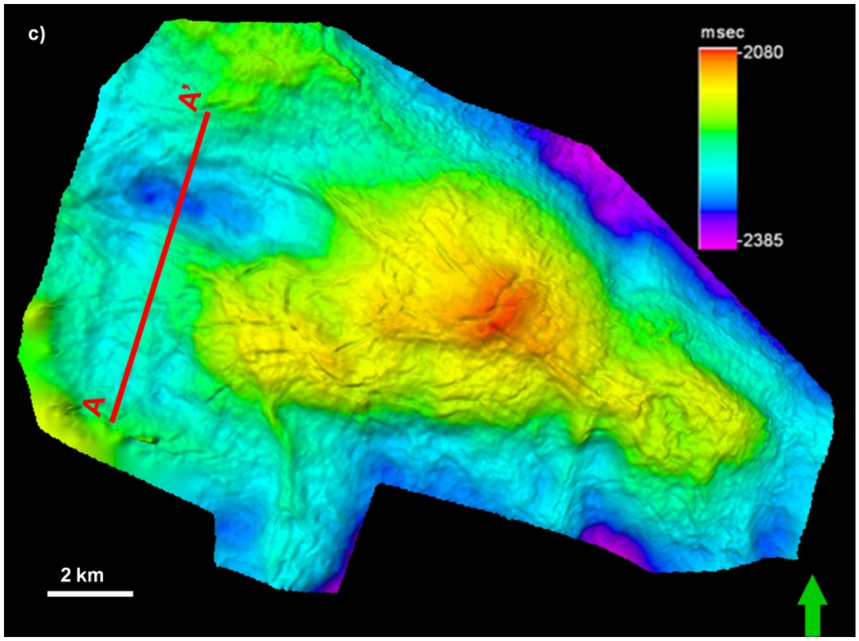

Figure 4.1. Vertical time slices through a) unconditioned and b) conditioned seismic amplitude volumes. Notice smoothing of the reflector, indicated by white arrow, and more pronounced discontinuities, indicated by green arrow, after conditioning the seismic using an edge-detecting structure-orineted filter. Location of the line is shown in c).

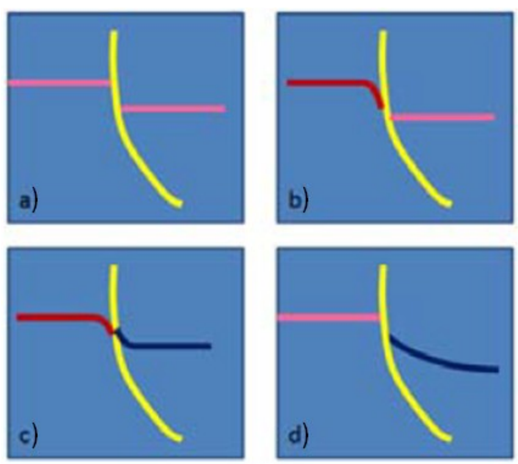

Figure 4. 2. Normal faults with different types of displacement associated with: (a) no drag of the surface on either side of the fault, (b) fault drag on one side of the fault, (c) fault drag on both sides of the fault, and (d) fault syntectonic deposition (After Mai et al., 2009).

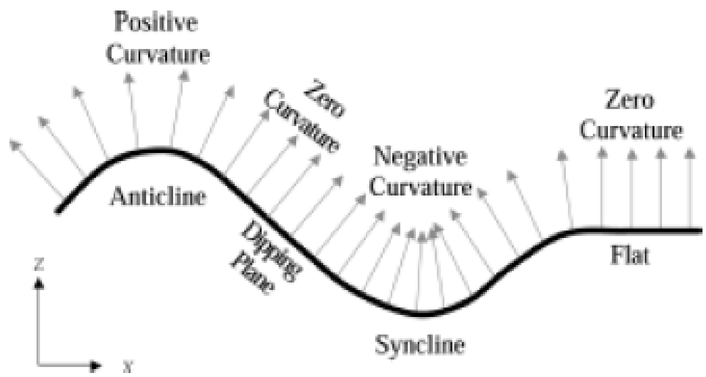

Figure 4.3. Two dimensional representation of curvature, showing positive and negative curvature by diverging and converging vectors normal to the surface, and vectors parallel to each other showing dipping or flat surface with zero curvature (After Roberts, 2001).

When considering curvature of the surface in 3D, note that many normals to the surface and orthogonal to each other can be drawn. For this reason, it is helpful to define principal curvatures, (k_1 and k_2 where $k_1 \geq k_2$), that represent the extreme values, and for quadratic surface, will be orthogonal to each other (Figure 4.4). Curvature analysis can be estimated volumetrically by computing the first derivatives of the components of apparent dip. Al-Dossary and Marfurt (2006) estimate the dip and azimuth of the reflector to honor geologic representation of structure, which is then used to compute the principal curvatures.

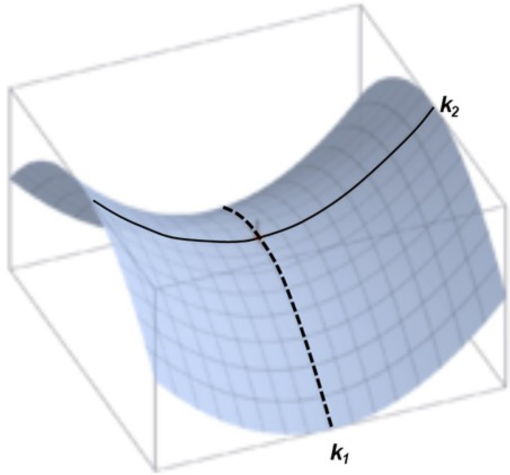

Figure 4.4. Three dimensional representation of curvature showing principal curvatures (k_1 and k_2) across a saddle. The most positive principal curvature, k_1, represents an anticlinal cross section in the image and is numerically larger than the apparent curvature in any other cross section. The most negative principal curvature, k_2, represents a synclinal cross section and is numerically less than the apparent curvature in any other cross section. For a quadratic surface (dome, ridge, saddle, valley, bowl, or plane) $k_1 \geq k_2$.

Elastic Impedance Inversion for Rock Strength Prediction

Seismic amplitudes are sensitive to impedance variation across an interface. Rock properties can be estimated through calibration of seismic reflectivity with recorded log information through seismic impedance inversion methods. As discussed in Chapter III, the rock strength affects the coefficient of friction, and also affects the stability of the borehole, which can be estimated using slowness measured on velocity logs. I will estimate impedance as an indicator of the rock property changes within the shale component of the Sele formation, and through well control relate these properties back to lateral variation of the rock strength.

Seismic impedance inversion is the inverse of forward modeling. I deconvolve seismic trace using an estimate of the bandlimited wavelet. The normal incidence reflectivity of the subsurface represents a bandlimited estimate of acoustic impedance, product of density and velocity (Hampson and Russell, 2006):

$$r_{Pi} = \frac{Z_{Pi+1} - Z_{Pi}}{Z_{Pi+1} + Z_{Pi}} \tag{4.1}$$

where r_{Pi} is the zero-offset P-wave reflection coefficient at the i^{th} interface, and Z_{Pi} is the i^{th} layer's P-wave impedance. Because seismic data are contaminated by noise and are also bandlimited, there is no unique solution. The bandlimited wavelet source misses the low frequency response. This low frequency component is extracted from the low frequency component of well log data, and then added to the bandlimited seismic component. Seismic inversion on post-stack data can be used if there is no significant variation of amplitude with offset. As shown in Figure 4.5, interpretation of the top Sele formation horizon (Figures 4.5 c and d) using partial angle-stacked seismic volumes reveals the difference in the reflection response between the near-angle (Figure 4.5 a, c) and the mid-angle (Figure 4.5 b, d) offsets. The Sele formation top reflector changes from a positive value in near-angle stack (5^o-13^o) to a zero-crossing in the mid-angle stacks (29^o-37^o).

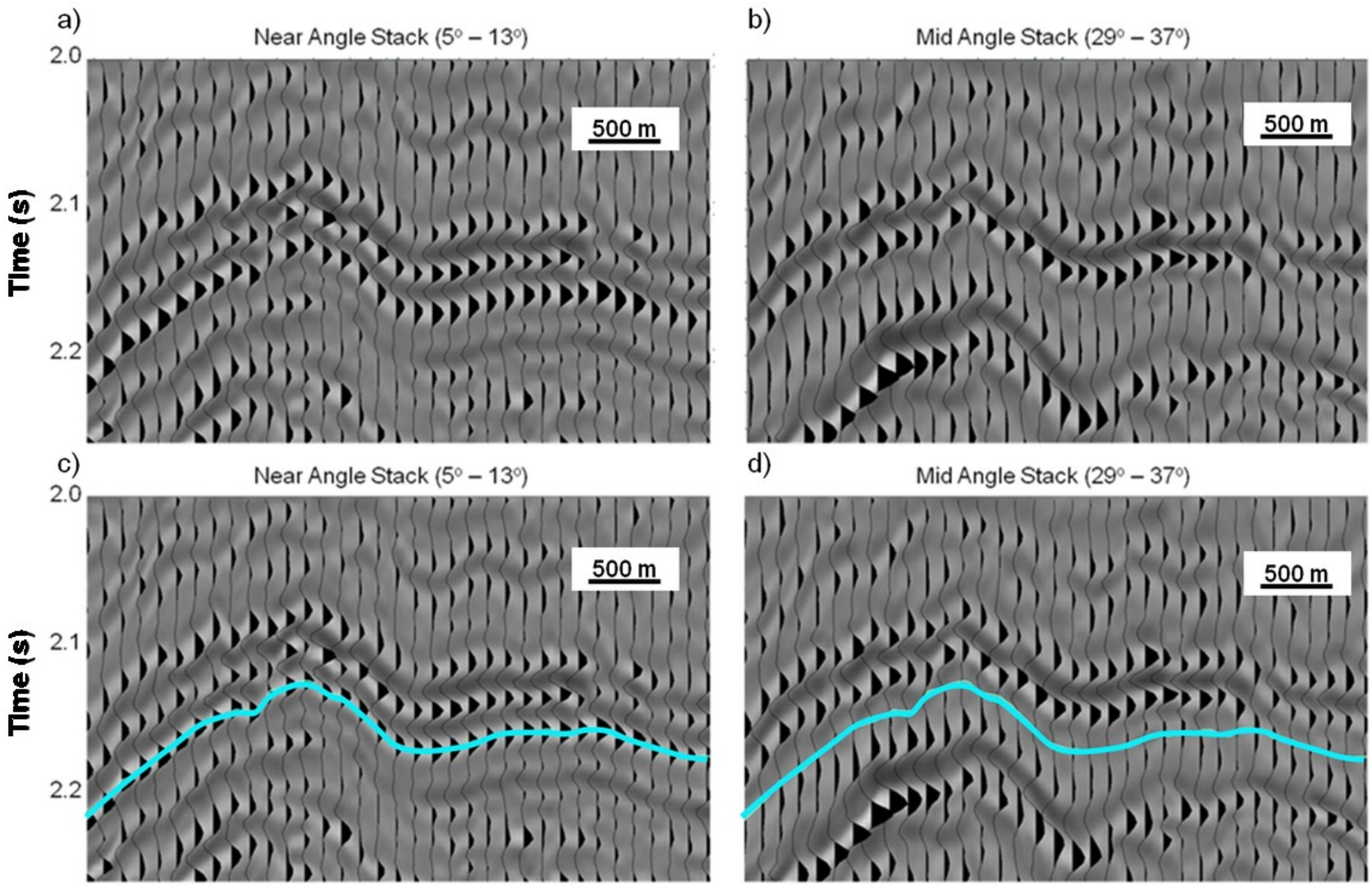

Figure 4.5. Vertical time slice through partial stack seismic amplitude volumes showing difference in amplitudes between (a) near-angle and (b) mid-angle stacks at the Sele formation. (c) and (d) the Sele formation shale top pick in cyan.

I interpreted this observation as a classical amplitude variation with offset (AVO) effect. An incident P-wave at an angle θ, results in reflected and transmitted P and S-waves (Figure 4.6). Aki and Richards (1980) linearized the Zoeppritz equation to obtain the reflection coefficient as a function of angle R(θ) for isotropic material:

$$R(\theta) \approx b_0 + b_1 \sin^2\theta + b_2 \left(\tan^2\theta - \sin^2\theta\right), \qquad (4.2)$$

where b_o is the intercept, b_1 the gradient, and b_2 the curvature defined as:

$$\begin{aligned} b_0 &= \frac{1}{2}\left(\frac{\Delta\rho}{\rho} + \frac{\Delta V_p}{V_p}\right) \\ b_1 &= \left[\frac{1}{2}\frac{\Delta V_p}{V_p} - 2\frac{V_s^2}{V_p^2}\frac{\Delta\mu}{\mu}\right] \\ b_2 &= \frac{1}{2}\frac{\Delta V_p}{V_p} \end{aligned} \qquad (4.3)$$

The b_o and b_1 of the equation 4.3 are useful for fluid and lithology detection, respectively. Although, the above equation describes AVO variation and was first used to estimate pore fluid and lithology changes, Goodway et al. (1997) propose using a modified approximation, where for small angles, the P- and S- wave impedance contrasts, ΔZ_P and ΔZ_S, can be estimated without the need for the density, ρ, value, which is challenging to estimate from seismic:

$$R(\theta) = (1+\tan^2\theta)\frac{\Delta Z_P}{2Z_P} - 8\left(\frac{V_S}{V_P}\right)^2 \sin^2\theta \frac{\Delta Z_S}{2Z_S} - \left(\frac{1}{2}\tan^2\theta - 2\left(\frac{V_S}{V_P}\right)^2 \sin^2\theta\right)\frac{\Delta\rho}{\rho} \qquad (4.4)$$

where ρ in the last term of approximation is small for small angles. Using commercial software, a pre-stack model-based inversion workflow inverted seismic data directly for Z_P and Z_S, and density volumes (Hampson and Russell, 2006). Using Lambda-Mu-Rho (LMR) transform modulus in Hampson-Russell, Lamé parameters, λρ and μρ, can be calculated using following relationships for isotropic materials:

$$\lambda\rho = Z_P^2 - 2Z_S^2 \qquad (4.5)$$

$$\mu\rho = Z_S^2 \qquad (4.6)$$

where λ and μ are fluid compressibility and rigidity (Goodway et al., 1997). Using Lamé elastic parameters, I assume in this study that the fluid, brine, within the shale rock does not change laterally, and only change in matrix of the rock or rigidity, μ, will indicate lateral change of the rock strength.

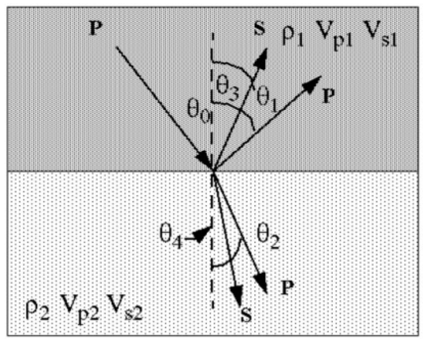

Figure 4.6. Mode conversion of the incident P-wave at angle θ resulting in reflected and transmitted P and S-waves (Aki and Richards, 1980).

In this study, fourteen near vertical-wells with compressional velocity, V_P, and density logs and six deviated wells with compressional, V_P, and shear velocity, V_S, and density logs available. V_S for wells without shear logs data were estimated using the relationship between V_P and V_S cross-plots shown in Figure 4.7. Figure 4.8 shows a comparison of the original V_S with the estimated V_S using the relationship from Figure 4.7. The correlation between the original and the estimated V_S is about 0.96. Conditioning of the pre-stack seismic data, well ties to seismic, and inversion analysis including comparison of created synthetics with original seismic for error estimation and QC are described in Appendix B.

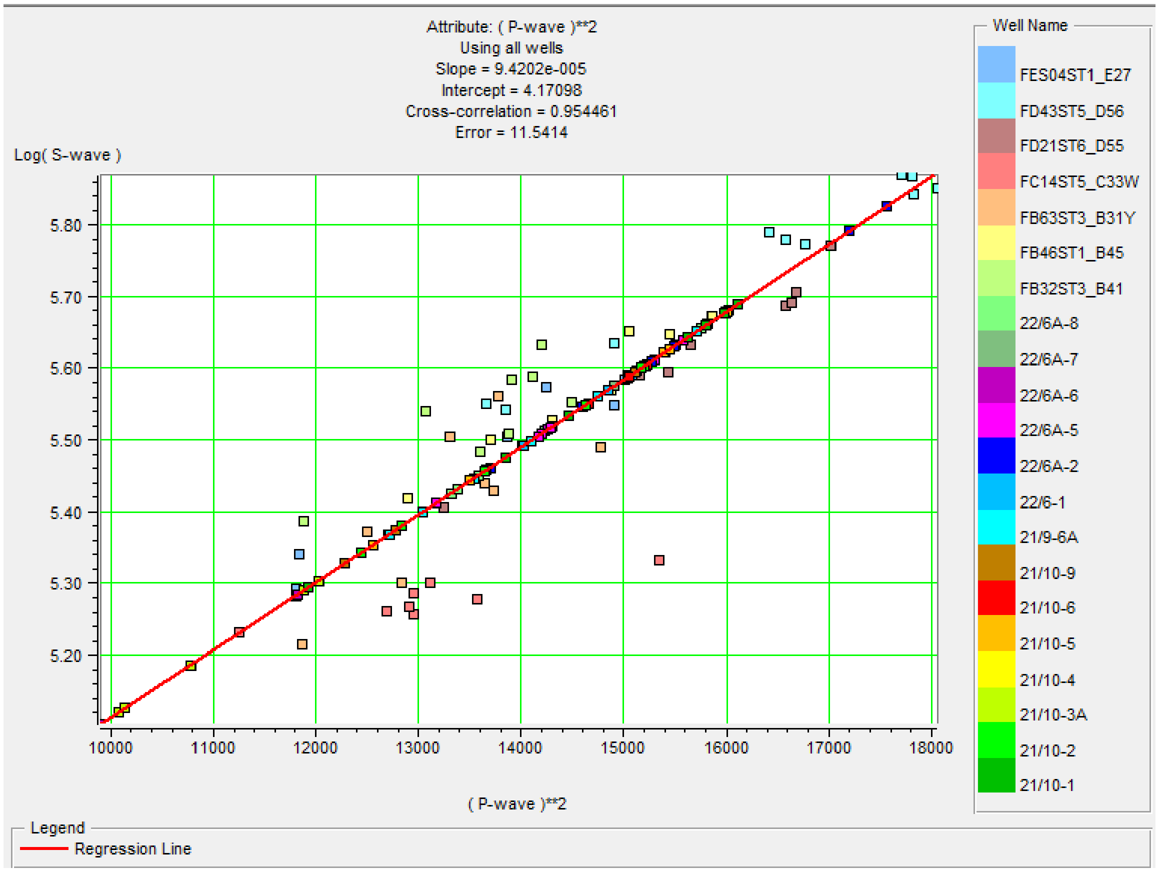

Figure 4.7. $V_P – V_S$ cross-plot using well logs in order to estimate V_S for the wells without recorded V_S. The colors in the cross-plot represent the wells, labeled on the right side of the figure.

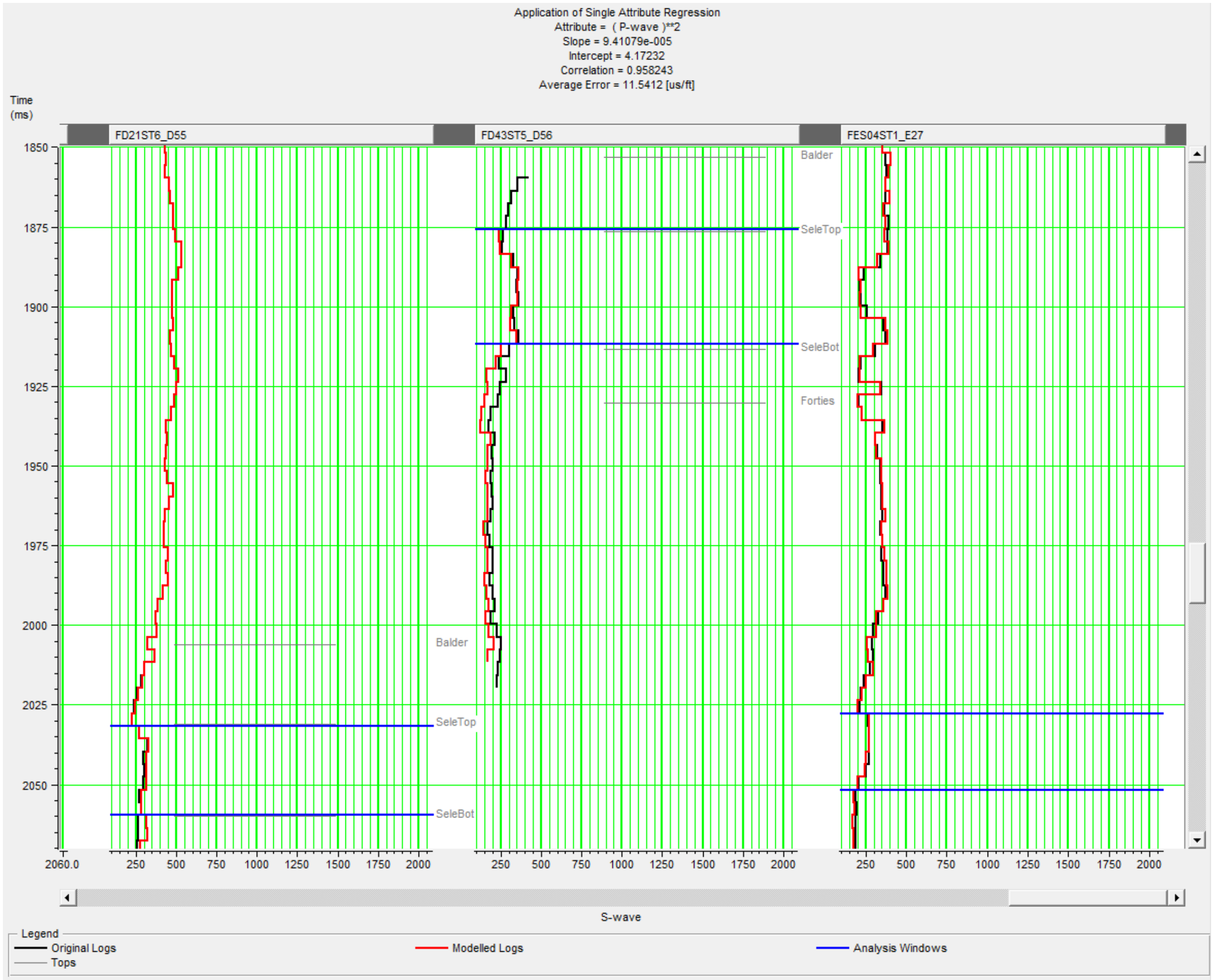

Figure 4.8. Comparison of the original V_S with the estimated V_S using the relationship between V_P and V_S shown in the Figure 4.7. The correlation between the original and estimated V_S is about 0.96 within the Sele formation window.

CHAPTER V

ANALYSIS – FORTIES FIELD GEOMECHANICS

Estimation of In-Situ Stresses

A geomechanical analysis of fault slip is based on the estimation of the principal stresses from constructed trend lines, which are then plotted as stress graphs in order to visualize the most prominent region for pre-existing fault plane to slip. The analysis includes several constructed scenarios where effective stresses change due to reservoir treatments. However, the most realistic case for the region of fault slip to occur under in-situ conditions is when the stress exceeds the failure envelope, governed by the coefficient of friction, γ.

The vertical major stress, Sv, was calculated using equation 3.9, where density of sea water, $\rho_w = 1.1$ g/cm^3 with $z_w = 116$m taken from White et al. (1974) and density values for subsurface taken from density log from a nearly vertical well. Pore pressure is assumed to be hydrostatic because the reservoir in the Forties field is normally pressured (Holm, 1998). The minimum principal stress was estimated from leak-off tests, LOT, measurements in the field that were taken up to the depth of the Balder shale formation that overlies the Sele formation. Figure 5.1 shows the constructed principal stress and pore pressure profile, where the trend lines were used to estimated stresses within the Sele formation.

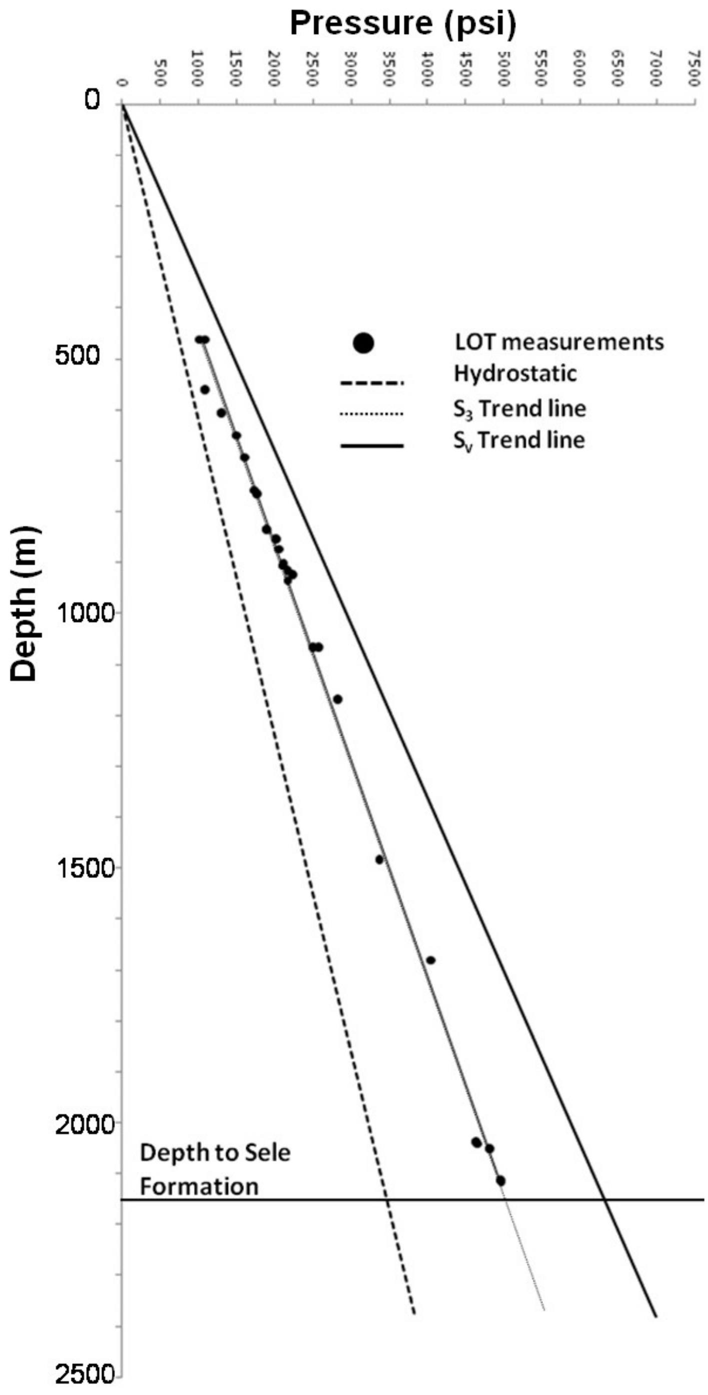

Figure 5.1. Pressure versus depth plot showing overburden vertical stress S_v (thick black line), calculated from the density log, horizontal minimum stress S_{hmin} trend line using LOT measurements from the wells in the area, (thin black line), and hydrostatic stress (dashed line).

Mohr Circle Construction

Effective stresses, σ_1 and σ_3, were calculated using values of principal stresses, **S**, and pore pressure found from Figure 5.1 shown in Table 5.1. Figure 5.2 shows the plotted effective stresses and corresponding Mohr circle with pre-existing fault line dipping at 40.5^o ($2\beta = 81^o$) measured from the vertical stress to normal stress of the dip. The linearized failure envelope in Figure 5.2 was constructed using a coefficient of friction, γ =0.6.

Stresses		psi
Vertical Max Principal Stress	$\mathbf{S_V}$	6400
Min Horizontal Principal Stress	$\mathbf{S_3}$	5000
Pore Pressure	P_p	3500
Effective Vertical Stress	σ_1	2900
Effective Min Horizontal Stress	σ_3	1500

Table 5.1. Effective vertical stress, σ_1 and horizontal minimum stress, σ_3 calculated from the principal stresses and pore pressure.

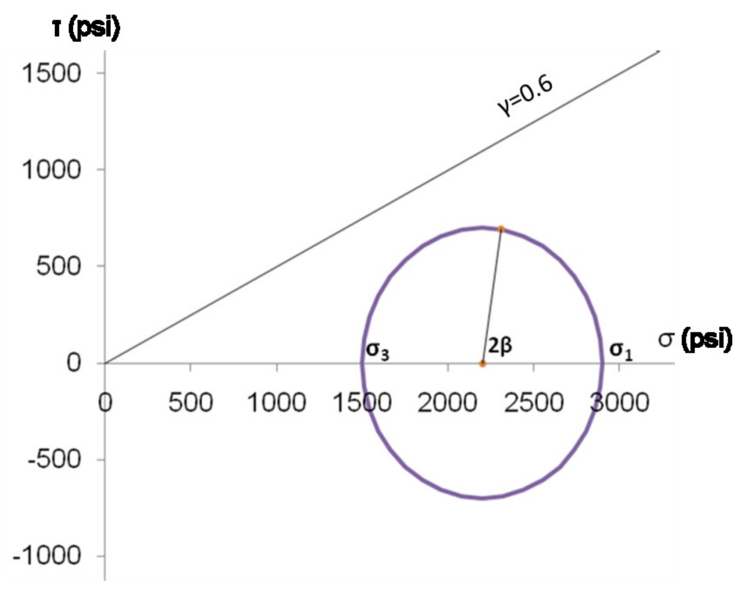

Figure 5.2. Representation of stresses through Mohr circle showing that with the current in-situ stresses and assumed coefficient of friction γ = 0.6, pre-existing faults with dip angle $\beta = 40.5^o$ are stable and will not experience slip.

Using estimated in situ principal stresses, one can observe that the Mohr circle does not touch the failure line when $\gamma = 0.6$ (Figure 5.2). Changes in pore pressure, as a result of reservoir depletion or injection, will give rise to changes in the effective stresses and corresponding changes in the Mohr circle. Figure 5.3a shows a uniform shift of Mohr circle as a result of depletion (decrease in pore pressure) and injection (increase in pore pressure) without any change in differential stress ($\sigma_1 - \sigma_3$). It is important to mention that a decrease in pore pressure is the most realistic case scenario, since the reservoir in the Forties field was normally pressured at the beginning of production, where reservoir depletion will result in pore pressure reduction. Uniform changes in both effective stresses only stabilize pre-existing faults by moving the Mohr circle further away from failure line (Figure 5.3a). In contrast, an increase in pore pressure is possible if the reservoir was overpressured at the beginning of production or caused by an overly aggressive injection program. However, the reservoir is normally pressured and no anomalous overpressure is observed in the Central Graben area within Paleocene sediments (Darby et al., 1996). Furthermore, current RFTs do not show any overpressure within the reservoir caused by injection. However, a small increase in pore pressure (by 1500 psi) may increase the propensity for faults to slip as the Mohr circle touches the failure line in Figure 5.3a.

Change in pore pressure also can change differential effective stress ($\sigma_1 - \sigma_3$) as plotted in Figure 5.3b. Hillis (2001) shows that the effective horizontal stress, σ_3, change slowly due to effect of changing pore pressure on horizontal principal stress (S_{Hmax}):

$$\Delta\ _{H\max} = (- \ \Delta\ _{P}, \tag{5.1}$$

where $k = 0.32$ is a constant calibrated by the coefficient of friction under assumption that $\gamma = 0.6$, and is described as:

$$k = \frac{1}{\left(\sqrt{\gamma^2 + 1} + \gamma\right)^2} \tag{5.2}$$

Change in pore pressure affects horizontal principal stress (S_{Hmax}) due to $P_P/\ \sigma_3$ coupling. A decrease in pore pressure increases the differential stress (σ_1- σ_3), whereas an increase in pore pressure decreases the differential stress (σ_1- σ_3). However, neither of these changes cause the Mohr circles to touch the failure line at any point (Figure 5.3b).

Plotting different scenarios of stress changes caused by pore pressure changes reveals that uniformly decreasing effective stresses caused by increasing the pore pressure is the only case where the pre-existing fault plane is prone to slip. Figure 5.4 shows that a decrease of a failure slope from $\gamma = 0.6$ is needed to intersect the Mohr circle with my measured in-situ stresses. As described in Chapter IV, the coefficient of friction is assumed to be between 0.6 and 1. One of the explanations for a decrease in the coefficient of friction could be due to known pre-existing sub-horizontal weakness planes (fractures) within the Sele formation that further decreases the rock strength. A decrease of rock strength and associated decrease of coefficient of friction hypothesis is in agreement with Jaeger and Cook's (1979) and Zoback's (2007) theories on associated rock strength anisotropy.

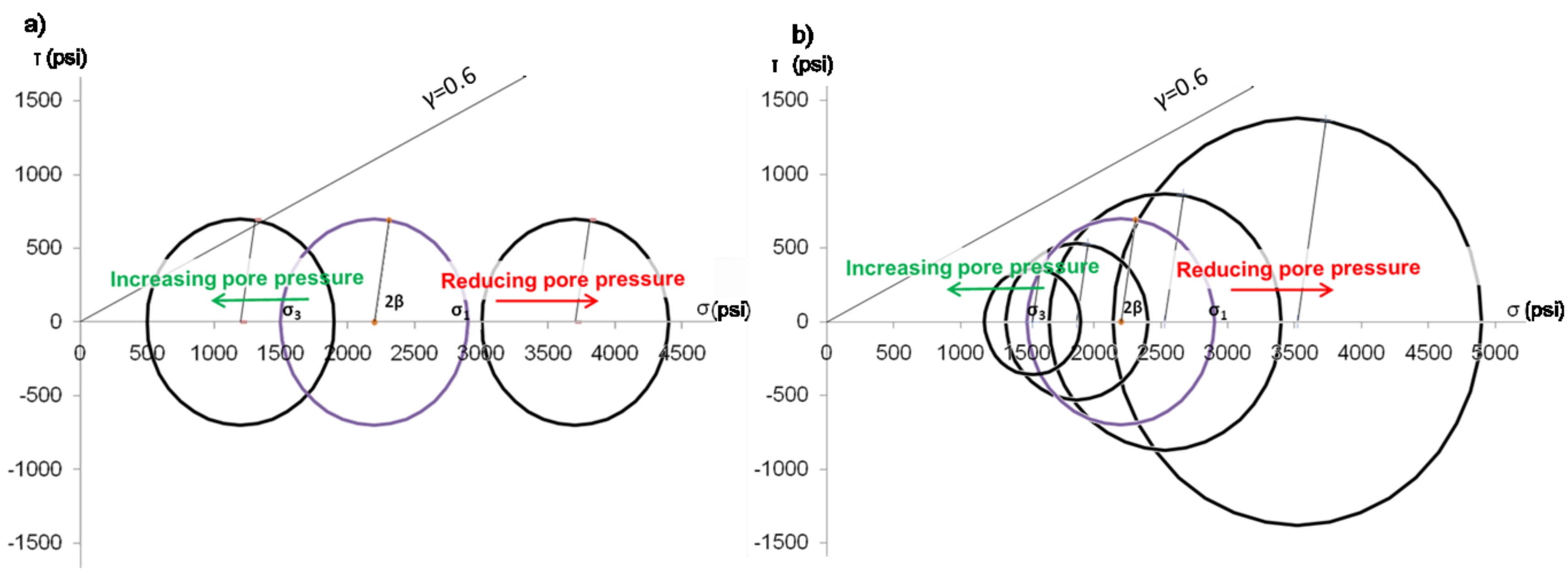

Figure 5.3. The Mohr circles were constructed using current in-situ stresses (purple) and different scenarios of increasing or decreasing pore pressure caused by injection or depletion of the reservoir. In (a) effective stresses are affected uniformly, whereas in (b) principal horizontal stress are affected in such a way that effective minimum horizontal stress changes slowly than effective vertical stress, thus increasing or decreasing the Mohr circles. Note that every scenario does not touch the failure envelope except for the scenario in (a) when pore pressure increases. In Forties field this scenario is highly unlikely, since the reservoir is normally pressured.

Fault interpretation using 3D seismic showed that the dip angles, β, of the faults vary from 15° to 50°. Assuming that a decrease in the coefficient of friction is possible, the smallest change from $\gamma = 0.6$ to $\gamma = 0.3$ occurs when the dip angle of the fault, $\beta = 40^{o}$ - 50^{o} (Figure 5.4). Using coefficient of friction of $\gamma=0.3$, the region of possible fault slip is between $40^{o} \leq \beta \leq 65^{o}$ colored in black in Figure 5.5.

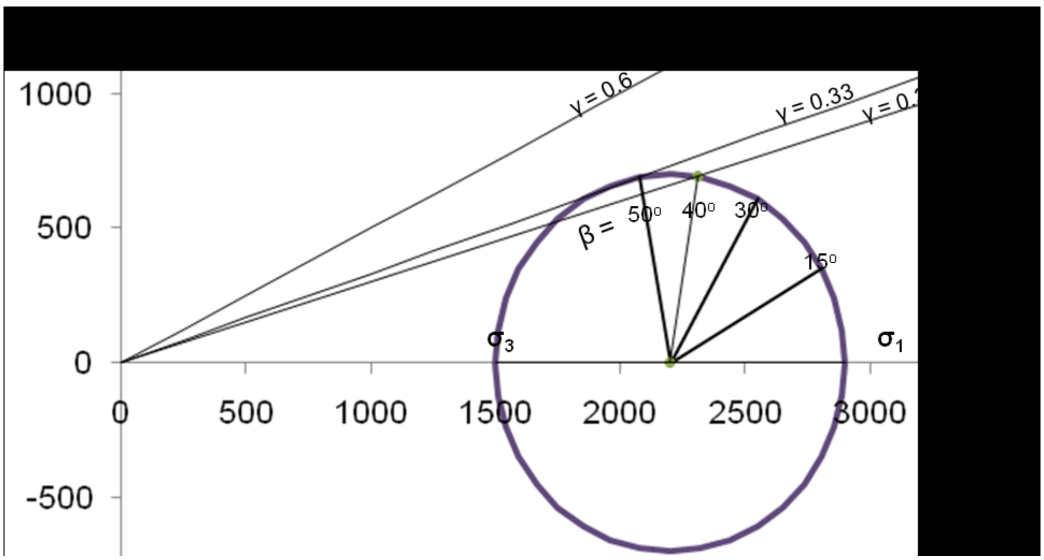

Figure 5.4. Stress state plot with the Mohr circle constructed using in-situ effective stresses representative of Forties field. Note that suggested coefficient of friction by Zoback (2007) and Jaeger and Cook (1979) of $\gamma=0.6$ does not touch the Mohr circle. In order for the region of slip to occur with a fault dip angle of $\beta=40^{o}$ - 50^{o}, the coefficient of friction has to decrease to about $\gamma=0.3$.

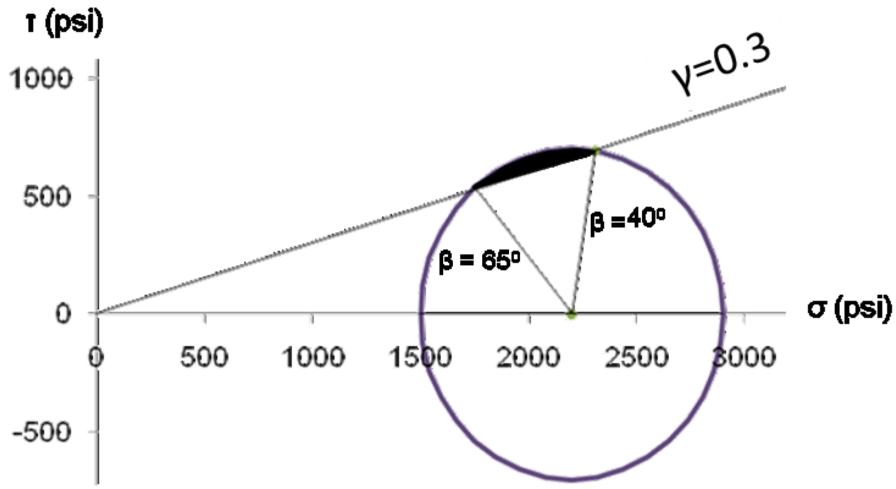

Figure 5.5. Stress state plot with Mohr circle constructed using in-situ effective stresses. Assuming a coefficient of friction of γ=0.3, the region of possible fault slip is between β=40°-65°.

Rock Strength Estimation from Well Logs

From the fault slip analysis, we can see that the region of fault slip failure depends on the coefficient of friction, γ. In the case of the Sele formation shale, the coefficient of friction is very low, two times lower than that suggested by Zoback (2007), which can be ascribed to the lubricant within the fault gouge and low strength of the rock within the fault region. Core studies conducted by Apache Corporation and Schlumberger (Keir et al., 2009) showed pre-existing sub-horizontal fractures and layering within weak shales of the Sele formation (Figure 5.6). The same study showed difference in UCS values (Figure 5.7) measured at angles, 0°, 45 °, and 90° to the bedding plane. It is important to point out that the measured UCS values at 0° and 90° to the bedding plane are not representatives of the strength of the rock mass because they are parallel to the maximum stress direction. Thus, the strength of the rock is not affected at 0° and 90° directions. See Appendix A for explanation.

The competency and weakness of shale is dependant on the sub-horizontal layering and fractures within the rock that affects the stability of the pre-existing faults through the formation and shale stability at the borehole. Apache Corporation reported several wells that had shale instability problems within the Sele formations (Mohamed, 2011). Knowing that the overlying Balder shale formation is more competent and knowing the location of the wells with shale instability problems, we can descriminate between weak, low UCS, and strong, high UCS, rock material. The results from the labaratory measurements are compared with the UCS estimation from well logs discussed in Chapter III. Figure 5.8 shows that the estimation of the UCS values from empirical relationships provided by Lal (1999) and Horsrud (2001) correspond to the values from the core measurements at 45^o angle to bedding. It is important to note that the UCS values from core measurements are static measurements from stress-strain relationship and the estimated UCS from sonic logs are dynamic measurements from elastic wave velocities. Even though both methods are in agreement with each other, the approaches to estimate the UCS are very different from each other.

Both empirical relationships, Lal's (1999) and Horsrud's (2001) show that for the rocks with lower Δt or higher velocities, the UCS increases. Using Lal's (1999) estimation, elastic impedance inversion from surface seismic was used to compare and delineate the lateral variation of the Sele shale formation. Figure 5.9 shows a cross-plot of UCS with μ-ρ calculated using well logs, where the colors represent different wells that have been plotted. The cross-plot shows that μ-ρ is directly related to empirically estimated UCS. The lower values colored in light pink and turqoise within the red oval represent the wells that have reported shale instability within the Sele formation.

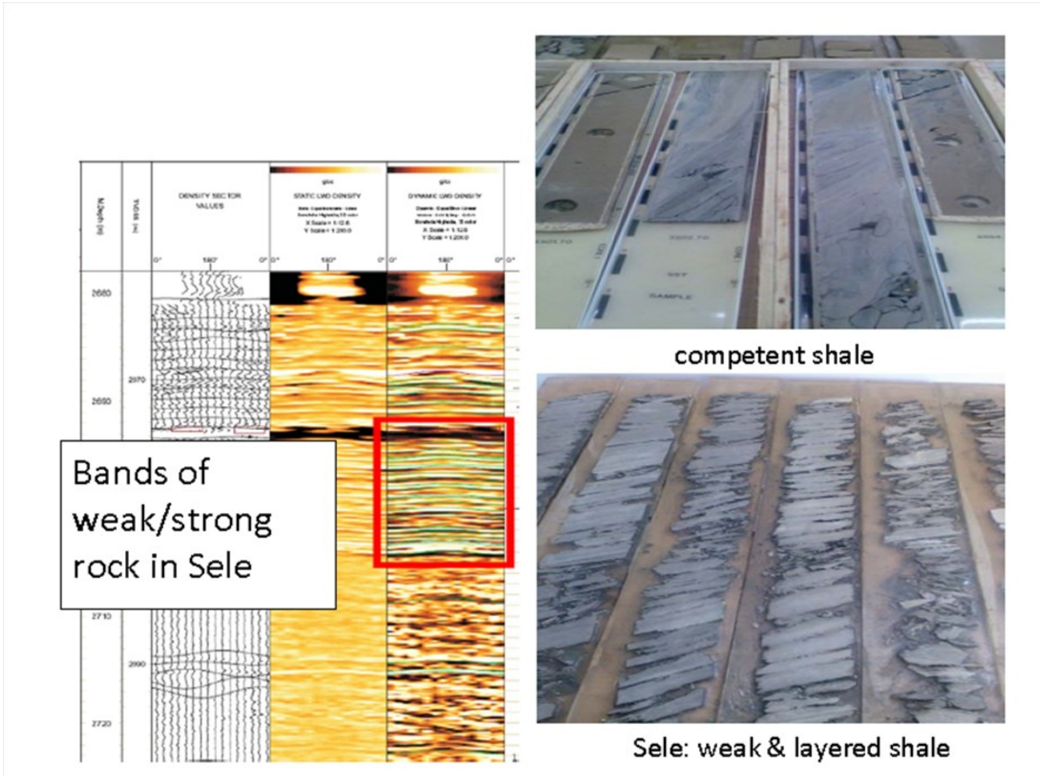

Figure 5.6. LWD density image and pictures of cores within the Sele formation shale showing weak and layered shale that causes anisotropy and low UCS values (After Keir et al., 2009).

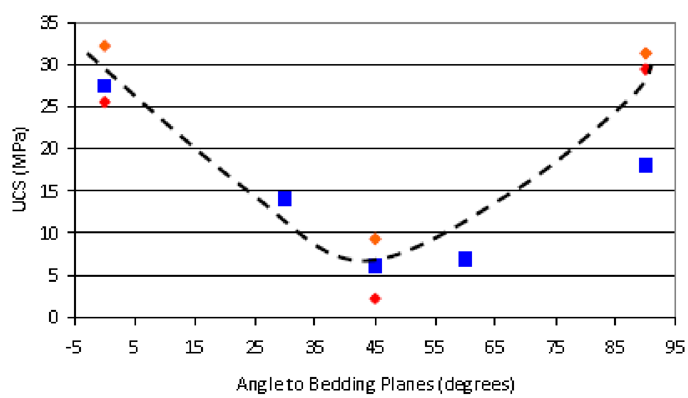

Figure 5.7. UCS measurements from shale cores in the Sele formation, where different colors represent different core samples. Note the changes in UCS values with angle at which measurements were taken, indicating that the rock strength is a minimum at 45^o and strongest at 0^o and 90^o to the bedding (After Keir et al., 2009).

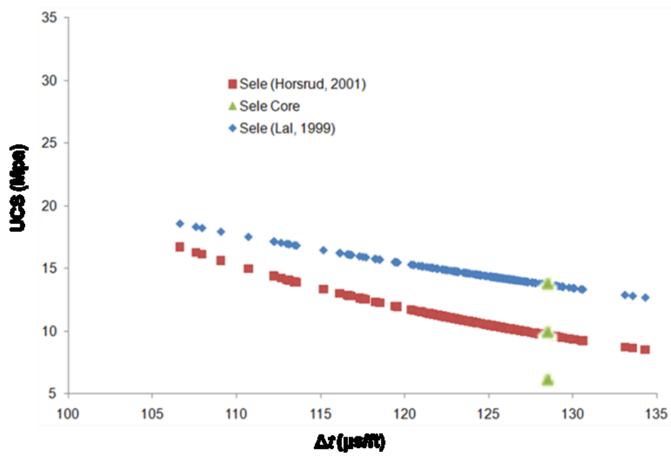

Figure 5.8. UCS versus DT plot showing that UCS measurements from the core at 45^{o} angle to the bedding, plotted as green triangles, correspond to rock strength estimations using empirical relationships by Lal (1999), plotted as blue rombs, and Horsrud (2001), plotted as red rectangles.

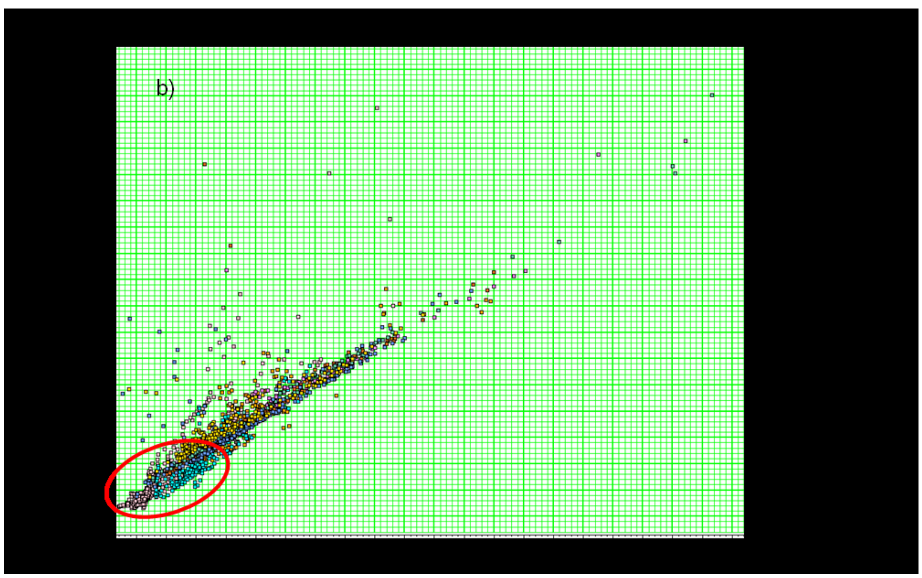

Figure 5.9. Comparative cross-plot of measured μ-ρ values with empirically derived values of UCS from well data using Lal's (1999) empirical relationship. Colors represent different wells, where the lower values colored as light pink and turquoise are the values from the wells that reported shale instability within the Sele formation that fall within the red oval.

CHAPTER VI

ANALYSIS - FORTIES FIELD 3D SEISMIC

Data conditioning and 3D Seismic Interpretation

I applied structure-oriented-filtering (SOF) to angle-limited stacked migrated seismic data, to enhance the signal-to-noise ratio, thereby facilitating subsequent interpretation. Figure 6.1 compares horizon slices along the Sele formation shale top through the Sobel filter attribute volume computed before and after SOF. Notice the reduced noise of the Sobel filter volume calculated from the pre-conditioned seismic (Figure 6.1b) denoted by blue arrows, compared to that calculated from the original volume in Figure 6.1a. Volumetric attributes are computed using a 3D analysis window and are thus statistically more robust than the horizon-based attributes that suffer from picking error. A green arrow indicates a fault in Figure 6.1b that is not easily noticed in Figure 6.1a, which is due to the edge-preserving filter enhancing the reflector discontinuities. Discontinuities of the reflector that are smeared in Figure 6.2a are readily seen in Figure 6.2b after the SOF. 2D horizon autotracking, available in most commercial software, jumps the discontinuities in Figure 6.2c, resulting in a continuous pink reflector. After the SOF, the sharpened faults stop the autotracking, giving rise to the broken reflector denoted by the white arrows (Figure 6.2d).

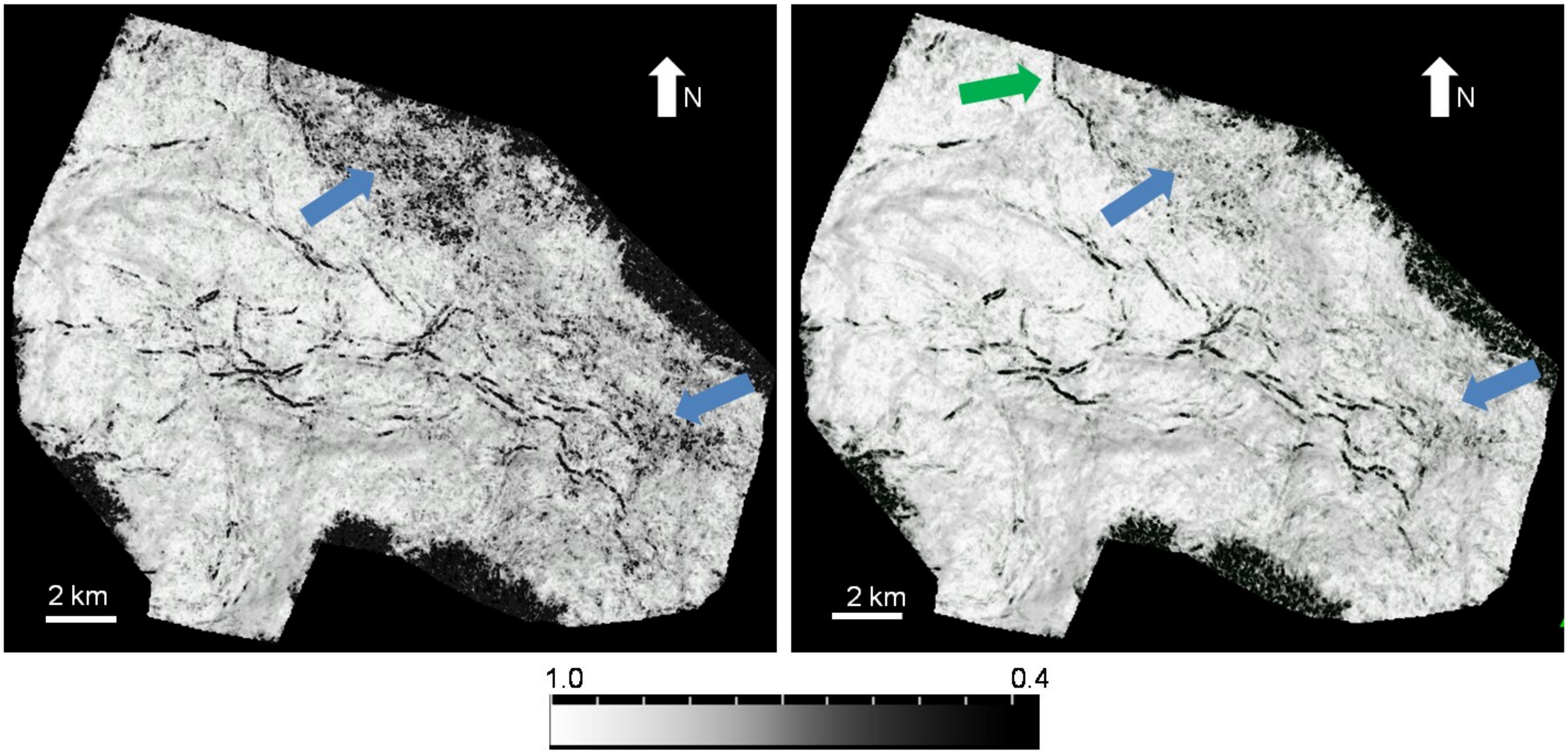

Figure 6.1. Horizon slice along the top Sele formation through the Sobel filter attribute volume computed from (a) the un-conditioned and (b) the pre-conditioned, SOF, seismic amplitude volumes. Notice the noise reduction after conditioning the seismic amplitude volume denoted by blue arrows. The fault shown cutting the horizon through (b) denoted by the green arrow that is hard to see on (a).

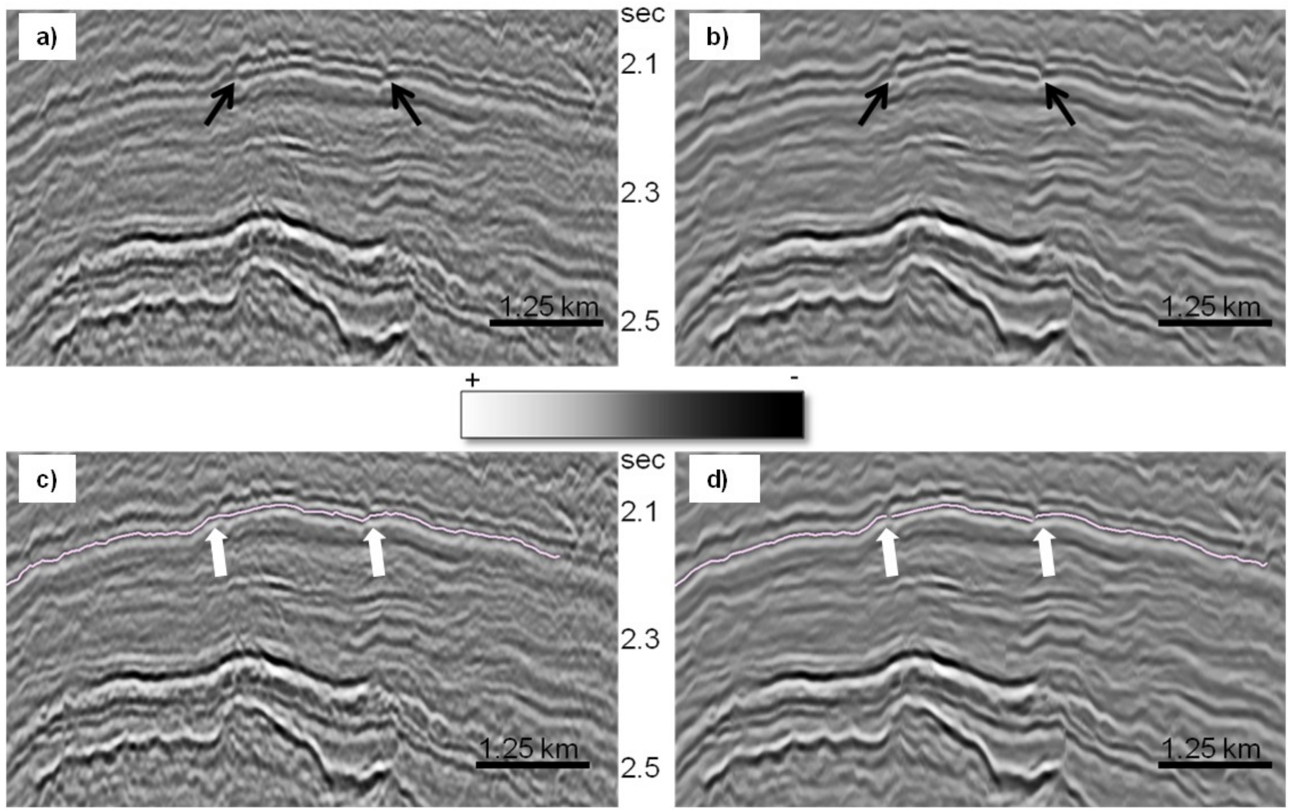

Figure 6.2. Vertical slices through seismic amplitude volumes (a) before and (b) after the SOF. Black arrows indicate faults that are better resolved in (b). Note how 2D horizon autotracking shown in pink, available in commercial software, (c) does not detect the reflector discontinuity thus missing the fault on the un-conditioned seismic, but (d) stops at the fault edge after the SOF denoted by the white arrows.

3D seismic interpretation analysis on conditioned partial angle stacked seismic data includes interpretation of the Paleocene Sele shale formation horizon (Figures 6.3a and b) and the overlying top Balder shale formation (Figure 6.3b). Horizon picks were based on the well tops provided by Apache Corporation. Fault interpretation was based on observed discontinuities in seismic amplitude that was correlated to seismic attributes, including the Sobel filter, coherence, and principal curvatures described later in this chapter. Fault modeling included picking each fault, such that they fit with the surface, and computing fault dip and azimuth. Fault planes were further classified into the groups by dip angles: 15^o-30^o, 30^o-40^o, and $>40^o$ (Figure 6.4).

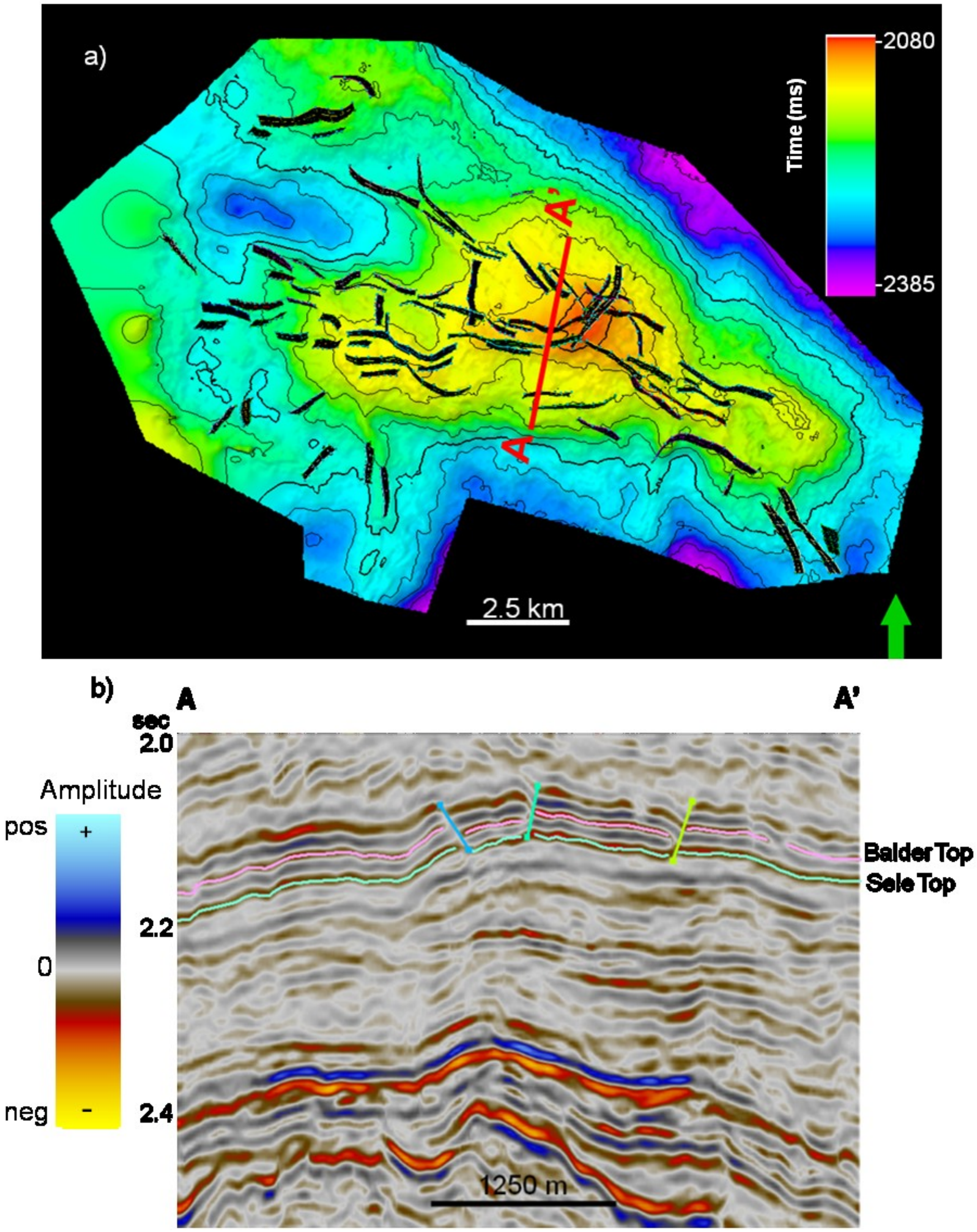

Figure 6.3. Interpreted (a) top Sele shale horizon time structure map with subset of modeled faults. (b) Vertical slice AA' showing top Balder (in pink) and top Sele (in green) horizons and modeled faults.

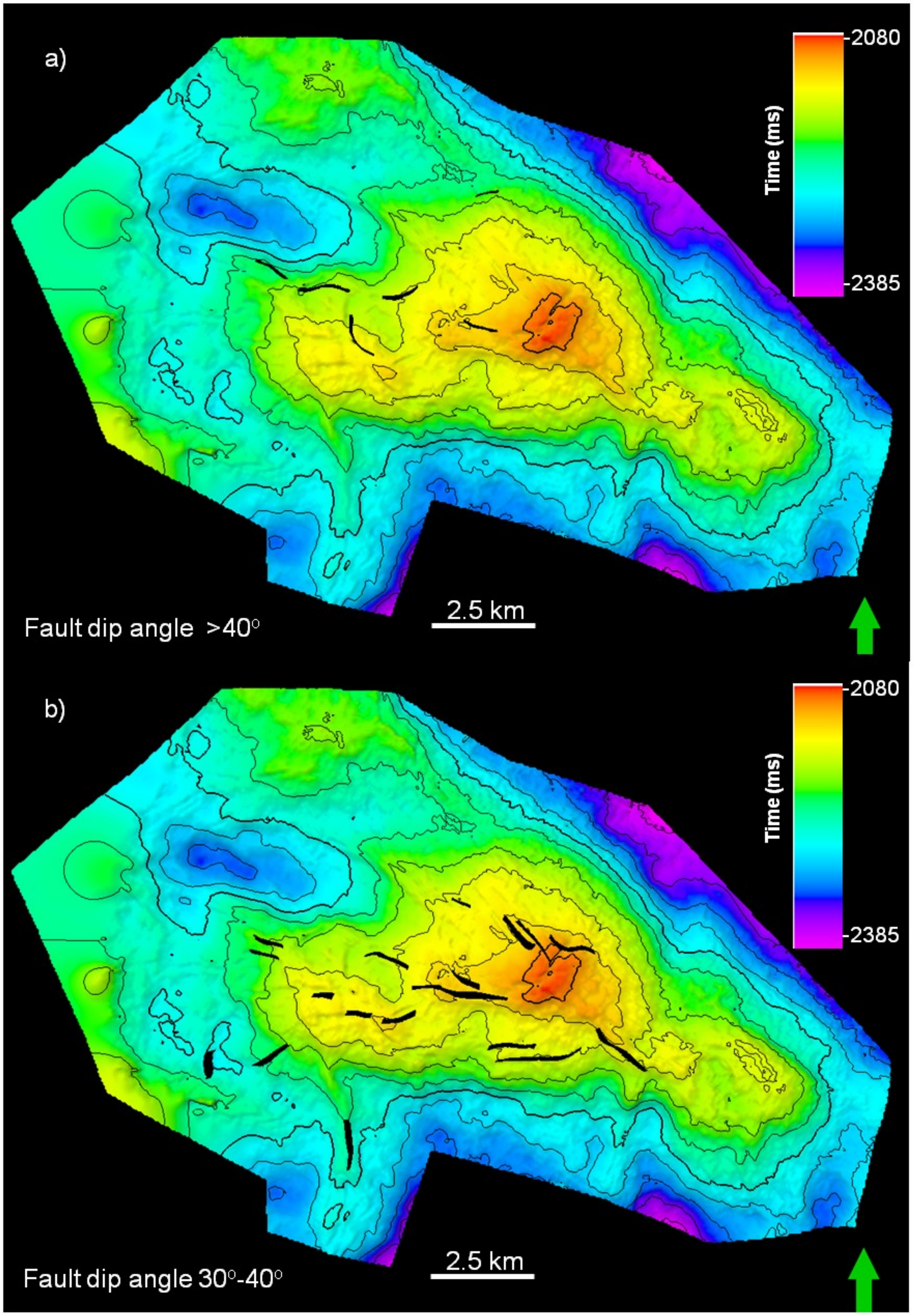
a)
-2080
Time (ms)
-2385
2.5 km
Fault dip angle >40°
b)
-2080
Time (ms)
-2385
2.5 km
Fault dip angle 30°-40°

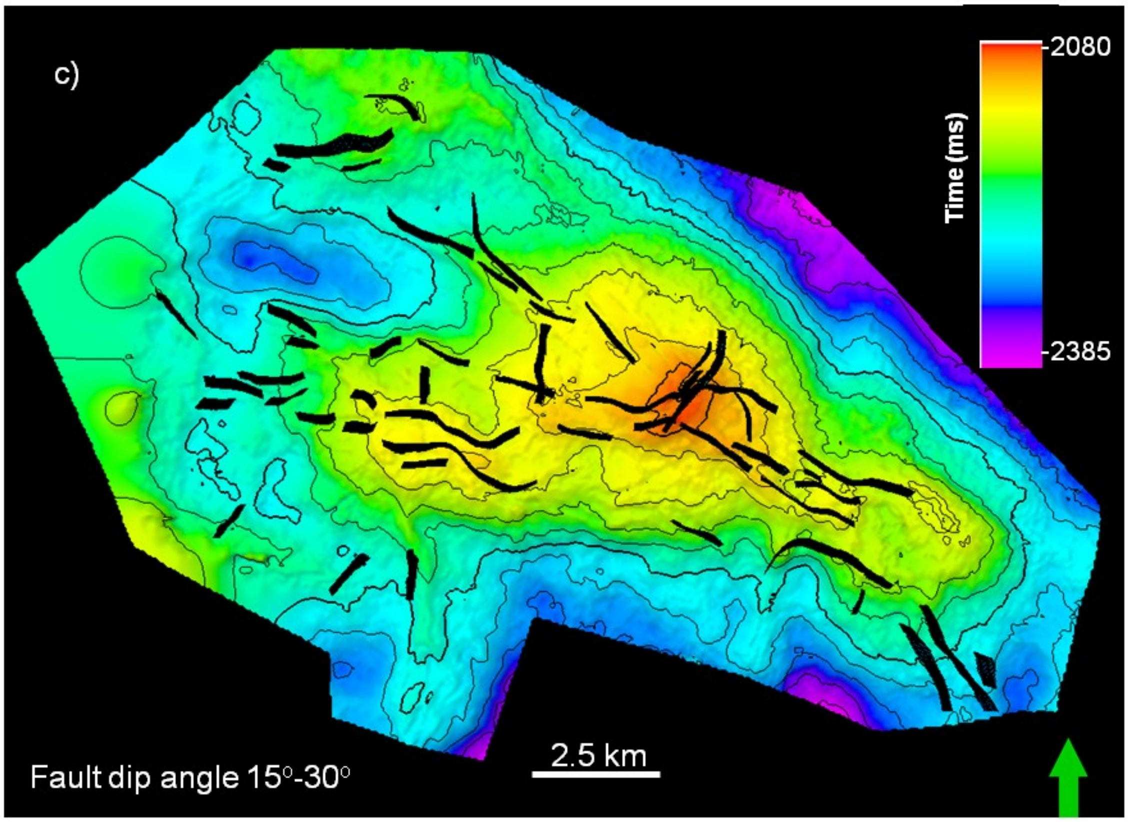

Figure 6.4. Structural map of the Sele formation top with interpreted faults where the dip angles are categorized as (a) >40°, (b) 30°-40°, and (c) 15°-30° from the vertical.

Application of 3D Seismic Attributes

The Sobel filter shows faults better than the eigenstructure-based coherence attribute, which implies that faults represent a lateral change in amplitude rather than in waveform (Chopra and Marfurt, 2007). Figure 6.5 compares horizon slices along the top Sele formation through the Sobel filter and coherence volumes. Blue arrows indicate faults detected by the Sobel filter but not by coherence. In contrast to these two similarity attributes, volumetric curvature attributes are insensitive to amplitude and waveform, but rather detect faults that have drag or have antithetic faults that give rise to what appears to be curvature (Ferrill and Morris, 2008) associated with the faults in the area.

Volumetric principal curvature attributes delineate normal faults within the Balder and Sele shale formations. Ma et al. (2009) analyzed curvature over a survey in Mexico and correlated surface drag associated with the faults to the most-positive, k_1, and most-negative, k_2, principal curvatures. Figure 6.6 shows the top Sele formation surface through most-positive and most-negative principal curvatures (k_1 and k_2), and the corresponding fault drags as black lines. Co-rendering both curvature volumes together, we can see the delineation of the grabens and horsts, shown in Figure 6.7a, where grabens, colored as white lines, correspond to k_2 anomalies surrounded by horsts colored as black lines, correspond to k_1 anomalies (Figure 6.7b). Correlating fault discontinuities using edge-detecting attributes to the principal curvature volumes is necessary because principal curvature also delineates flexure (folding). Co-rendering most-positive and most-negative principal curvatures with edge-detecting attributes helps to visualize the movements of the blocks in relation to fault discontinuities (Figure 6.8a and b). In order to further differentiate structural deformations in terms of their shapes, shape index with curvedness was computed using principal curvatures, k_1 *and* k_2:

$$s = -\frac{2}{\pi}\mathrm{ATAN}\left(\frac{k_2+k_1}{k_2-k_1}\right). \tag{6.1}$$

3D quadratic shapes are described by six basic shapes (Figure 6.9b): bowl, dome, ridge, valley, saddle, and plane. I used a 2D color bar (Figure 6.9c), where the shapes correspond to the colors and are modulated to the curvedness that becomes lighter (more white) as each shape gets closer to becoming planar. The synclines seen in the most-negative principal curvature correspond to the saddle and valley shapes, whereas faults delineated by Sobel filter similarity correspond to ridge and dome shapes as seen in Figure 6.9c.

In order to observe strikes of the faults, I computed the strike of the most-positive principal curvature, k_1, plotted it against the intensity of k_1 using a cyclical 2D color bar, and co-rendered them with the Sobel filter similarity to delineate the fault discontinuities (Figure 6.10). The hue represents the strike of k_1, whereas the lightness of the k_1 varies from 0 (white) to 5 (to a pure color). The azimuth of the strike is calculated from North. The larger faults shown in Figure 6.4 generally strike 120^o from North. The blue arrows denote faults with the azimuth of about 30^o, almost perpendicular to the general direction.

Overall, normal fault strikes have general NW-SE direction, following the same orientation of underlying the Forties-Montrose High and reservoir turbidite current flow, described in the Chapter II.

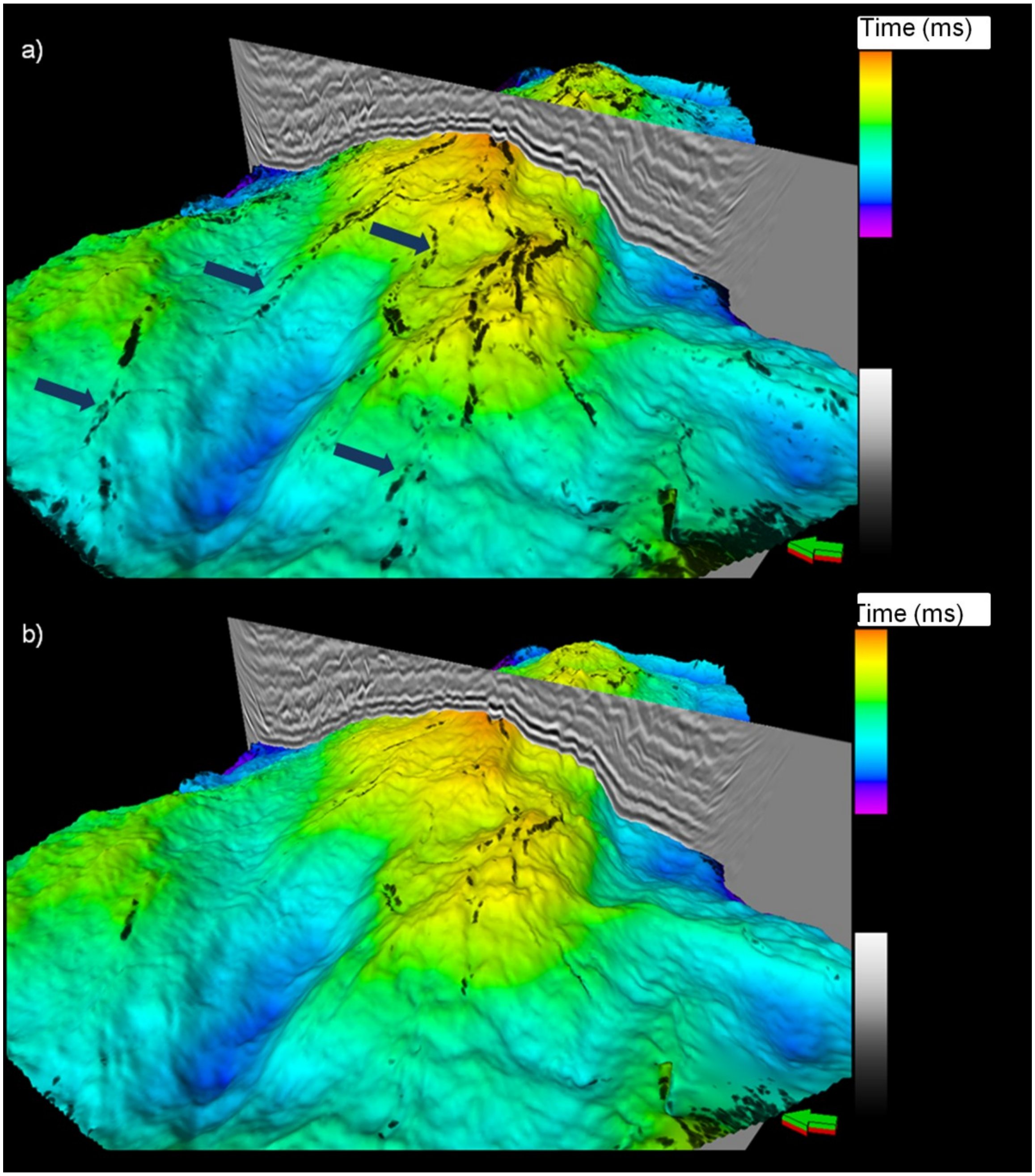

Figure 6.5. Horizon slice along the top Sele formation through (a) Sobel filter and (b) coherence volumes showing faults in black. Note the faults delineated by the Sobel filter attribute, marked by blue arrows, which are not detected by the coherence attribute.

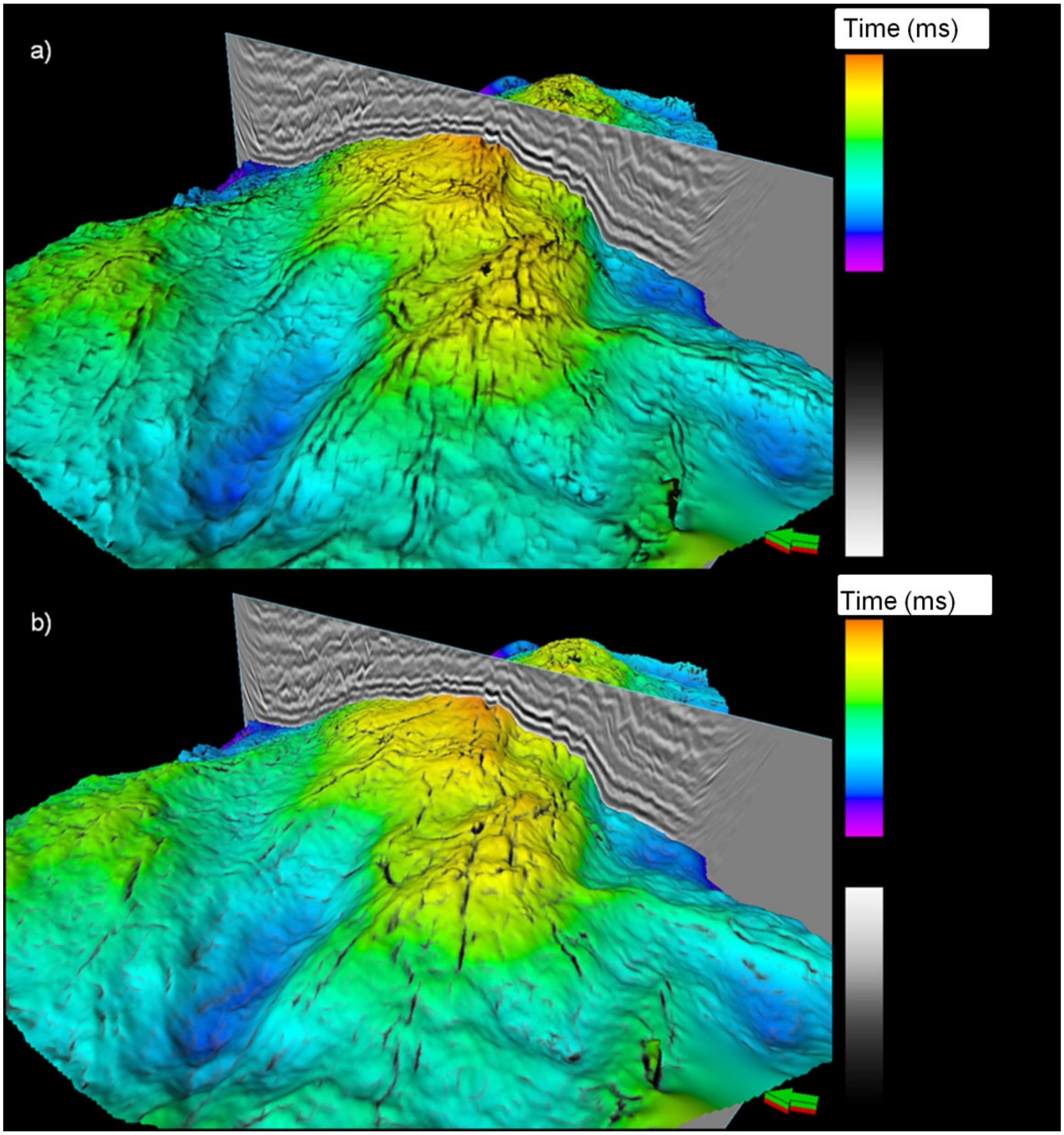

Figure 6.6. Horizon slice along the top Sele formation through (a) most-positive principal curvature, k_1 and (b) most-negative principal curvature, k_2. Note that both principal curvatures delineate the drag associated with the faults as was described by Ma et al. (2009).

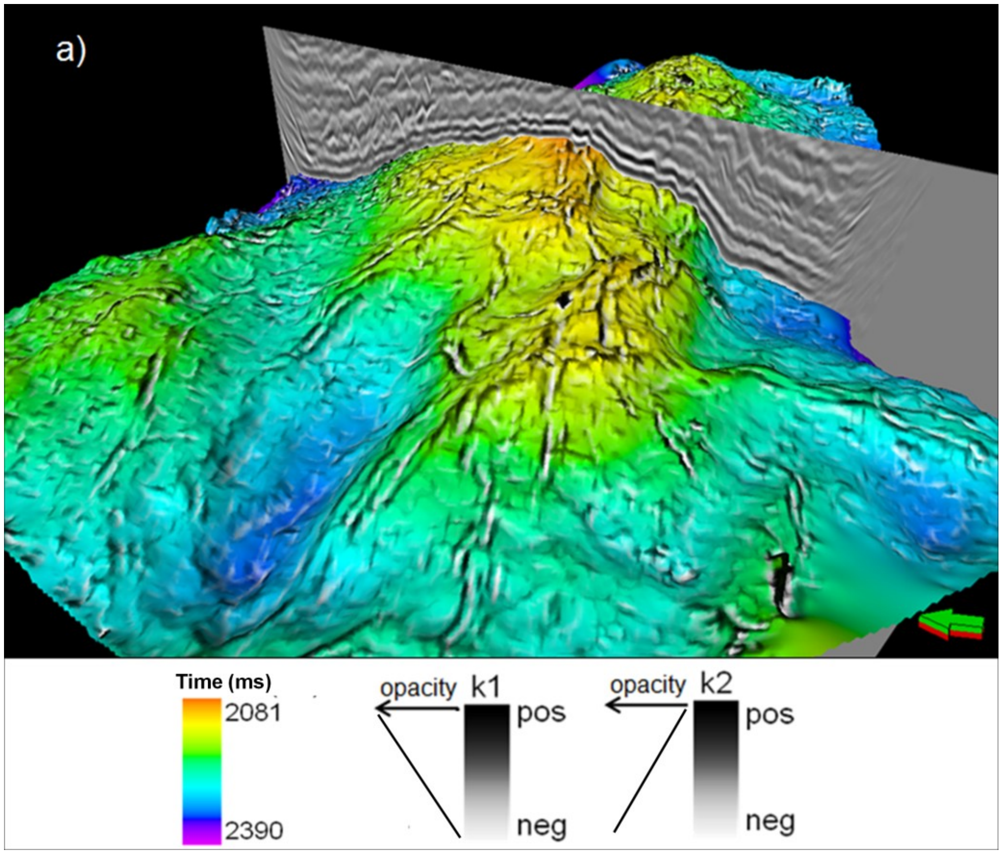

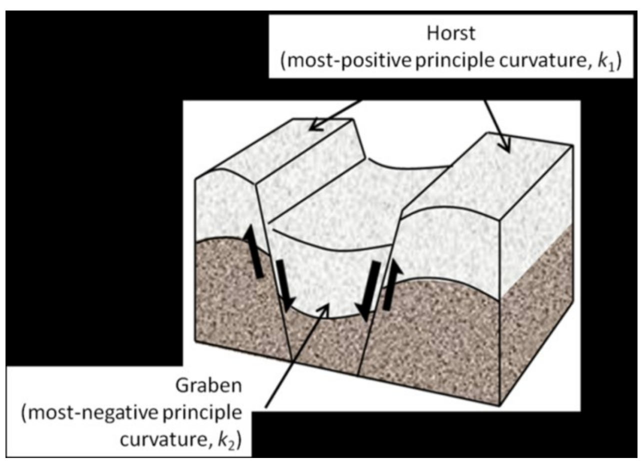

Figure 6.7. (a) Horizon slice along the top Sele formation through co-rendered most-positive and most-negative principal curvature volumes. Notice that the most positive principal curvature shown as black lines corresponds to the horst, and in the middle, grabens, shown in white lines, correspond to most-negative principal curvature. (b) Cartoon depicting the normal faults.

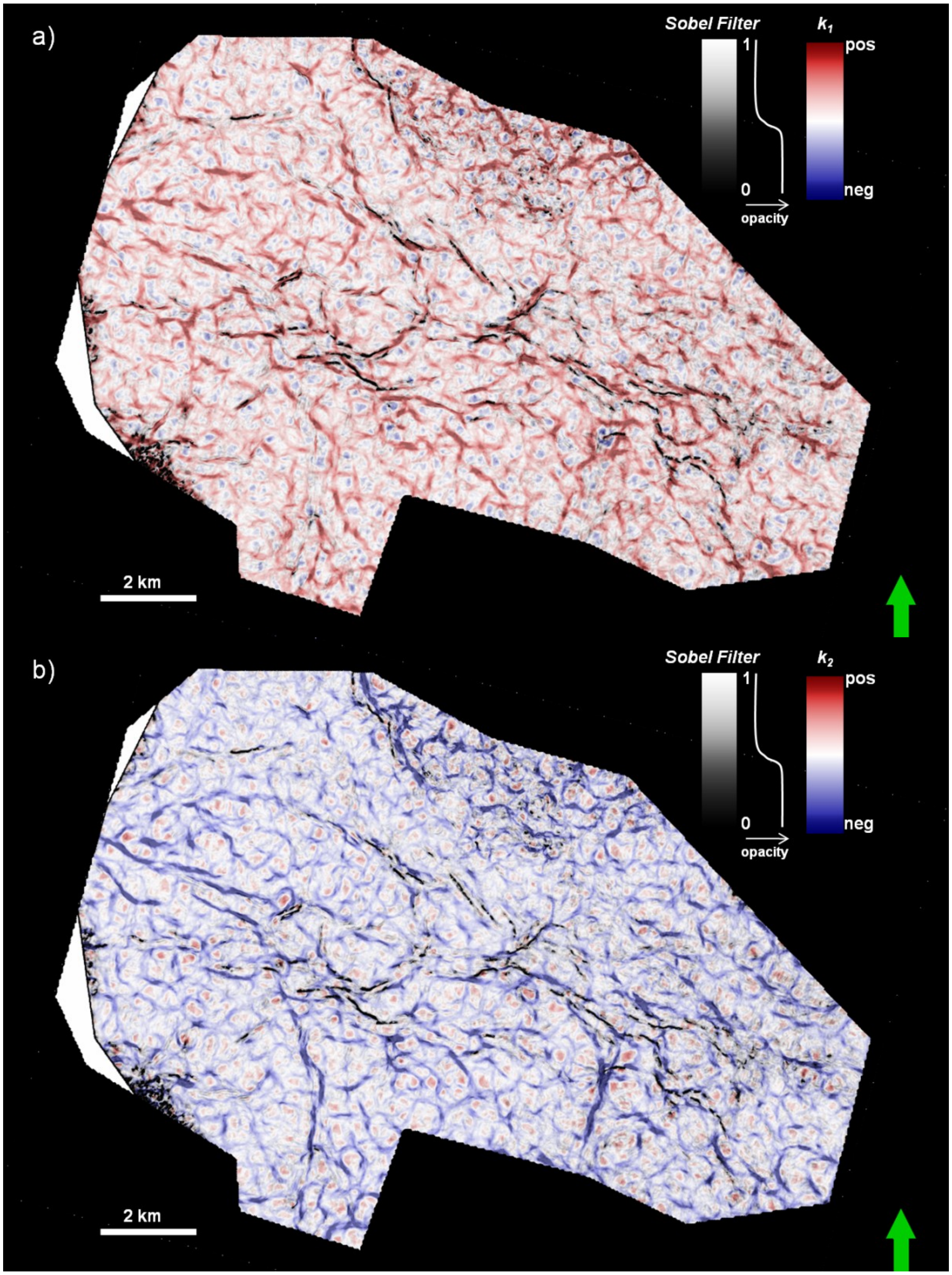

Figure 6.8. Horizon slice along the top Sele formation through (a) co-rendered most-positive principal curvature and Sobel filter and (b) most-negative principal curvature and Sobel filter volumes. Notice that co-rendering edge-detecting attribute with curvature makes it easier to visualize upthrown and downthrown blocks of the fault discontinuity.

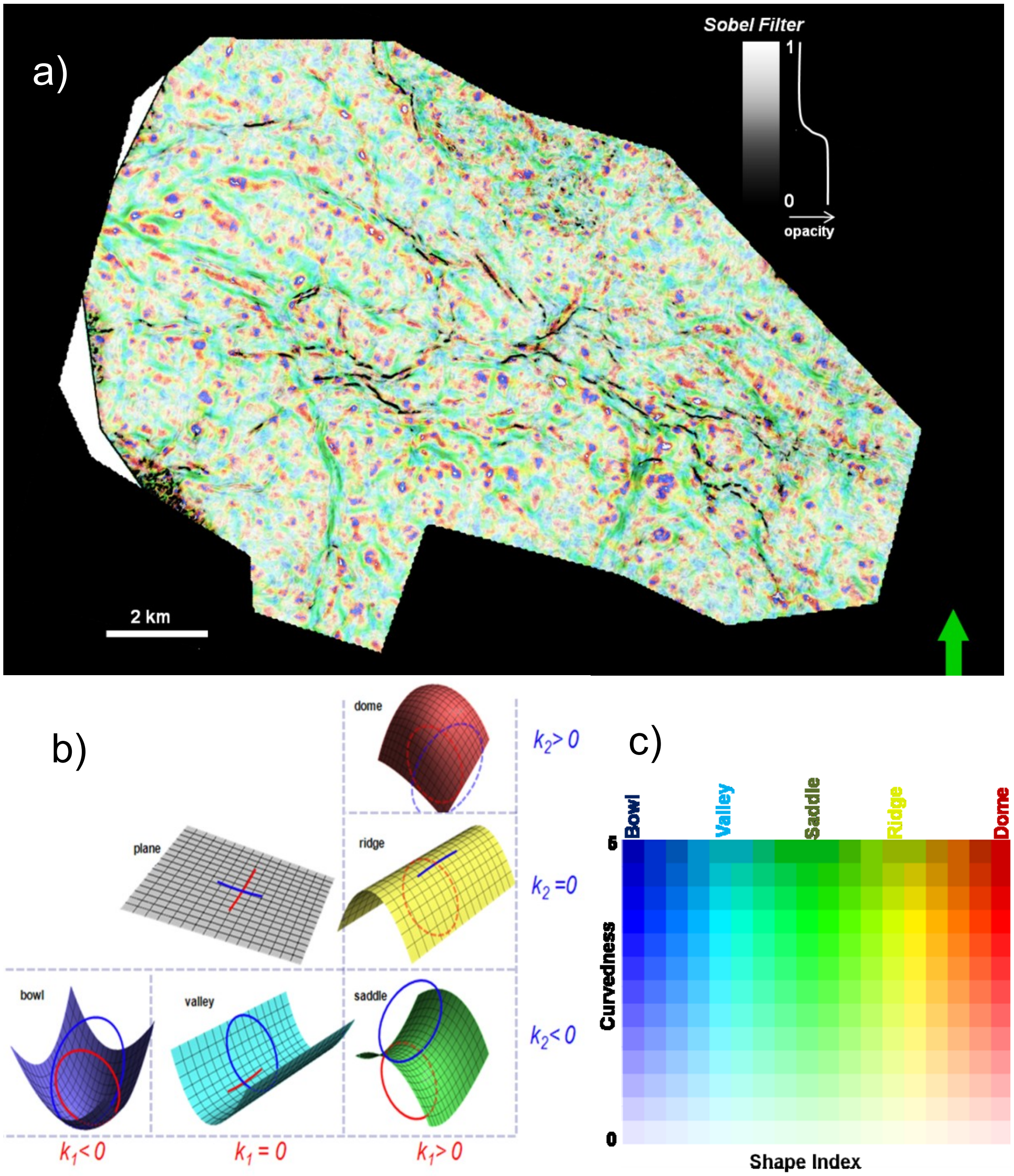

Figure 6.9. (a) Horizon slice along the top Sele formation through co-rendered shape index volume modulate by curvedness with Sobel filter similarity volumes, where (b) the colors represent six basic shapes and (c) vary from light (close to being planar) to bright (more curved).

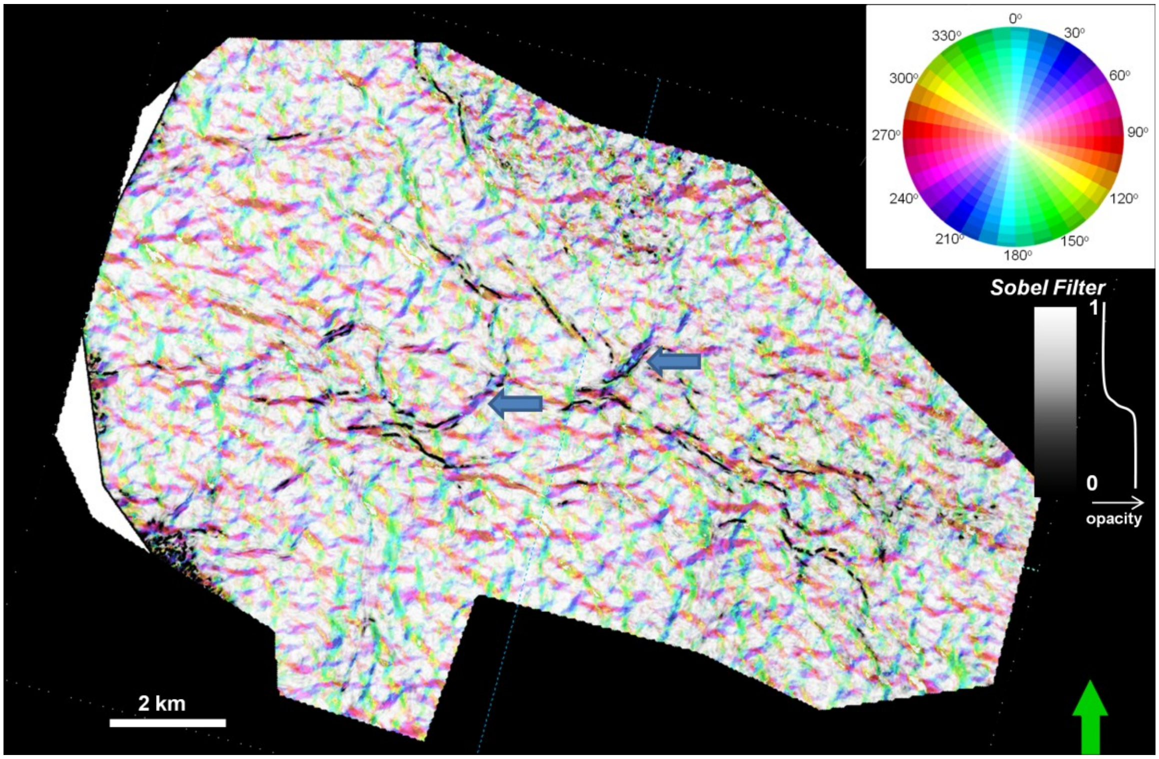

Figure 6.10. Horizon slice along the top Sele formation through k_1 strike modulated by the intensity of k_1 co-rendered with Sobel filter similarity.

Application of Elastic Impedance Inversion

Elastic impedance inversion volume was computed using pre-stack seismic data that resulted in P- and S-impedance volumes. The impedances were then used to calculate λρ and μρ volumes using equations 4.5 and 4.6. Figure 6.11a shows the Sele formation horizon through the μρ volume. The low values ($\mu \leq 7$ GPa*g/cm^3) appear as yellow to red and are interpreted as weak shales, having a correspondingly low UCS values (white arrows). The holes in the data correspond to the locations of the platforms, and the acquisition vessels had to go around them. Figure 6.11b is a zoomed in view, showing wells that report borehole shale instability. These wells correspond to the low UCS and μρ values shown in Figure 5.9. Note that all the wells correspond to the low μρ values computed from the surface seismic data, except one well indicated by purple arrows, which correspond to higher than expected values of μρ. This could be due to the misinterpretation of borehole instability which may have occurred in a shallower formation above the Sele.

The regions with low μρ values are expected to have the weakest shales and in turn have higher risk of borehole instability. Figure 6.11a shows that the weakest shales correspond to the direction of the Paleocene sediment deposition and have a northwesterly trend. Figure 6.12a shows the Sele formation through computed μρ volume with the interpreted faults in the area. Co-rendering faults with dip angles higher than 40^{o} with μρ in Figure 6.12b show that faults within the red oval are located in the low μρ areas would have a low coefficient of friction, and thus may be prone to slip.

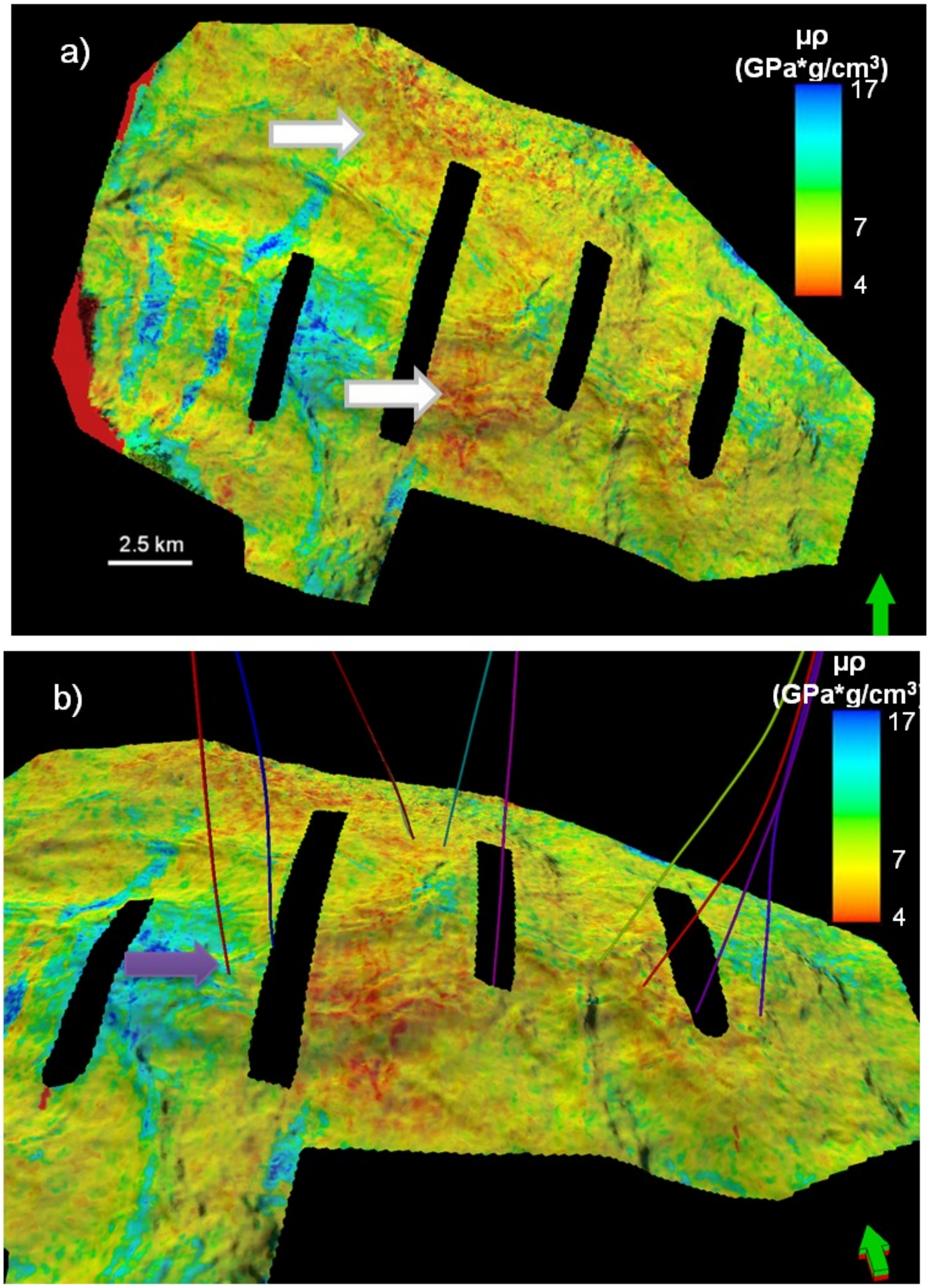

Figure 6.11. The Sele formation horizon through μρ volume computed from pre-stack gathers showing (a) low values of $\mu\rho \leq 7$ GPa*g/cm^3) corresponding to weak shales or low UCS values denoted by white arrows. (b) Zoomed image showing wells that reported shale instability within the Sele. Note the well in (b) indicated by purple arrow that correlate to values $\mu > 7$ GPa*g/cm^3.

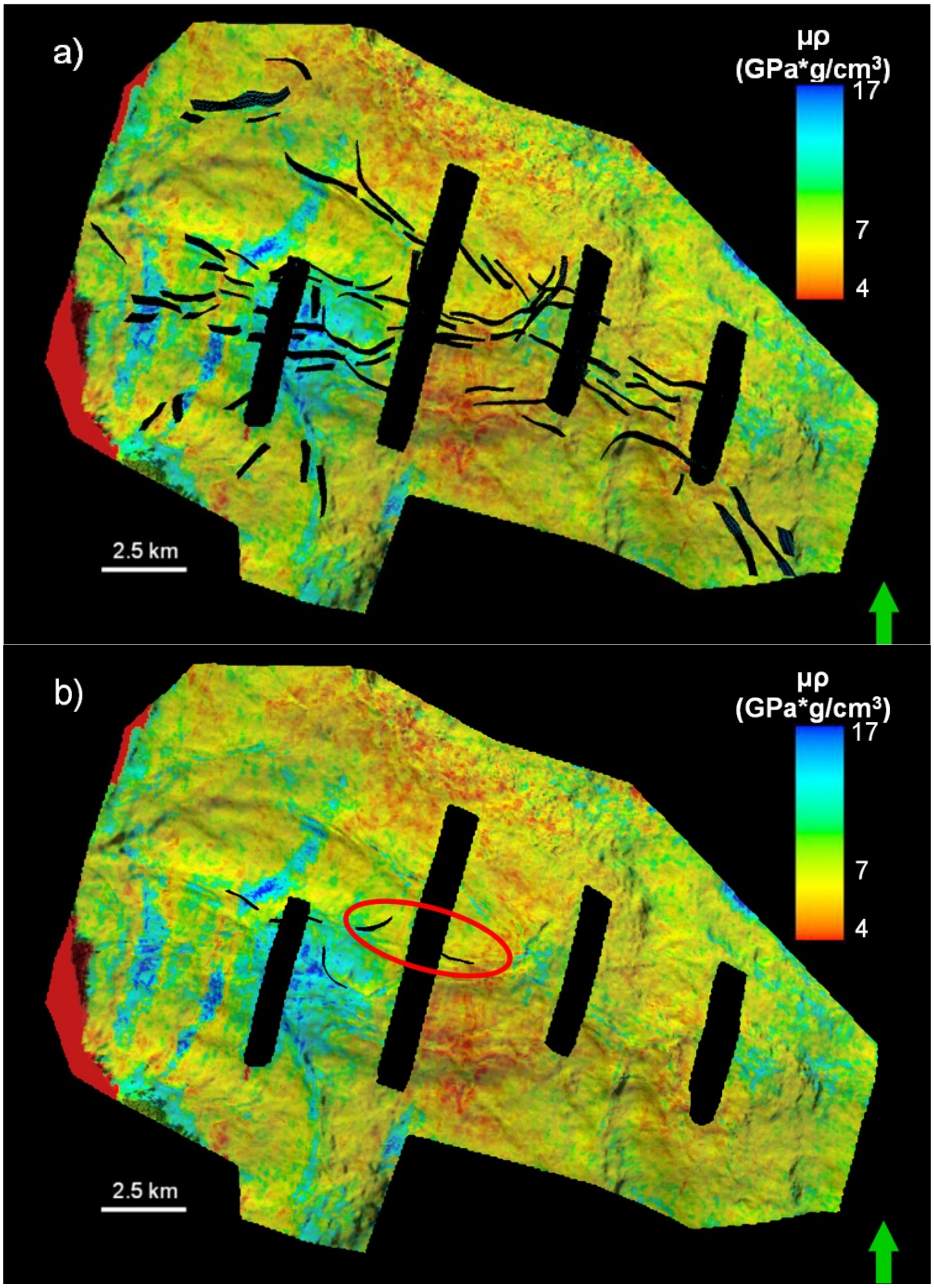

Figure 6.12. (a) The Sele Formation horizon slice through the μρ volume where the low values (colored from bright red to yellow) are more prone to shale instability. (b) Red circle indicates the faults with dip angles higher than 40^{o} within the area of weak rock strength.

DISCUSSION AND CONCLUSIONS

Mohr's circle construction using in-situ stresses showed that fault reactivation is possible for faults with dip angles higher than 40^o and a coefficient of friction of about $\gamma = 0.3$. An interpretation of a decrease in the coefficient of friction from generally accepted $\gamma = 0.6$ is necessary to explain slip along the faults. A decrease in γ could be due to layering and pre-existing fractures (as seen in the core photographs shown in Figure 1.1) within the Sele formation. Apache Corporation reported nine wells that had encountered shale instability (borehole collapse) within the Sele formation. More wells have the same problem. However, it is hard to estimate exactly whether the problem incurred in the caprock, in the reservoir, or in both. I anticipate that "unstable" shales causes a decrease of coefficient of friction, thus faults within these areas of weak shales will reactivate.

This study showed that the uniaxial compressive strength of the shales, UCS, measured from the core samples (static measurements) at 45^o to the bedding explicitly correlates to the dynamic estimation of the UCS values measured from sonic logs (Δt) from deviated wells. The strength of the rock is the weakest at 45^o to the bedding. The study showed that strength of the rock can be correlated to rigidity, μ, of the rock. Well logs from deviated wells were used to empirically estimate UCS values and which can then be crossplotted against $\mu\rho$ values computed from density and dipole sonic logs as well as direct core measurements of strength. The cross-plots showed that a lower bound of $\mu\rho \leq 7$ (GPa)*(g/cm^3) corresponds to weak or "unstable" shales. A direct relationship between UCS and $\mu\rho$ from the wells was then applied and calibrated to $\mu\rho$ values computed from model-based pre-stack impedance inversion of the seismic amplitude data. 3D seismic inversion for calibrated $\mu\rho$ values can be used to estimate the variation of the strength of the shale rock laterally.

Low $\mu\rho$ values, corresponding to weak and "unstable" shales follow a northwesterly trend of the Paleocene sediment deposition. Knowledge of the areas with weak shales can help to construct a more careful well drilling plan with an appropriate mud weight window in order to reduce drilling problems.

After conditioning the seismic amplitude data using structure-oriented filters, I used edge-detecting seismic attributes, including Sobel filter similarity and coherence, and principal curvature attributes help delineate faults in the area. Co-rendering Sobel filter similarity with principal curvatures makes it easier to visualize upthrown and downthrown blocks of the fault discontinuities and better understand the structural geology of the area. The faults in the field have a general NW-SE strike, the trend of deeper faults that controlled the depositional turbidity flow. However, azimuthal strike of the principal curvature showed many NE-SW trending faults and flexures, striking perpendicular to the general trend. Two faults with the dip angles greater than 40^o were mapped in the areas of a low $\mu\rho$ (up to 7 (GPa)*(g/cm3)) that could be prone to slip. None of the faults were drilled through. It is recommended that the drilling and geomechanical engineers use the region of possible slip from Mohr's circle and equation 3.8 for a more careful directional drilling through such faults.

REFERENCES

Ahmadi, Z. M., M. Sawyers., S. Kenyon-Roberts, C. W. Stanworth, K. A. Kugler, J. Kristensen, L. M. G. Ingelli, 2003, Paleocene, The Millennium Atlas: Petroleum Geology of the Central and Northern North Sea: Geological Society, London, 235-259.

Aki, K., and P. G. Richards, 1980, Quantitative Seismology: Theory and Methods, 1: W. H. Freeman and Co.

Al-Dossary, S., and K. J. Marfurt, 2006, 3D volumetric multispectral estimates of reflector curvature and rotation: Geophysics, **71**, 41–51

Bujak, J. and D. Mudge, 1994, A high-resolution North Sea Eocene dinocyst zonation: Journal of Geological Society, **151**, 449-462. http://www.nhm.uio.no/norlex/atlas/7_NORLEX_Paleogene_2.pdf

Carman, G.J., and R. Young, 1982, Reservoir geology of the Forties oilfield, in Illing, L.V., and Hobson, G.D., eds., Petroleum Geology of North-West Europe: Heyden & Son Ltd, 371-379.

Chang, C., M. D. Zoback, and A. Khaksar, 2006 Empirical relations between rock strength and physical properties in sedimentary rocks: Journal of Petroleum Science and Engineering, **51**, 223-237.

Chopra, S., and K. J. Marfurt, 2007, Volumetric curvature attributes add value to 3D seismic data interpretation: The Leading Edge, **26**, 856-867.

Chopra, S. and K. J. Marfurt, 2010, Integration of coherence and volumetric curvature images: The Leading Edge, **29**, 1092-1107.

Darby D., R. S. Haszeldine, and G. D. Couples, 1996, Pressure cells and pressure seals in the UK Central Graben: Marine and Petroleum Geology, **13**, 865-878.

Davis, G.H., and S.J. Reynolds, 1996, Structural geology of rocks and regions (2nd Edition): John Wiley and Sons.

Davogustto, O., 2011, Removing footprint from legacy seismic data volumes, M.S. Thesis, Norman, Oklahoma.

Dewhurst, D., J. Cartwright, and L. Lonergan, 1999, The development of polygonal fault systems by syneresis of colloidal sediments: Marine and Petroleum Geology, **16**, 793-810.

Ferrill, D. A., and A. P. Morris, 2008, Fault zone deformation controlled by carbonate mechanical stratigraphy, Balcones fault system, Texas: AAPG Bulletin, **92**, 359–380.

Frederiksen, S., S. B. Nielsen, and N. Balling, 2001, Post-Permian evolution of the Central North Sea: a numerical model: Tectonophysics, **343**, 185-203.

Goodway, B., T. Chen, and J. Downton, 1997, Improved AVO fluid detection and lithology discrimination using Lamé petrophysical parameters; "λρ", "μρ", & "λ/μ fluid stack", from P and S inversions: 67th Annual International Meeting, SEG, Expanded Abstracts, 183-186.

Hampson, D. P., B. H. Russel, and B. Bankhead, 2005, Simultaneous inversion of pre-stack seismic data: 75th Annual International Meeting, SEG, Expanded Abstracts, 1063-1067.

Hampson, B. and D. Russel, 2006, The old and the new in seismic inversion: CSEG Recorder, 5-11.

Hempton, M., J. Marshall, S. Sadler, N. Hogg, R. Charles, and C. Harvey, 2005, Turbidite reservoirs of the Sele Formation, Central North Sea - geological challenges for improving production, in Dore, A.G. and Vining, B.A., eds., Petroleum Geology: North-West Europe and Global Perspectives, Proceedings of the 6th Petroleum Geology Conference: Geological Society of London.

Hibsch, C., J. Jarrige, E. M. Cushing, and J. Mercier, 1995, Palaeostress analysis, a contribution to the understanding of basin tectonics and geodynamic evolution. Example of the Permian/Cenozoic tectonics of Great Britain and geodynamic implications in western Europe: Tectonophysics, **252**, 103-136.

Hill, P.J., and Wood, G.V, 1980, Geology of the Forties Field, U.K. Continental Shelf, North Sea, in Halbouty, M.T., ed., Giant Oil and Gas Fields of the Decade 1968-1978: AAPG Memoir, **30**, 81-93.

Hillis, R. R., 2001, Coupled changes in pore pressure and stress in oil fields and sedimentary basins: Petroleum Geoscience, **7**, 419-425.

Holm, G.M., 1998, Distribution and origin of overpressure in the Central Graben of the North Sea, in Law, B.E., G.F. Ulmishek, and V.I. Slavin eds., Abnormal pressures in hydrocarbon environments: AAPG Memoir **70**, 123–144.

Horsrud, P., 2001, Estimating mechanical properties of shale from empirical correlations: SPE Drilling and Completion, **16**, 68-73.

Jaeger, J. C. and N. G. W. Cook, 1979, Fundamentals of rock mechanics, 2nd edn: Chapman and Hall.

Keir, D., A. Donald, A. Paxton, and E. Knight, 2009, Characterizing sonic anisotropy for geomechanics and geophysics applications: case study in Foties Field, UK: DEVEX Conference.

Lal, M., 1999, Shale stability: drilling fluid interaction and shale strength: SPE Asia Pacific Oil and Gas Conference and Exhibition, Jakarta, Indonesia.

Latin, D. and F. G. Waters, 1992, Basaltic magmatism in the North Sea and its relationship to lithospheric extension: Tectonophysics, **208**, 77-90.

Lin, W., K. Yamamoto, H. Ito, H. Masago, and Y. Kawamura, 2008, Estimation of minimum principal stress from an extended leak-off test onboard the Chikyu drilling vessel and suggestions for future test procedures: Scientific Drilling, 6, 43-47.

Lonergam, L., J. Cartwright, and R. Jolly, 1998, The geometry of polygonal fault systems in Tertiary mudrocks of the North Sea: Journal of Structural Geology, **20**, 529-548.

Lorwongngam, A., 2008, The validity of leak-off test for in situ stress estimation ; the effect of the bottom of the borehole, M. S. Thesis, Norman, Oklahoma.

Luo, Y., W. G. Higgs, and W. S. Kowalik, 1996, Edge detection and stratigraphic analysis using 3D seismic data: 66th Annual International Meeting, Society of Exploration Geophysicists, Expanded Abstracts, 324–327.

Mai, H. T., K. J. Marfurt, and S. Chávez-Pérez, 2009, Coherence and volumetric curvatures and their spatial relationship to faults and folds, an example from Chicontepec basin, Mexico: 79th Annual International Meeting, SEG, Expanded Abstracts, 1063-1067.

McInally, A. T., T. Redondo-López, J. Garnham, J. Kunka, A. D. Brooks, L. Stenstrup Hansen, F. Barclay, and D. Davies, 2003, Optimizing 4D fluid imaging: Petroleum Geoscience, **9**, 91-101.

McIntyre, B., T. Hibbert, D. Keir, R. Dixon, T. ORourke, F. Mohammed, A. Donald, L. Chang, A. Syed, and V. Biran, 2010, Managing drilling risk in a mature North Sea Field: The Journal of Petroleum Technology, **62**, 76-80.

Mohamed, F., 2011, Personal communication.

Nielsen, L., N. Balling, B. H. Jacobsen, and MONA LISA working Group, 2000, Seismic and gravity modelling of crustal structure in the Central Graben, North Sea. Observations along MONA LISA profile 3: Tectonophysics, **328**, 3-4.

Ribeiro, C. C. Reiser, P. Doyen, A. Lau, and S. Adiletta, 2007, Time-lapse simulator-to-seismic study - Forties field, North Sea: 77th Annual International Meeting, SEG, Expanded Abstracts, 2944-2948.

Roegiers, J., 2011, Personal communication.

Roberts, A., 2001, Curvature attributes and their applications to 3D interpreted horizons: First Break, **19**, 85-100.

Sigismondi, M. E. and J. C. Soldo, 2003, Curvature attributes and seismic interpretation: Case studies from Argentina basins: The Leading Edge, **22**, 1122-1126.

Sippel, J., M. Scheck-Wenderoth, K. Reicherter, and S. Mazur, 2009, Paleostress states at the south-western margin of the Central European Basin System — Application of fault-slip analysis to unravel a polyphase deformation pattern: Tectonophysics, **470**, 129-146.

Smith, K. and J. D. Ritchie, 1993, Jurassic volcanic centres in the Central North Sea: Petroleum Geology Conference series, **4**, 519-531.

Spann, H., B. Müller, and K. Fuchs, 1994, Interpretation of anomalies in observed stress data at the Central Graben (North Sea) – Numerical and analytical approach: Soil Dynamics and Earthquake Engineering, **13**, 1-11.

Walmsley, P.J., 1975, The Forties Field, in Woodland, A.W., ed., Petroleum and the Continental Shelf of North-West Europe: Applied Science Publishers Ltd.

White I., D. Kash, M. Chartock, M. Devine, and R. Leonard, 1974, North Sea Oil and Gas: Implications for Future United States Development: University of Oklahoma Press.

Wills, J.M. and D.K. Peattie, 1990, The Forties Field and the evolution of a reservoir management strategy, in North Sea Oil and Gas Reservoir - II: The Norwegian Institute of Technology: Graham and Trotman.

Ziegler, 1992, North Sea rift system: Tectonophysics, **208**, 55-75.

Zoback, M., 2007, Reservoir geomechanics: Cambridge University Press.

Zoback, M. D, and J. H. Healy, 1992, In-situ stress measurements to 3.5 km depth in the Cajon Pass scientific borehole: implications for the mechanics of crustal faulting: Journal of Geophysical Research, **97**, 5039–5057.

APPENDIX A

A fault weakness depends on frictional strength, such that when the ratio of shear to effective normal stress on the fault exceeds frictional strength fault slippage occurs causing reactivation of the discontinuity shown in equation A1 (Zoback, 2007):

$$\frac{\sigma_1}{\sigma_3} = \frac{S_1 - P_p}{S_3 - P_p} \le \left[\left(\gamma^2 + 1 \right)^{1/2} + \gamma \right]^2 \tag{A1}$$

To analyze the strength of the fault, Roegiers (2011) considers shear and effective normal stresses from equations 3.3 and 3.4 and substitutes those expressions in equation 3.6 to obtain following:

$$(\sigma_1 - \sigma_3)\sin 2\beta = 2C_0 + \left[(\sigma_1 + \sigma_3) + 0.5(\sigma_1 - \sigma_3)\cos 2\beta \right] \tan\phi \tag{A2}$$

which simplifies to:

$$(\sigma_1 - \sigma_3) = \frac{2C_0 + (\sigma_1 + \sigma_3)\tan\phi}{\sin 2\beta \, (1 - \cot 2\beta \tan\phi)} \tag{A3}$$

From the Mohr failure envelope, it was determined that the coefficient of internal friction, γ, is defined as

$$\gamma = \tan\phi \tag{A4}$$

which further Jaeger et al. (2007) simplifies equation to:

$$(\sigma_1 - \sigma_3) = \frac{2(C_0 + \gamma\sigma_3)}{(1 - \gamma\cot\beta)\sin 2\beta} \tag{A5}$$

Equation A5 shows the difference between stresses needed for the slippage along the plane of weakness to occur as a function of β with a fixed minimum principal stress σ_3. If the plane of weakness is aligned with the major principal stress σ1, such that $\beta \rightarrow 0$ or $\beta \rightarrow \pi/2$, then the difference between stresses becomes infinite, $\sigma_1 - \sigma_3 \rightarrow \infty$. The slippage also becomes impossible as β → φ which in turn cause cot2βtan φ → 1 in equation A3. So, the region for the slippage to be possible is constrained by φ < β < π/2 and the minimum value of $\sigma_1 - \sigma_3$ for the slippage to occur when:

$$\tan 2\beta = -1/\gamma \qquad \text{(A6)}$$

Using this equation A5, Jaeger et al. (2007) defines minimum σ_1 as:

$$\sigma_1 = \sigma_3 + 2(C_0 + \gamma\sigma_3)\left[(1+\gamma^2)^{1/2} + \gamma\right] \qquad \text{(A7)}$$

or

$$(\sigma_1 - \sigma_3)_{min} = 2(C_0 + \gamma\sigma_3)\left[(1+\gamma^2)^{1/2} + \gamma\right] \qquad \text{(A8)}$$

If the actual (σ_1-σ_3) is larger than $(\sigma_1-\sigma_3)_{min}$ then a possible region of slip exists for pre-existing plane of weakness with β** dip angle shown in Figure A.1, where the slip is impossible for β → φ and β → π/2. So, if the planes of weakness are parallel to the maximum stress direction, these planes do not affect strength of the rock (Roegiers, 2011). So the corresponding angles, β_1 and β_2, between which fault slip can occur, can be found by using following relationship:

$$\beta_{1,2} = \frac{\pi}{2} - \frac{1}{2}\arccos\left[\frac{\gamma}{(1+\gamma^2)^{1/2}}\right] \pm \frac{1}{2}\arccos\left[\frac{\gamma}{(1+\gamma^2)^{1/2}}\frac{\sigma_1+\sigma_3}{\sigma_1-\sigma_3}\right] \qquad \text{(A9)}$$

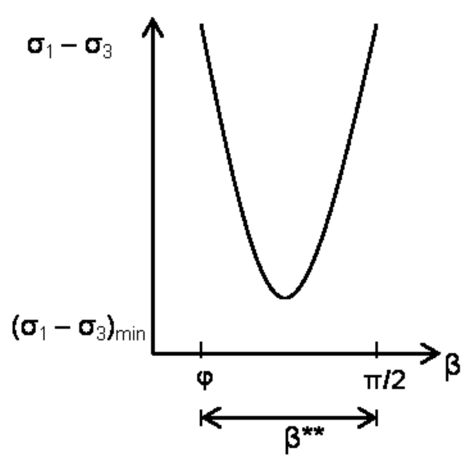

Figure A.1. Influence of weakness planes, where a possible region of slip exists within a range of dip angles β^{**}, when $(\sigma_1-\sigma_3)$ is larger than $(\sigma_1-\sigma_3)_{min.}$ The slip is impossible for $\beta \rightarrow \varphi$ and $\beta \rightarrow \pi/2$ (After Roegiers, 2011).

APPENDIX B

For the inversion analysis, I used model-based pre-stack inversion workflow discussed by Hampson et al. (2005). First, I added +180^{o} phase shift to NMO corrected CMP gathers in order to convert the data to normal polarity, shown in Figure B.1 (blue arrows indicate the corresponding Sele formation horizon). After converting CMP offset gather to angle gather, I applied trim statics to correct for residual moveout. Notice the difference of the events within the blue boxes from before and after statics applied in Figure B.2. Further, I extracted two wavelets from seismic data for angle ranges of 0-15^{o} and 15^{o}-42^{o} shown in Figure B.3.

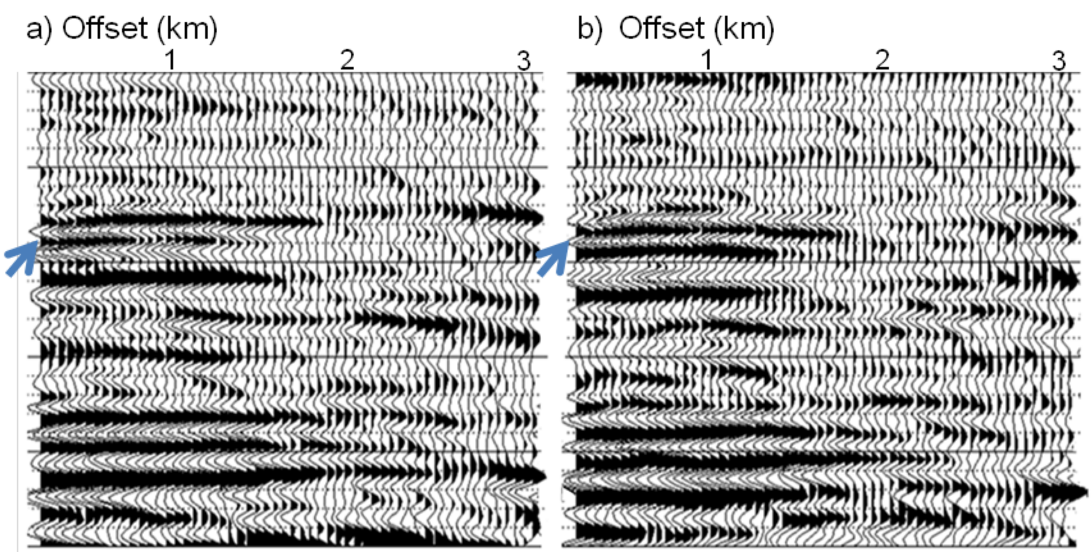

Figure B.1. (a) Original NMO corrected CMP gather with reverse polarity and (b) CMP gather with phase shift of +180^{o} in order to convert to normal polarity. The blue arrows correspond to the Sele formation horizon top.

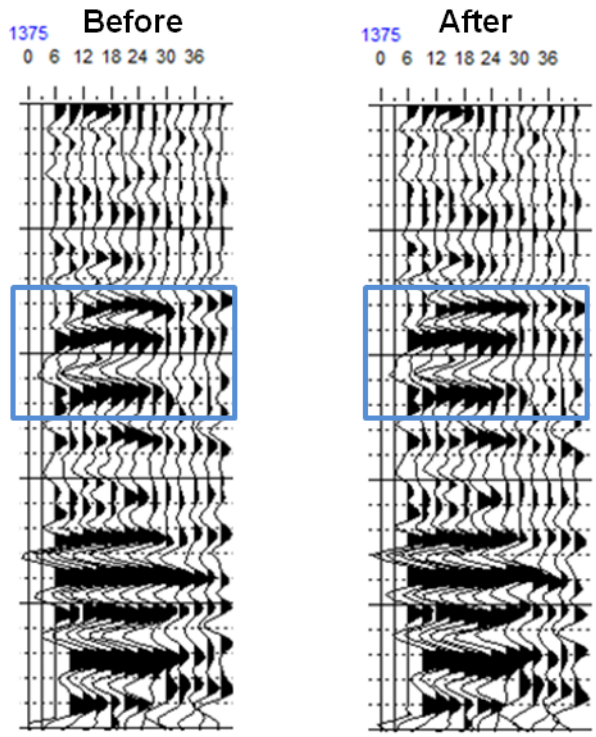

Figure B.2. CMP angle gathers (a) before and (a) after trim statics applied. Notice (a) events within the blue box (b) straightened after statics applied.

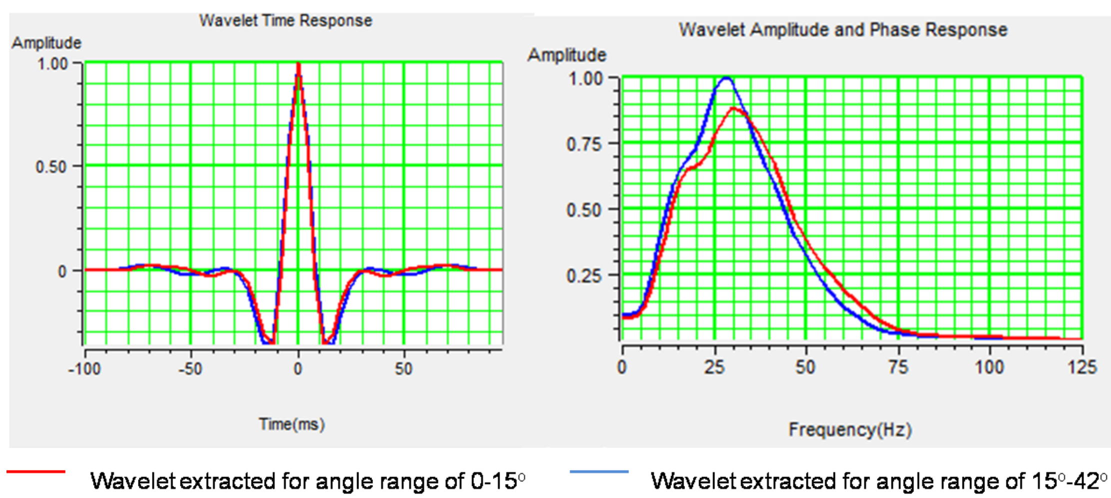

Figure B.3. Extracted wavelets from seismic data for angle ranges of 0-15^{o} and 15^{o}-42^{o}.

After tying well logs to seismic (Figure B.4), I build the initial model for pre-stack inversion, which supplies seismic with the low frequency component from the wells. Before inverting seismic volume, the inversion parameters are verified for the seismic scaling optimization. Figure B.5a shows inversion analysis of pre-stack data, where the inverted results are compared to the original log and model. Figure B.5b shows the comparison of created synthetic seismic to a real seismic data and the error (difference between the two).

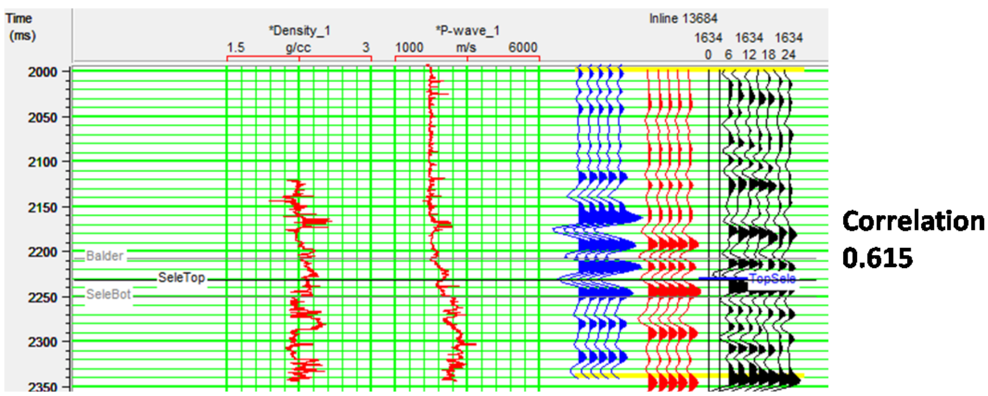

Figure B.4. Well log correlation to seismic.

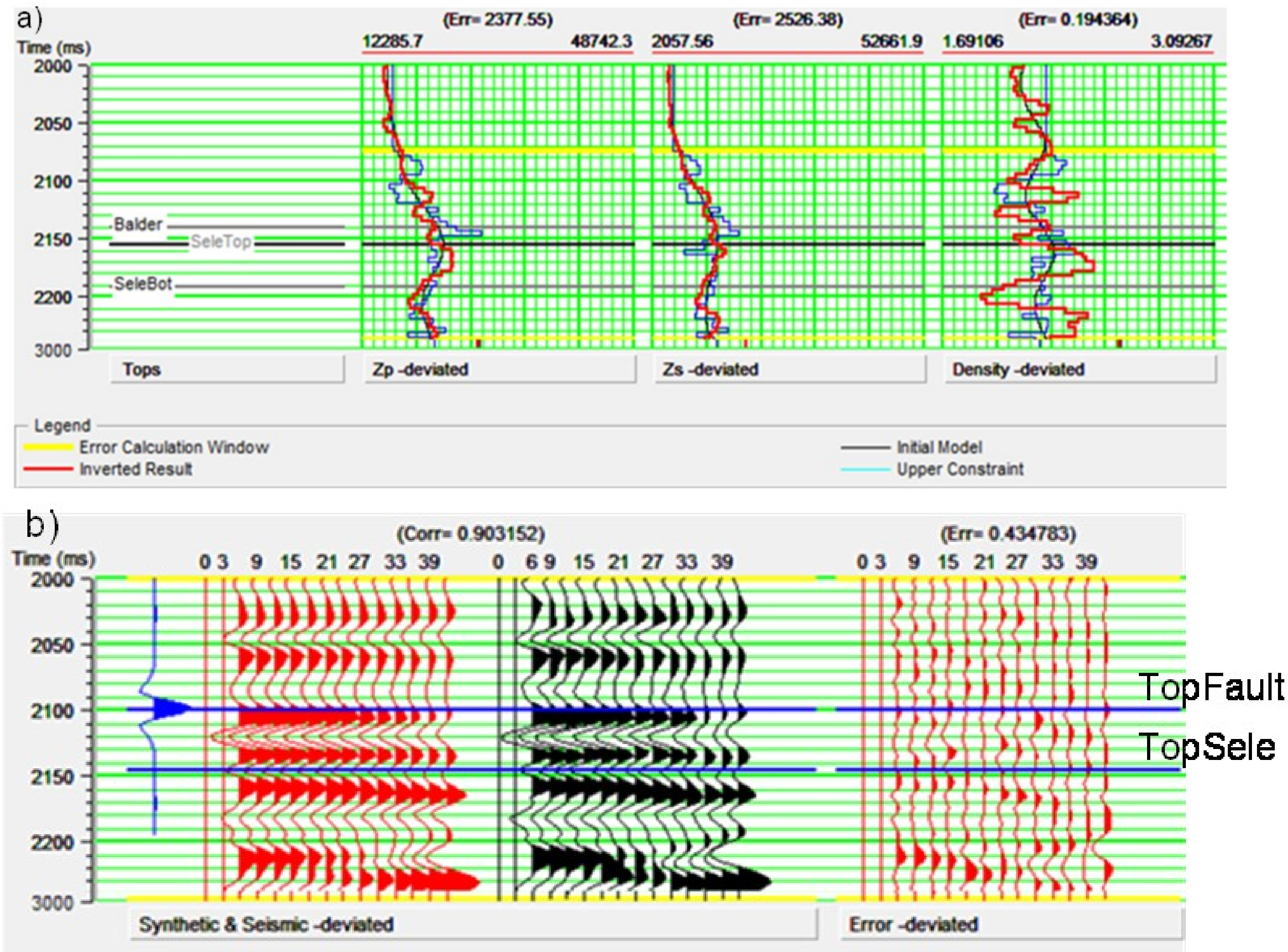

Figure B. 5. Inversion analysis of pre-stack data, where (a) the inverted results are compared to the original log and model and (b) comparison of created synthetic seismic to a real seismic data and the error (difference between the two).

APPENDIX C

Late Eocene and early Paleocene epochs include the Sele and Balder shale formations (Figure 2.1). The main reservoir pay is concentrated in the Forties Member sands of Sele Formation. The depositional environment of the Forties Member was interpreted as the middle and lower submarine fan environment due to the facies types and the vertical sequence of the formation obtained from the logs in the previous studies. Four distinct types of facies were recognized: 1) fine to medium grain size quartzarenite, 2) poorly sorted, coarse to medium/fine grain size quartzarenite, 3) gray kaolinitic shales with graded siltstone/shale sequence, which referred to as thin bedded turbidites, and 4) green waxy shale considered as the *hemipilagic* sediments (Hill and Wood, 1980). From the distribution of the facies, five informal intervals were recognized, which suggested the regional depositional environment as a submarine fan, and where the Forties Field is located in the middle and lower fan area (Hill and Wood, 1980). Later studies show that development of four interchanneled systems deposited by the high density turbidites shown in Figure 2.3 (Alpha, Bravo, Delta-Echo, and Charlie) were discovered (Ribeiro et al., 2007).

The cross-section through amplitude seismic volume shows interpreted horizons of the Balder and Sele formations and the sand reservoir of the Forties Member in Figure C.1. 3D seismic energy attributes, such as volumetric energy curvature and coherent energy detect and delineate turbidite channels of Forties Member very well. Phantom horizon, 20 ms below the Sele horizon, through the coherence volume images incise channel very well (Figure C.2c); however, in Figure C.2a and b, energy attributes detect lateral change in amplitude, thus delineating turbidites as shown in Figure 2.3.

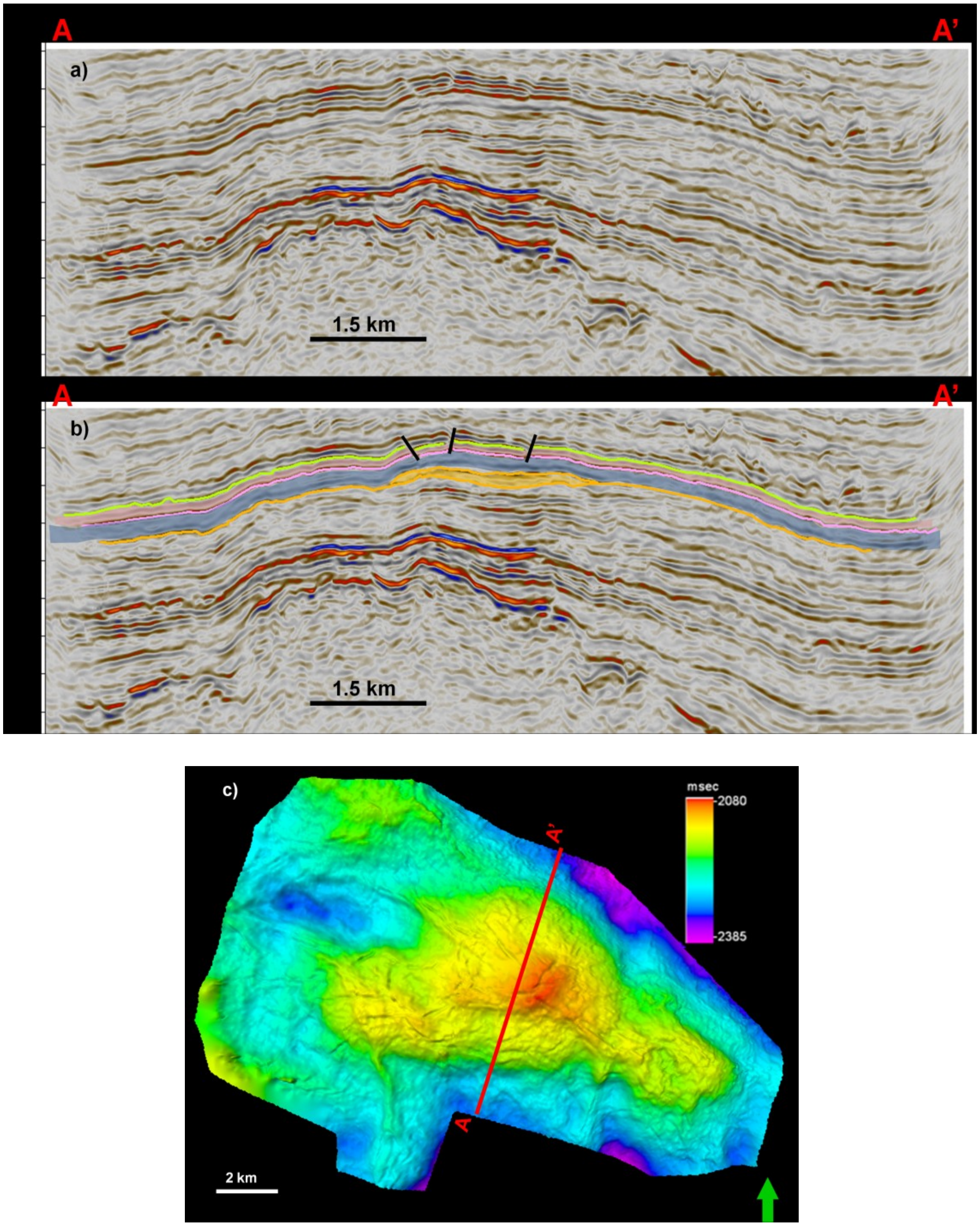

Figure C.1. (a) Vertical time slice, AA', through seismic amplitude volume (b) showing interpreted horizons of the Forties Member, the Sele formation, and the Balder formation. Location of the line is shown in (c).

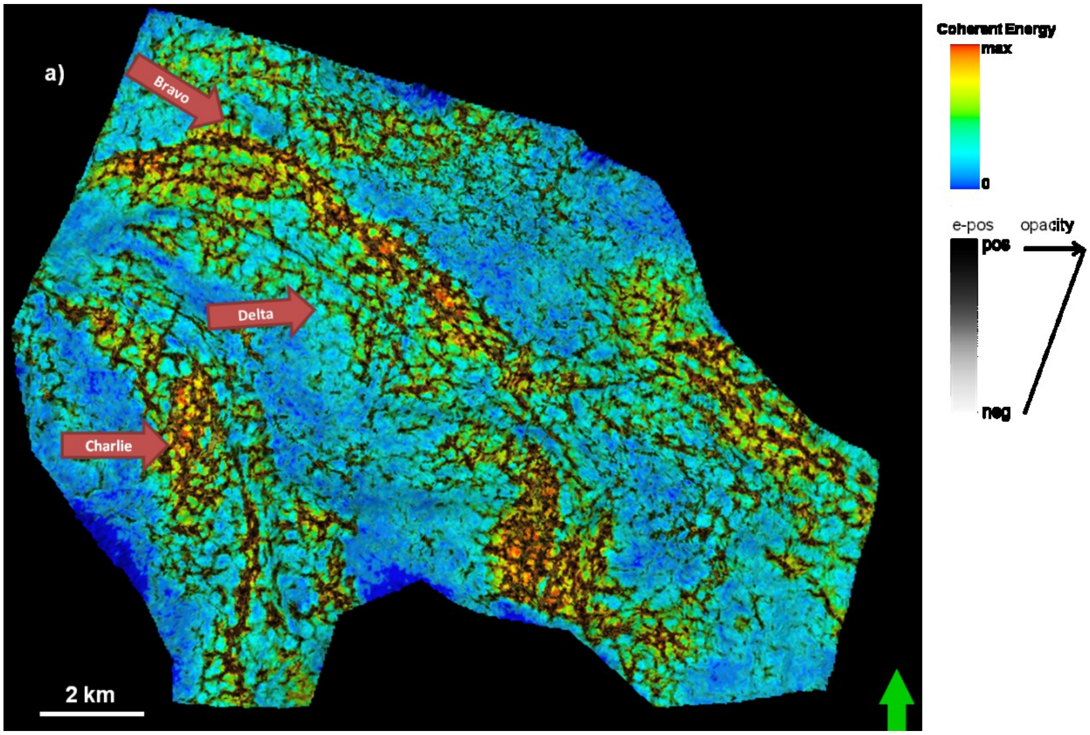
a)
Bravo
Delta
Charlie
2 km
Coherent Energy
max
0
e-pos
opacity
pos
neg

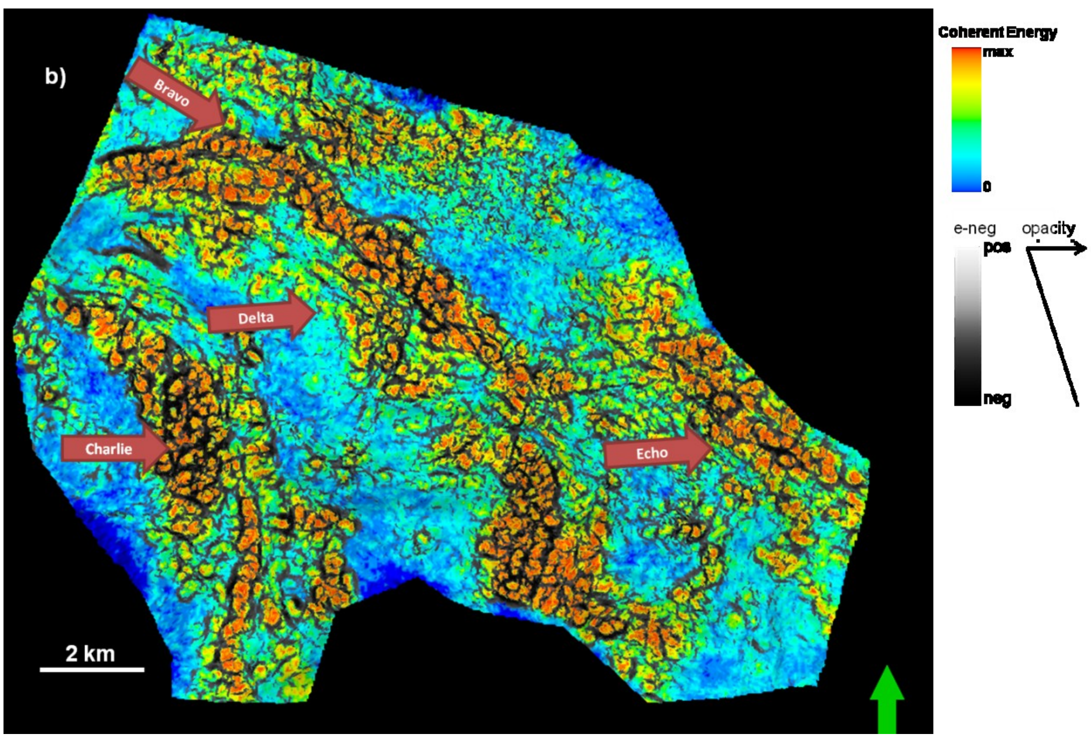
b)
Bravo
Delta
Charlie
Echo
2 km
Coherent Energy
max
0
e-neg
opacity
pos
neg

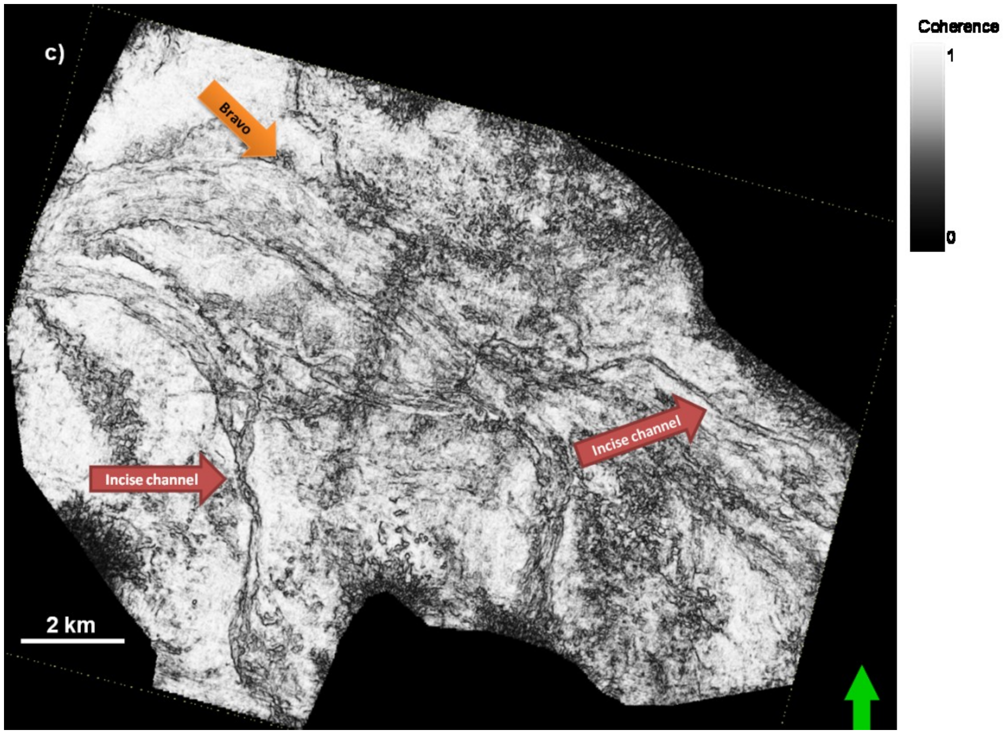

Figure C.2. Phantom horizon, 20 ms below the Sele horizon, through (a) coherent energy co-rendered with positive energy curvature, (b) coherent energy co-rendered with negative energy curvature, and (c) the coherence volume. Notice turbidity channels shown in (a) and (b), detected by lateral variation of amplitude within the Forties sands. On the other hand, (c) the coherence attribute delineates incise channel very well. The names of the turbidites correspond to Figure 2.3.

The Balder shale formation lies on top of the Sele formation and contains a series of polygonal faults, formed due to volumetric contraction during compactional dewatering of the shale. These faults are observed in the phantom horizon slice, corresponding to the Balder formation through the coherence volume shown in Figure C.3a and compared to the faults observed by Dewhurst et al. (1999) and Lonergan et al. (1998) in Figure C.3b and c.

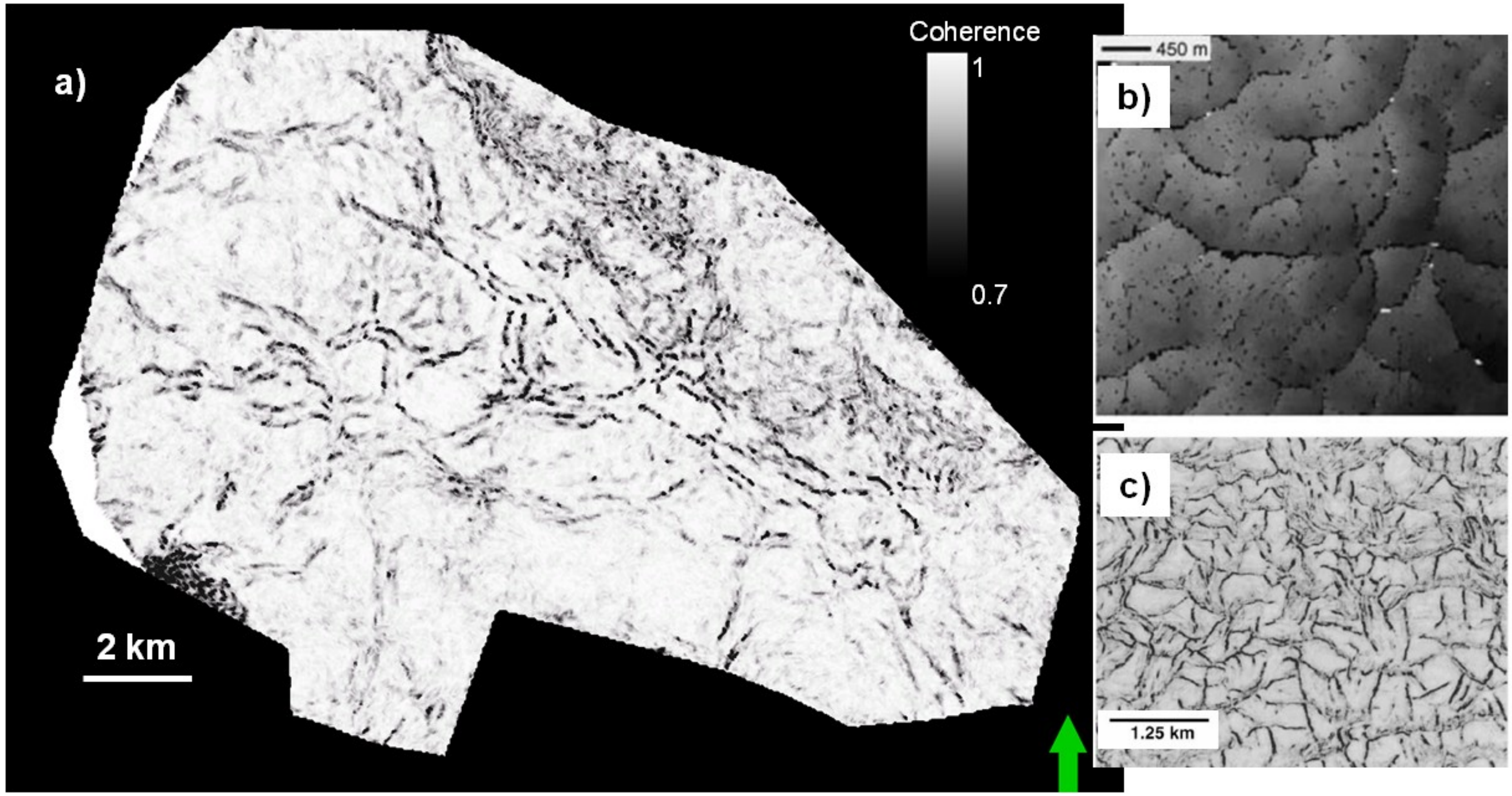

Figure C.3. (a) Phantom horizon slice, corresponding to the Balder formation, through the coherence attribute volume showing polygonal faults, similar to those (b and c) faults observed by Dewhurst et al. (1999) in the Balder formation in the Central North Sea.